CORROSION RISK ASSESSMENT SYSTEM FOR COATED STEEL PIPELINES

A Dissertation
Submitted to the Graduate Faculty
of the
North Dakota State University
of Agriculture and Applied Science

By

Fodan Deng

In Partial Fulfillment of the Requirements
for the Degree of
DOCTOR OF PHILOSOPHY

Major Department:
Civil and Environmental Engineering

November 2018

Fargo, North Dakota

North Dakota State University
Graduate School

Title

CORROSION RISK ASSESSMENT SYSTEM FOR COATED STEEL PIPELINES

By

Fodan Deng

The Supervisory Committee certifies that this ***disquisition*** complies with North Dakota State University's regulations and meets the accepted standards for the degree of

DOCTOR OF PHILOSOPHY

SUPERVISORY COMMITTEE:

Dr. Ying Huang
Chair

Dr. Fardad Azarmi

Dr. Zhibin Lin

Dr. Yechun Wang

Dr. Simone Ludwig

Approved:

November 14, 2018
Date

David R. Steward
Department Chair

ABSTRACT

Steel is widely used as building material for large-scale structures, such as oil and gas pipelines, due to its high strength-to-weight ratio. However, corrosion attack has been long recognized as one of the major reasons of steel pipeline degradation and brings great threat to safety in normal operation of structure. To mitigate the corrosion attacks, coatings are generally applied to protect steel pipelines against corrosion and improve durability of the associated structures for longer service life. Although have higher corrosion resistance, coated pipelines will still get corroded in a long run, as coatings may subject to damages such as cracks. Cracks on coatings could lower the effectiveness of protection for associated structures. Timely updates of up-to-date corrosion rate, corrosion location, and coating conditions to the pipeline risk management model and prompt repairs on these damaged coatings would significantly improve the reliability of protected structures against deterioration and failure. In this study, a corrosion risk analysis system is developed to detect and locate the corrosion induced coating cracks on coated steel using embedded fiber Bragg grating (FBG) sensors. The coatings investigated include high velocity oxygen fuel (HVOF) thermal sprayed Al-Bronze coating, wire arc sprayed Al-Zn coating, and soft coating. Theoretical models of corrosion risk assessment system were carried out followed by systematic laboratory experiments, which shows that the developed system can quantitatively detect corrosion rate, corrosion propagations, and accurately locate the cracks initialized in the coating in real time. This real-time corrosion information can be integrated into pipeline risk management model to optimize the corrosion related risk analysis for resource allocation. To place the sensing units of the system in the most needed locations along the huge pipeline systems for an effective corrosion risk assessment, an example case study is conducted in this study to show how to locate the most critical sensor placement

locations along the pipeline using worst case oil and gas discharge analysis. Further applications of the developed system can be integrated with pipeline management system for better maintenance resource allocations.

ACKNOWLEDGEMENTS

I would like to express my sincere gratitude to my advisor, Dr. Ying Huang. She was always there, willing to help and provide guidance, not only on research, but also in daily life, during my graduate study at North Dakota State University. It was such a privilege and great time working with her. I believe everyone had worked with Dr. Ying Huang had felt the same.

Thanks to Dr. Fardad Azarmi, my co-advisor. He never hesitated to provide help when I encountered problems in my research. He not only shared lots of knowledge with me, but also provided great working environment and advanced laboratory to help me achieve the completion of this dissertation.

Appreciation was also extended to members of the advisory committee, Dr. Zhibin Lin, Dr. Yechun Wang, and Dr. Simone Ludwig for their great advices and valuable time in reviewing the dissertation. Their comments and questions had made this dissertation a better one.

I also appreciated the assistant from my colleagues and friends during my graduate study, includes but not limited to Dr. Zhiming Zhang, Mr. Xiao Liang, Mr. Dawei Zhang, Mr. Leonard Chia, Mr. Xingyu Wang, and Mr. Avik Sarkar. They cheered me up when I was in a down time during my research. And I learned a lot from them and came up with a great number of new ideas in the discussion with them.

In the end, the author would like to express special thanks to my parents and Miss. Jie Long for their patience, encouragement, and support.

DEDICATION

This dissertation is dedicated to my father who taught me how to keep curious and supported me unwaveringly in twenty-seven years and eleven months.

TABLE OF CONTENTS

LIST OF TABLES

LIST OF FIGURES

Figure Page

LIST OF ABBREVIATIONS

1D ..... One Dimensional

2D ..... Two Dimensional

3LPE ..... Three-Layer-Polyurethane

CFR..... Code of Federal Regulations

DOF ..... Degree of Freedom.

EIS ..... Electrochemical Impedance Spectroscopy

FBE ..... Fusion-Bonded Epoxy

FBG..... Fiber Bragg Grating.

FEM ..... Finite Element Model.

GDP ..... Gross Domestic Product

HVOF..... High Velocity Oxygen Fuel.

NPS ..... Nominal Pipe Size

PHMSA..... Pipeline Hazardous Material Safety Administration

1. INTRODUCTION

As the most vital media of transporting oil and gas in the industry, pipeline systems were located in every state in the US. For those pipelines across villages or rivers, oil and gas spill could be a huge disaster for local community and environment [1-8]. In a statistic result from Pipeline Hazardous Material Safety Administration (PHMSA) shown in Figure 1, it could be seen that several serious pipeline incidents could results in a cost up to hundreds of millions of dollars.

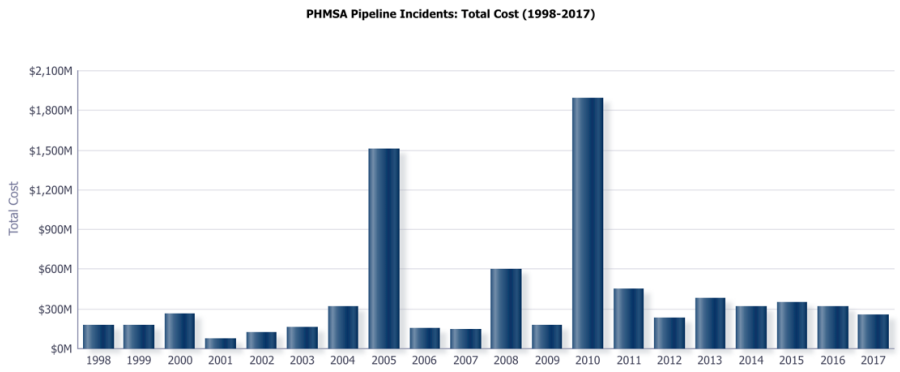

Figure 1. Total cost of pipeline significant incident in US dollars from 1998 to 2017.

Other than the direct financial burden for both pipeline operators and related parties, the environment impact brought by the pipeline incident could be huge, too. In 2013, an oil spill of about 840,000 gallons (also known as Tesoro spill) was occurred on 6-inch diameter pipeline in North Dakota state, near the city of Tioga. It took about five years for liable parties to clean up the spill. More than 1.4 million tons of dirt was excavated and the total cost for this disaster was estimated to be 93 million dollars. Large amount of farm land was damaged, and the health of local people was put in threat in this spill. In 2016, a gasoline leakage of about 350,000 gallons occurred on Colonial Pipeline in Alabama State. Six states near the leakage location declared states of emergency and people were evacuated. This accident also caused gas shortage in

southeast United States. All these spill or leakage accident had emphasized the need of safety in pipeline operation.

As known, steel is very popularly used as building material for pipelines, especially transmission pipelines, since it has high strength-to-weight ratio. However, for steel, a well-known problem is corrosion, which is one of the major threats to safety of steel pipelines [1, 4, 9]. According to the pipeline incidents statistics collected from PHMSA in recent 20 years, nearly 18.2% of the incident was reported as caused by corrosion. Besides, the deterioration brought by corrosion may also cause pipeline more vulnerable to other types of pipeline failures such as buckling and cracks. So, to ensure the pipeline system operation safety, a comprehensive corrosion mitigation plan should be derived.

Application of coatings on steel is recognized as an effective approach to mitigate corrosion on pipelines, however, coated pipelines would still corrode in a long run and the corrosion damages on coatings are hard to detect and analyze. Corrosion stress cracks on coatings, specifically, could introduce accelerations on coated steel pipelines which may concern the pipeline safety, resulting in a need for a corrosion risk assessment system. Thus, this chapter will have a detail introduction on the background, motivation, and literature review on the needs of the development of proposed corrosion risk assessment system.

1.1. Background

When transporting massive amount of fluid, liquid, or gas, pipeline has great amount of advantages over other types of transportation methods in aspects of efficiency, cost, operation risk, environment, etc.[10]. In 2015, nearly 71% of energy transportation in United States was done by pipeline, and a total of more than 2.5 million miles of petroleum and natural gas pipeline were in operation[11]. With phenomenally increased demand for natural gas in recent years,

more natural gas pipeline will be constructed in the near future. As one of the most popular structure materials, steel is widely used in large-scale infrastructures including pipeline. Compared with other type of traditional building materials, steel is more reliable against several severe situations, such as earthquake, tornado, or explosions, considering its higher strength-to-weight ratio and ductility [12-15]. With recent development of production techniques in steel industry, the cost of steel components was reduced, and the environmental-friendliness was greatly improved, bringing a steady growth in attention in steel as a cost-effective building material choice for pipelines[16, 17].

However, steel components are vulnerable to corrosion attack [4, 5, 18-21]. Corrosion happens naturally when structure steel meets with water and oxygen concurrently. The corrosion reaction consists of a sequence of sub-reactions, ended in consuming steel as well as producing rust. Corrosion had been long recognized as one of the main reasons of structural steel component degradation due to its ability to substantially lower the cross-section area of component, causing a substantial deterioration in load-carrying capability of associated structure [4, 5]. Corrosion happens in reinforced concrete pipeline components also had been categorized as one of the most critical type of degradation [22, 23]. Not only because the corrosion reduces load capacity of steel bars in concrete, but also rust has much less density so that the enormously increased volume leads to severe cracks in concrete, resulted in unexpected component failure. Therefore, corrosion significantly impacts the reliability and safety of pipeline and might cause catastrophic impacts on both human and environment occasionally if not properly mitigated. According to a report in 2002 [24], the corrosion related failure and corrosion management direct cost was 7 billion USD in gas and liquid pipeline. Considering the rapidly increased oil and gas industry in recent 10 years, the corrosion related cost could become relatively large. Based on

this report, the newest estimation for corrosion cost in 2016 had been updated to be 1.1 trillion USD, which accounts for about 6% of the gross domestic product (GDP) of United States.

1.2. Literature Review

To mitigate the corrosion on steel pipelines, coatings are widely applied [1, 4, 5]. Coatings including soft and hard coatings serve as barriers between the steel and outer corrosive environmental, which had shown magnificent performance in corrosion mitigation. However, as every structure, coatings could fail under certain conditions such as external impacts, abrasions, biology attacks, water scouring, etc. When the coatings failed, the underlying structure would be exposed to corrosive environmental and subjected to corrosion attacks. To ensure the proper functionality of coatings, multiple types of non-destructive testing techniques can also be applied to verify the performance of coatings as well as to predict service life [25-35].

1.2.1. Soft Coatings

The corrosion of a metal is an electrochemical process. Although there are various factors controlling the process of corrosion, including the physical and chemical properties of metal, the roughness of metal surface, temperature, etc.; it is clear that presence of both water and oxygen is necessary for electrochemical reaction of corrosion to happen. With the presence of free electrons, water and oxygen, reduction happens at cathodes, as shown in the reaction below [5, 25]:

$$2H_2O + O_2 + 4e^- = 4OH^- \quad (1)$$

When coatings isolate the metal substrate from both water and oxygen, the electrochemical process shown above would not be able to start at substrate. Based on the surface hardness of coatings, coatings could be categorized as soft coating or hard coating.

Coatings with low surface hardness were categorized as soft coatings. Soft coatings predominantly are composed of carbon compounds, which mostly are chemical inert to corrosive environment to metals. The earliest available soft coating is coal-tar coatings [36]. Coal tar was discovered in 1665 and not widely used as a type of corrosion mitigation methods in structures until 1910s, when the difficulties in odor and liquidity had been addressed by numerous efforts put on mixing coal tar with various additives [37-39]. Coal tar coatings were very consistent and had the possibility to permanently protect substrate against corrosion if properly maintained. However, coal tar coatings could cause serious environmental damage and general public health problems, and the coating process might also bring health problem to coating workers [40, 41]. In addition, pipelines with coal tar coatings were in general not properly maintained in a long run, resulting in an overall service life of only five to ten years [42].

For a safer soft coating, polyurethane coating was developed and became an acceptable alternative to coal tar based coatings around 1980s [43-46]. Later in 1990s, since field experience demonstrated that service life of polyurethane coatings generally couldn't satisfy the expectations of long-term uses, coatings of thicker layers had been developed to fulfill durability demands. Polychloroprene coating, Fusion-Bonded Epoxy (FBE) coating and Three-Layer-Polyurethane (3LPE) coating are several widely-used thick layer soft coatings [47-50]. But thick layer soft coatings had some trade-offs such as high cost and more complicated coating process, and thin layer soft coating would be more easily to delaminate from substrate inducing more risk [51-53]; resulting in an increasing need to find the balance between coating thickness and durability.

1.2.2. Hard Coatings

To improve the roughness of the applied coatings, hard coatings are also investigated to protect pipelines from corrosion. Hard coatings generally compose of metal particles with higher corrosion resistance and higher density than substrate [54-58]. Thus, metallic hard coatings provide wear resistance in addition to the corrosion resistance. Since metallic hard coatings introduce various types of metals, their application brings potential galvanic corrosion problem. Galvanic corrosion describes the situation where one metal corrodes preferentially over the other one when they contact with each other electrically with presence of an electrolyte [4, 5]. In such situation, the corroded metal is less corrosion resistant (or more chemically reactive), and the reserved metal is more corrosion resistant (or less chemically reactive). In hard coating, if the metal particles in coating is less corrosion resistant than substrate, the corrosion would first happen on coating itself, which means the coating sacrifices itself to preserve the substrate; on the other hand, if the metal particles in coating is more corrosion resistant than substrate, the corrosion would first happen on the substrate, which means it requires additional corrosion mitigation strategies against galvanic corrosion to be considered to preserve the substrate. Under either circumstance, the application of hard coating would inevitably have trade-offs such as higher initial cost or maintenance cost.

Many coating processes are available in applying hard coating [59], such as mechanical bonding/cladding, physical/chemical vapor deposition, thermal spraying, hot dipping, etc. Spraying technologies are widely used to provide pipeline wear resistance as well as corrosion resistance due to its ability not only to apply new coatings on large area of desired substrate, but also to repair failed coatings on-site without disturbing existing structure. Based on the different type of spraying energy sources, the spraying technologies could be further categorized by

chemical energy spraying (such as flame spraying, high velocity oxygen fuel spraying, etc.) and electrical energy spraying (wire arc spraying, etc.).

In flame spraying, coating material is fed into the gas produced flame; and then blown onto the desired surface of substrate by a highly-compressed air wave. Flame spraying technology is one of the earliest spraying techniques in 1910s [60]. It is still widely used nowadays mainly because its low cost and convenience.

The high velocity oxygen fuel (HVOF) spraying technology uses a spraying gun mixing oxygen and fuel in a combustion condition and generate a gas wave with a speed of more than 700 m/s and a temperature of higher than 3000 °C [61-63]. Due to the high velocity and temperature, the HVOF spraying technology was capable of producing thick layers of coating while maintaining low porosity, which contributes to its high corrosion and wear resistance.

The wire arc spraying technology uses two wires of desired coating material serving as two electrodes and then moved through a spraying gun [64, 65]. Powered by an electric current, coating materials moved in spraying gun are melted and then sprayed onto the surface of substrate. During the spraying process, melted coating material will have a temperature of more than 5000 °C, which create great bonding strength. Additionally, the melted coating material only has a velocity of around 150 m/s when spraying onto substrate, so the energy consumption of wire arc spraying technology is relatively low.

Research successes in non-metallic hard coatings such as ceramic coatings had unveil the potential to overcome the disadvantages of metallic hard coatings while preserving the desired high wear resistance [66-71]. However, application of ceramic coatings in large-scale infrastructure is limited due to the high cost of coating process. Therefore, soft coatings are often

chosen to be applied together with hard coatings to mitigate the possible galvanic corrosion attacks when wear resistance is in consideration.

1.2.3. Corrosion Risk Assessment Tools

To analyze the corrosion risk of a steel pipeline, the first priority is to assess the corrosion condition of the pipelines. Corrosion brings several direct changes that could be used for either destructive or non-destructive techniques such as electric potential and alternation of surface properties. The former one is the fundamental of weight loss measurement and electrochemical corrosion research [29, 30], and the latter is the origin of ultrasonic [26, 27, 33], acoustic emission [72, 73], and other wave-based non-destructive corrosion detection methods [74].

For destructive corrosion assessment, there are mainly two approaches including weight loss measurement and electrochemical measurement [29]. Weight loss measurement, which is also known as exposure test, is simple in concept which measures the weight difference of a coupon (sample) between a certain time interval while placing it in a controlled corrosive environment. The corrosion rate is the weight difference divided by the time elapsed because the weight loss on coupon is exactly the amount of metal consumed by the corrosion reaction. Weight loss measurement is the earliest attempt to perform quantitative corrosion assessment [75, 76], and is also the direct approach to accurately measure the corrosion rate in a certain environment. With statistical study and visual inspection efforts, weight loss measurement could provide additional information such as common early signs for corrosion initialization and corrosion types to guide local corrosion mitigation strategies [77]. However, weight loss measurement is extremely time-consuming and generally takes 30 days to decades to complete depends on the coupons and environment setups. In the excessively long-term weight loss

measurement, there also could be problem that at the time measurement was done, the environment to be simulated had already changed while performing the measurement.

Electrochemical measurement, or electrochemical impedance spectroscopy (EIS), was first used in corrosion assessment in 1950s, and fast gained popularity due to its capability of completing measurements in a short period of time while providing and repeatable and reliable results [29, 30, 78]. Since the corrosion reaction is one type of electrochemical reaction composing of anode, cathode, and electrolyte, the corrosion rate could be determined by an equilibrium between electrochemical reactions at anode side and cathode side. A general electrochemical measurement test setup is shown in Figure 2, and the corresponding measurement result is shown in Figure 3 (two test samples). A test instrument electrically connected to sample is used for both inducing potential and measuring current on anode and cathode sides. One test cycle on one sample only costs 30 minutes or less if only short-term corrosion rate is desired. In addition, electrochemical measurements also could be adjusted for long-term corrosion behavior analysis purposes [79, 80].

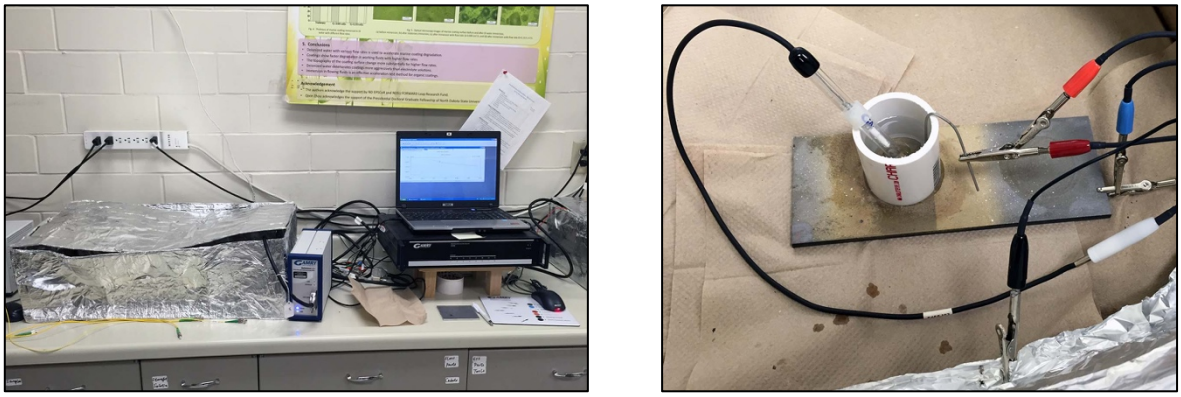

(a) (b)

Figure 2. A typical electrochemical measurement testing setup.

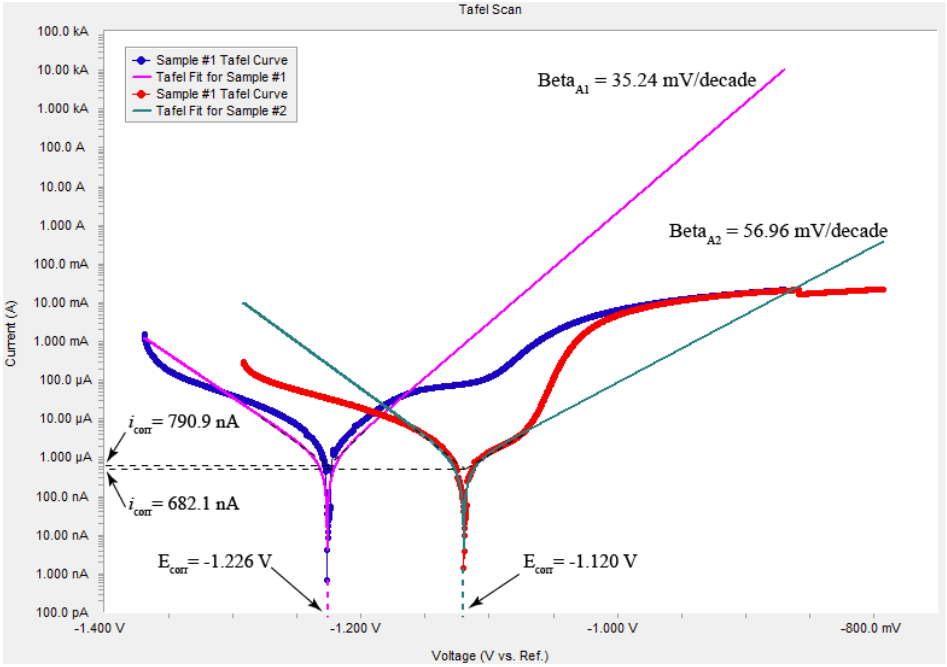

Figure 3. A typical electrochemical measurement result.

As seen above, both weight loss and electrochemical measurement are destructive corrosion assessment. Though they are able to obtain corrosion rate directly, they are not suitable for conducting corrosion assessment on an existing pipeline and could only be used to determine the corrosion resistance of a type of metal or coating before it is placed in actual operation of a pipeline, or the corrosiveness of the environment where pipeline is operating. In such circumstances, several non-destructive corrosion assessment methods are used to evaluate corrosion severity including ultrasonic and acoustic tools and embedded or attached sensors.

Ultrasonic measurement methods are one of the most popular corrosion assessment methods used in the pipeline industry. It provides of high sensitivity, accurate, and immediate assessment for pipeline thickness [26, 27, 33]. Similar to all other waves, ultrasound echoes when transmit from one medium to another. Thus, if there is no change in the pipeline thickness, the intervals of ultrasonic echoes would be a static value. When corrosion occurs, the metal is consumed, and pipeline thickness is reduced, which could be detected by the ultrasonic wave as

the intervals of echoes would change corresponding to the change of thickness. A set of ultrasonic measuring instruments often includes a transducer to emit ultrasonic wave, a receiver to receive the ultrasonic wave emitted from transducer, and controller to coordinate two parts and visualize the data. The transducer and receiver could also be combined in the same working unit in case of that receiver is used for receiving reflected ultrasonic wave. Traditional ultrasonic measurement methods are point-by-point measurement in natural, as it requires ultrasonic wave perpendicularly penetrate the pipeline wall, but researches had shown potential of enlarging measurement range when combined with guided wave methods [81, 82]. However, the ultrasonic measurement methods are having difficulties perform assessment on irregular shape parts, and the extensive knowledge requirement for operating and understanding the instrument often limits its application. Furthermore, the ultrasonic measurement requiring human operation on-site could hardly become a candidate for real-time monitoring system of large area.

Acoustic emission (AE) has been widely used for damage monitoring in loaded structures, and researches is trying to adapt it in corrosion assessment and monitoring of pipeline [72, 73]. When there is rapid release of energy within structure, such as the occurrence of a crack, a set of transient elastic waves are generated and transmitted started from that release location. This phenomenon is acoustic emission. By analyzing the properties of AEs transmitted to receiver, the damage could be categorized and localized. AE method as one type of passive detection method is suitable for real-time monitoring and provides high sensitivity, however, it would have low signal-to-noise ratio in field for small cracks.

Strain sensor-based corrosion assessment methods are gaining attention recently. When corrosion reactions happen, though original metal is consumed, the corrosion products (oxidized metal) would occupy several times of volume compared with original metal. If the corrosion

reaction happens in a confined space, the excessive increased volume would induce a noticeable amount of strain, which could be used as an indicator of corrosion reaction. However, electrical strain gauges may have difficulties applying in pipeline corrosion assessment due to the underground nature for most of the pipelines with moisture and intensive electromagnetic noise.

Fiber optic sensors which are made by silica materials have a great potential as a sensing tool in strain based corrosion assessment of steel pipelines. Among all fiber optic sensors, fiber Bragg grating (FBG) sensors are well-known for its reliability and high sensitivity. Fiber Bragg grating (FBG) sensors in recent 15 years had received lots of attention due to their simplicity in installation, high sensitivity and exceptional durability [83, 84].

Other than being an alternative to strain and temperature sensors, FBG sensors were proven to have the capability to detect and locate cracks on concrete and metallic structures, if properly cooperated with other non-destructive detection methods such as acoustic emission and ultrasonic [34, 85, 86]. FBG sensors also had the advantages of chemical inertness because FBG sensors do not require any metallic components, which made them outstanding choices in corrosion monitoring system. A few recent attempts to apply FBG sensors in corrosion monitoring of steel rebar in reinforced concrete and the previous attempt to apply FBG sensors in hard coating in preliminary study had shown the possibility of FBG sensors in corrosion monitoring [87-90]. Relatively low cost of FBG sensors also made large-scale application practical and thus made FBG sensors strong candidate in corrosion monitoring system [84, 91-100]. However, to date, limited sensing technologies can monitor the corrosion due to the harsh environment occurs on structural steels with coatings.

The advantages and disadvantages of existing corrosion measurement methods were briefly summarized in Table 1.

Table 1. Summary of existing corrosion measurement methods.

Measurement Methods	Weight Loss Measurement	Electrochemical Measurement	Existing Non-destructive Measurement
Advantages	Accurate.	Fast and repeatable; Available for corrosion mechanism research.	Include results more than corrosion related information.
Disadvantages	Time-consuming; Impractical for large scale.	Destructive; Interference Sensitive.	Human interference required; Relatively high cost.

1.3. Problem Statements

From the literature review above, the following findings and gaps can be identified:

1) Coatings including both soft and hard coatings can be effective corrosion mitigation ways for steel pipelines, however, the corrosion induced coating damages are hard to detect and may bring concerns to the pipeline safety.
2) Traditional corrosion risk assessment and detection tools for coated structures require large amount of human interference and may not be suitable and comprehensive in all structures, such as large-scale structures like pipeline and marine structures. In addition, the long maintenance interval in coating makes structures vulnerable to corrosion attack.
3) An on-site real-time continuous corrosion risk assessment system with ability to detect corrosion status and coating crack failure will significantly increase reliability of the coatings and the monitored structure in addition to increasing resource allocation efficiency in corrosion mitigation.

4) Since the pipeline is very long and in a large scale, the placement of sensing units of the corrosion risk assessment is very challenging and to date there is no clear guideline for the placement of the sensors.

1.4. Research Objectives

In this dissertation, to address the challenges mentioned above, the objective is to develop a reliable on-line real-time corrosion risk analysis system for coated steel pipelines through embedded fiber optic sensors. The proposed study will provide a new concept in corrosion risk analysis of steel pipelines, which is expected to greatly increase the reliability of pipelines in harsh environments, reduce the maintenance cost, and extend coverage of existing risk management system when integrated.

Specifically, this study has five detailed objectives:

1) Select sensor feasible of performing continuous long-term data acquisition in highly corrosive environment;
2) Develop an on-site real-time continuous corrosion risk assessment system with ability to detect corrosion status and coating crack failure;
3) Evaluate the performance of the corrosion risk assessment system in different combination of base metals and coating types;
4) Develop an algorithm for corrosion location and evaluate the sensitivity of corrosion risk assessment system;
5) Explore the optimized sensing unit placement locations along the pipeline using the worst case oil and gas discharge calculations.

Thus, the remaining dissertation is organized according as follows: in Chapter 2, the corrosion risk analysis system design is developed for coated pipelines; in Chapter 3,

systematical laboratory experiments are carried out for various coated structures to validate the developed corrosion assessment system and the experimental results are presented; in Chapter 4, the algorithms to identify corrosion locations are studied and system sensitivity parametric study are performed; in Chapter 5, an example case study is presented to determine the sensing unit placement locations along the pipeline using real-world worst case oil leakage discharge analysis; In Chapter 6, it is given the conclusions and future work, which have been demonstrated based upon the findings from this study.

2. CORROSION ASSESSMENT SYSTEM DESIGN FOR COATED PIPELINES

The design of a practical corrosion risk analysis system for coated pipelines, an effective corrosion assessment needs to be in place. Based on the fundamental corrosion principle, to assess corrosion, some physical properties of a corroded pipeline such as corrosion induced strains in coated pipes can be measured and monitored using embedded sensors. In this chapter, the fiber Bragg grating (FBG) sensor is introduced and designed to embedded inside the coatings of a pipeline to assess its corrosion status, and the detail theoretic corrosion detection principle by using FBG sensors for coated structures is discussed. Based on the real-time corrosion assessment of the coated pipelines from the embedded FBG sensors, a corrosion risk analysis system is designed to provide further decision-making analysis such as worst case oil and gas leakage analysis and maintenance resources allocation.

2.1. Corrosion Principle

Corrosion as an electrochemical degradation process of a metal composes of a series of reactions involving free electrons transfer from anode side to cathode side [5]. Metal is oxidized in the corrosion reaction acting in anode side and provides free electrons and oxygen and water are reduced acting in cathode side and receives free electrons. The corrosion process could be shown as Equation (1) as shown in Chapter 1 and repeated below [5, 25].

$$2H_2O + O_2 + 4e^- = 4OH^- \quad (2)$$

Reduction reaction at cathodes introduces several material property changes of the cathodes. For instance, when corroded, the iron gets oxidized and then dehydrated to ferrous oxide, ferric oxide and ferro-ferric oxide, which in average have ten times occupied volume comparing to the original iron metal, would gradually replace the original metal and expand in volume. Thus, detecting the material volume or expansion change using sensing techniques

throughout the corrosion process can potentially reveal the corrosion status such as corrosion rate and weight loss of the electrochemical process of metals.

2.2. Operational Principle of Fiber Bragg Grating Sensor

In this study, FBG sensors are used to detect and assess the corrosion status and any corrosion related damages such as crack initialization of coated pipelines. Figure 4 shows a typical structure of an FBG sensor. It is fabricated by periodic heating of fiber core using high-power UV laser, inducing a periodic modulation of the core refractive index. With the modulation, if a broadband light beam is transmitted through the FBG, part of the incoming light with certain wavelength will be reflected showing a dip in the reflected light spectrum, known as Bragg wavelength.

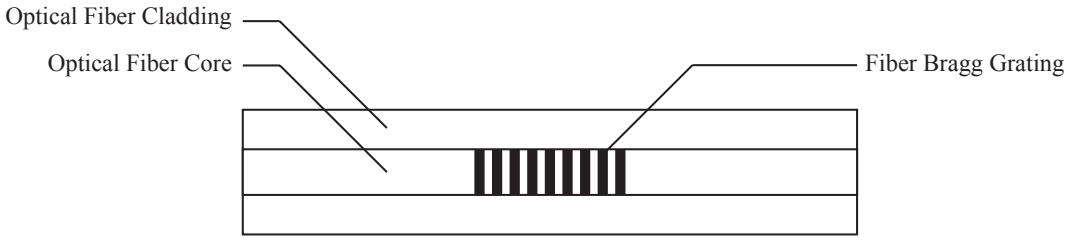

Figure 4. The Structure of a Typical FBG Sensor.

The Bragg wavelength (λ_B) needs to meet the Bragg condition with effective refractive index (n_{eff}) and grating pitch (Λ), as below [35]:

$$\lambda_B = 2n_{eff} \cdot \Lambda \tag{3}$$

The effective refractive index (n_{eff}) is determined by the transmitting media, which is optical fiber core in the case of an FBG sensor. It does not change during its use in corrosion detection or assessment as there is no material change related to optical fiber core. However, the grating pitch (Λ) does change with length variation of FBG, whether it is caused by a temperature raise/drop (ΔT) or an external tension/compression (ε_c). Changes in grating pitch

result in shifts in Bragg wavelength. From the wavelength spectrum of reflected light, a shift in peak wavelength can be found as shown in Figure 5.

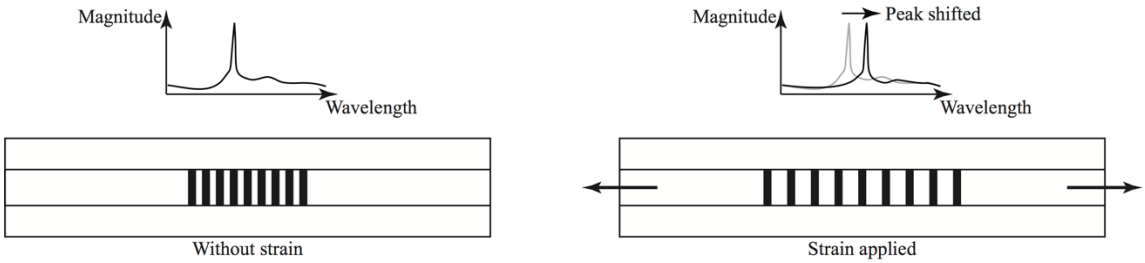

Figure 5. Bragg wavelength shift of reflected light when strain is applied on FBG sensor.

The amount of Bragg wavelength change ($\Delta\lambda_B$) with the changes in strains and temperatures can be calculated as below [101]:

$$\frac{\Delta\lambda_B}{\lambda_B} = (1 - \mathrm{P}_e) \cdot \varepsilon_c + [(1 - \mathrm{P}_e) \cdot \alpha + \xi] \cdot \Delta T \tag{4}$$

where P_e is the photoelastic constant of the fiber and α is the thermal expansion coefficient of the fiber, both determined by the material of fiber.

Thus, with an additional temperature reference sensor applied, the temperature effects, which refers to the second term in Equation (4) associated with ΔT, could be compensated. If the Bragg wavelength of temperature reference sensor is λ_{ref}, then the wavelength change induced by temperature can be described as:

$$\frac{\Delta\lambda_{\mathrm{ref}}}{\lambda_{\mathrm{ref}}} = [(1 - \mathrm{P}_e) \cdot \alpha + \xi] \cdot \Delta T \tag{5}$$

Combining Equation (4) into Equation (3), the wavelength change induced by external strain could be described as follow:

$$\frac{\Delta\lambda_B}{\lambda_B} = (1 - \mathrm{P}_e) \cdot \varepsilon_c + \frac{\Delta\lambda_{\mathrm{ref}}}{\lambda_{\mathrm{ref}}} \tag{6}$$

If a reference sensor is selected to satisfy condition that $\lambda_{\mathrm{ref}} \approx \lambda_{\mathrm{B}}$, then wavelength change with strain effects only after compensating the temperature effects ($\Delta\lambda = \Delta\lambda_{\mathrm{B}} - \Delta\lambda_{\mathrm{ref}}$) can be expressed as:

$$\Delta\lambda = \Delta\lambda_B - \Delta\lambda_{\mathrm{ref}} = (1 - \mathrm{P}_e) \cdot \lambda_B \cdot \varepsilon_c \quad (7)$$

Hence, with the measurement of Bragg wavelength change of a test sensor and a reference sensor, the strains on an FBG sensor can be calculated directly with the linear relationship between them ($\Delta\lambda \propto \varepsilon_c$), which can be further related to corrosion status and crack propagation of a coated pipeline.

2.3. FBG Sensor Embedment in Coatings

From Section 2.2, it can be seen that the FBG sensors can detect strain generation and progressing if attached to a structure surface. However, for a coated pipe, the corrosion will not occur on the surface of the coating, but in most cases, it will occur beneath the coating. Thus, to effectively detect and assess the corrosion on a coated pipeline, the FBG sensors need to be embedded inside the coatings of a pipeline. For a soft coating, the FBG sensors are easy to be embedded inside the coating through attaching the sensors on the pipeline surface and applying soft coatings after.

However, for some hard coatings such as thermal sprayed coatings, the embedment of FBG sensors inside the coating is very challenging. As is reviewed in Chapter 1, there were varies of thermal spraying coating techniques used for applying coating on metal surface, such as wire arc spraying, high velocity oxygen fuel (HVOF) thermal spraying, and plasma spraying. Most of them involve melting metal particles, accelerating the melted metal particles to high speed, and then hitting on the desired surface to form a condensed hard metallic coating surface Since the FBG sensors is made by silica materials and has a very small size of 125 μm in

diameter, it is very vulnerable to get damaged during the coating process of applying thermal sprayed coatings when high temperature and high impact are associated.

To survive during the harsh environments of a thermal spraying coating process, packaging method is required to protect the bare FBG sensor from damage. In this study, steel hypodermic tubes were used to package the FBG sensors as seen in Figures 5(a) to 5(d). The Bragg grating part of the FBG sensor was first protect by a stainless-steel hypodermic tube with a diameter of 0.01225 inch, shown in Figure 6(a, b). This ultra-fine tube could provide enough stiffness to prevent the core part of Bragg grating from bending failure when there was high impact from thermal spraying. It also helps the sensor to maintain its integrity when corrosion induced too much strain at one side, which may cause the sensor data inquisitor fail to read the data. The fiber other than Bragg grating part was then protected by a stainless-steel hypodermic tube with a larger diameter of 0.028 inch. This hypodermic tube was also used to provide extra stiffness to the optic fiber to prevent it from bending failure. To make sure there is no fiber got exposed to high temperature/high impact environment, these two types of hypodermic tubes have an overlap of about 0.25 inch, shown in Figure 6(c, d). Overlap section of two types of tubes is ensured by applying M-Bond 200 epoxy to prevent sliding.

The packaged FBG sensors were then attached to the surface of steel substrate using high temperature durable adhesives before coating as shown in Figure 6(e). The adhesive used is stainless-steel based adhesive. Comparing with other types of adhesive, this type of adhesive provided higher temperature resistance, higher wear resistance, and higher abrasion resistance. After FBG sensor got protected by the packaging and the adhesive, thermal spraying coating process then could be applied on top of the sensor and desired metal surface. Since the HVOF thermal spraying introduced the harshest environment for FBG sensor embedment, it was

selected to test the protection effectiveness of the FBG sensor packaging. Figure 6(f) showed the HVOF thermal spraying coating process for steel samples with embedded FBG sensors.

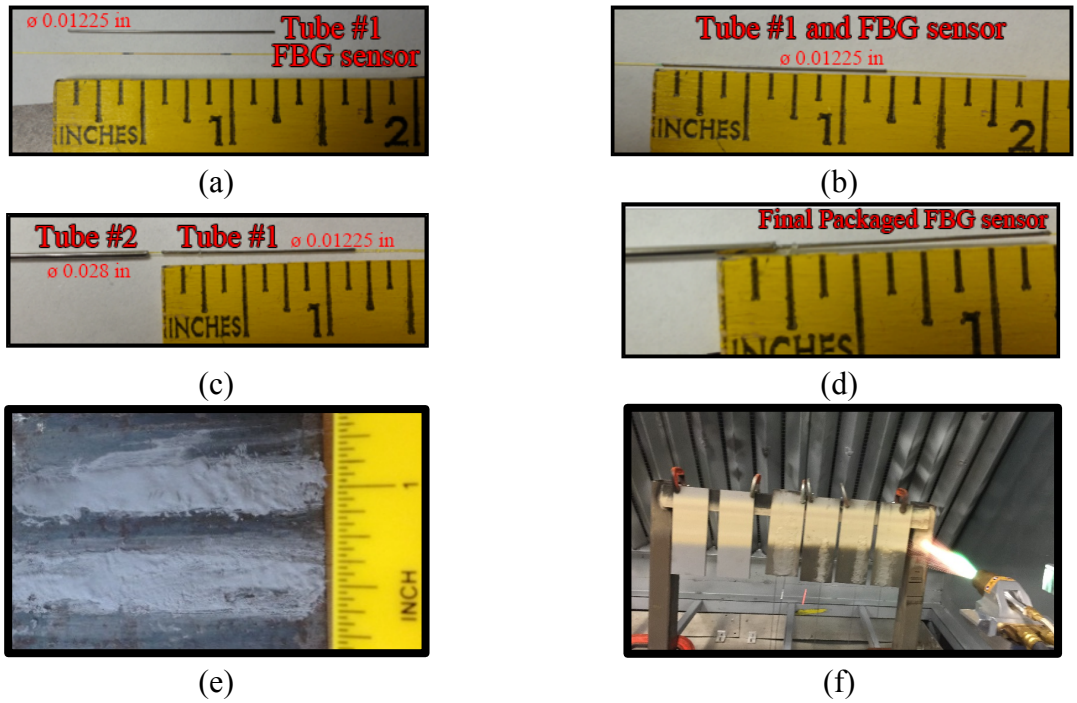

Figure 6. FBG sensor packaging process and testing HVOF thermal spraying.

To validate that the FBG sensor successfully survived during the coating, Figure 7 shows the monitored center wavelength changes from the one of the embedded FBG sensor from the coated samples in Figure 5(f). The figure shows clearly that the FBG sensors detected the temperature changes during each round of spraying process. After six rounds of spraying, the coating process was finished, and the FBG sensor was approved to be survived.

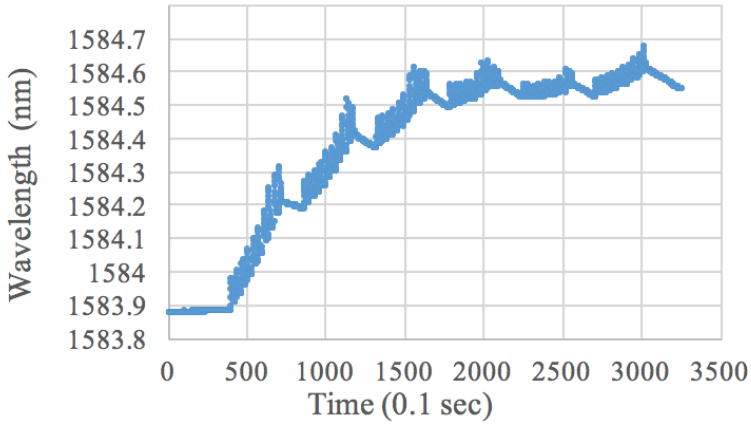

Figure 7. Monitored Bragg wavelength changes during thermal spraying coating process.

2.4. 1D Corrosion Assessment Using Embedded FBG Sensors

After the FBG sensors embedded inside the coatings, to assess the corrosion, the relationship between the FBG measurements to the corrosion needs to be established. This section establishes the relation between the FBG measured strains to the corrosion beneath the coating and also the resulted corrosion cracks, if any.

Figure 7 shows that when corrosion reaction occurs in the steel substrate or in the metallic coatings, the corrosion products expand and push the coatings upward, resulting in strain changes on the embedded FBG sensors in the coatings, as ε_i, that can be monitored by the Bragg wavelength change of the FBG sensors, as λ_i, where $_i$ is corrosion time step.

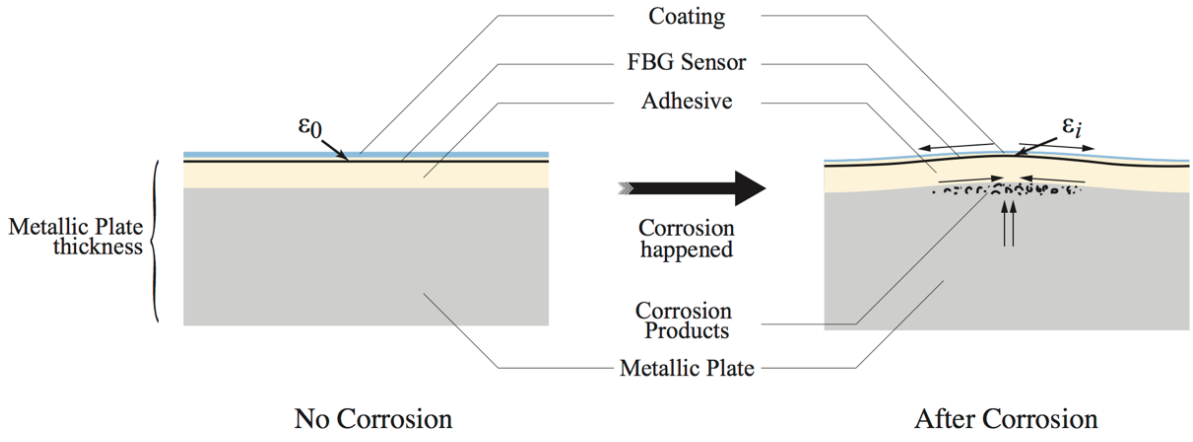

Figure 8. Cross-section of corrosion assessment system.

To simplify the analysis, since the FBG sensor is packaged using steel tubes or similar for protection, the corrosion induced strain to the constrained FBG sensor inside coating and adhesive if any during embedment, can be analyzed using a simply supported beam theory. Two assumptions are made based on a typical localized corrosion [20, 102, 103]:

1) The corrosion analyzed in this study is a pitted (localized) corrosion so its corrosion production is accumulated within a relatively small area comparing to the total span of the packaged FBG sensor;
2) The expansion of corrosion products mainly accumulates vertically.

Therefore, as shown in Figure 9, based on the first assumption, the corrosion product expansion can be simulated as a point load (F) induced displacement, Δ, in the middle of the FBG sensor as the coating detaching away from the steel substrate due to the presence of corrosion products and at the same time other coatings remain attaching to the steel substrate.

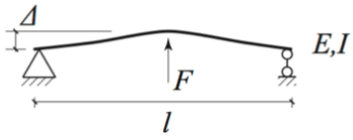

Figure 9. Simple supported beam system.

Based on fundamental structural analysis theory, the corrosion induced strain monitored by the embedded FBG sensor, ε_i, and the displacement in the middle of the total span, Δ, can be then calculated as:

$$\varepsilon_i = \frac{\sigma}{E} = \frac{My}{EI} = \frac{ly}{2EI} \cdot F \tag{8}$$

and

$$\Delta = \frac{Fl^3}{48EI} = \frac{l^3}{48EI} \cdot F \tag{9}$$

where σ is the normal stress at a distance y from the neutral surface of bending, M is the resistance moment of the section at middle span, E is the Young's modulus of adhesive, I is the moment of inertia, l is the span of beam, y is half of the height of cross-section, and F is the induced concentrated force by corrosion at the middle of total span. Let $k_1 = ly/(2EI)$ and $k_2 = l^3/(48EI)$. Then the relation between the center displacement (Δ) to that of the strain on the embedded FBG sensor (ε_i) can then be expressed as:

$$V = k_3 \cdot \Delta = (\frac{k_2 k_3}{k_1}) \cdot \varepsilon_i \quad (10)$$

Based on the second assumption mentioned above, the total volume of corrosion products, V, would be linear proportional to the corrosion induced center displacement on the FBG sensor (as volume increased linearly corresponding to the increase in height), which can be described as:

$$V = k_3 \cdot \Delta = (\frac{k_2 k_3}{k_1}) \cdot \varepsilon_i \quad (11)$$

where k_3 is the linear scaling factor between volume of corrosion products and induced center displacement.

As described in the definition, the corrosion rate (CR) of a metal is the derivative of the total lost weight of metal (m) due to corrosion with respect to time (t), and the weight is the product of the density of metal (ρ) and volume (V) of the metal. When the type of metal is determined, the density of metal and the expansion factor (k_4) between volume of corrosion products (V), and lost volume of metal due to corrosion (V'), are constants. Hence, with Equation (11), the relationship between corrosion rate and strain monitored by the embedded FBG sensor can be drawn as below:

$$\mathrm{CR} = \frac{\mathrm{d}m}{\mathrm{d}t} = \rho\frac{\mathrm{d}V'}{\mathrm{d}t} = \rho k_4\frac{\mathrm{d}V}{\mathrm{d}t} = \frac{\rho k_2 k_3 k_4}{k_1}\cdot\frac{\mathrm{d}\varepsilon_{\mathrm{i}}}{\mathrm{d}t} \tag{12}$$

Combing Equation (7) ~ (12), the measured Bragg wavelength changes of the embedded FBG sensors can then be related to the corrosion rate of the thermal sprayed coatings or the coated subtracts as below:

$$\mathrm{CR} = \frac{\rho k_2 k_3 k_4}{\lambda_B k_1(1-P_e)}\cdot\frac{\mathrm{d}\Delta\lambda}{\mathrm{d}t} = \alpha\cdot\frac{\mathrm{d}\Delta\lambda}{\mathrm{d}t} \tag{13}$$

where CR is the corrosion rate, $\Delta\lambda$ is the Bragg wavelength change measured by the embedded FBG sensor, and α is the sensitivity of the sensor toward corrosion rate of metals which can be calibrated with known corrosion rate of one certain material.

With known substrate and coating material properties, known FBG embedment locations and size of the steel pipes, the parameters, ρ, k_1, k_2, k_3 , k_4, λ_B, and P_e in Equation (13) can be determined and the FBG center wavelength to corrosion rate sensitivity, α, can be estimated. In addition, the laboratory accelerated corrosion tests also can measure the corrosion rate for a particular material and coating, which can be used to calibrate the corrosion measurement sensitivity of the FBG sensors. The calibrated model can then be applied to various thermal sprayed coatings in field for corrosion monitoring of coated steel structures. More importantly, as corrosion further develops, cracks will be initialized inside coating resulting in coating breakages, which will release the induced constrain of FBG sensors and change the boundary conditions of the FBG sensor for existing corrosion products. The lift-up phenomenon mentioned above will disappear, resulting in a sudden drop in Bragg wavelength of FBG sensors, which can be notified and used to monitor the cracks on coatings.

2.5. Summary

In this chapter, the corrosion risk assessment system design process was demonstrated. Started from the corrosion principle and the FBG sensor's working principle, the interaction between the corrosion products and corrosion risk assessment system had been discussed. The FBG sensors were embedded and protected comprehensively in designed system. The mathematical model had shown a positive relationship between the corrosion rate and the Bragg wavelength change rate of embedded FBG sensors. The presence of corrosion products, which has significantly increased volume compared with substrate material, causes FBG sensor to be lifted, resulting in an increase in wavelength of FBG sensor. The wavelength change rate (slope of wavelength changes curve) has a positive relationship with the production rate of corrosion products, which directly related to the corrosion rate.

3. EXPERIMENTAL VALIDATION FOR CORROSION ASSESSMENT

To validate the corrosion assessment system developed in Chapter 2 based on the embedded FBG sensors in coatings for steel pipelines, in this chapter, systematic laboratory experiments were conducted to measure corrosion rate using both electrochemical methods and embedded FBG sensors for coated steel plates and pipe samples using different coatings such as HVOF thermal sprayed Al-Bronze coating, wire arc Al-Zn coatings, and soft coatings. The electrochemical method is used to test the corrosion rate for bare steel and the associated different coatings for a reference corrosion rate to compare with the developed sensing technology for corrosion measurements. Table 2 showed the detail test matrix for the coated structure corrosion assessment used in this study. A total of 15 test samples were tested in this chapter to validate the effectiveness of the developed corrosion evaluation system.

Table 2. Test sample matrix.

Substrate	Coatings	Electrochemical Method	FBG Sensors
Steel Plate Samples	Bare steel	Sample B	Sample #5
	HVOF thermal sprayed Al-Bronze coating	Sample #3	Sample #1 ~ #4
	Wire arc Al-Zn coating	Sample A#4	Sample A#1 ~ A#3
	Soft coating	*	Sample S#1 ~ S#3
Steel Pipe Samples	HVOF thermal sprayed Al-Bronze coating	*	Sample P#1 ~ P#2

Note: * - Not tested.

3.1. Corrosion Rate Measurement Using Electrochemical Approach

Electrochemical method is an existing common method to measure the corrosion rate of a metal material. Tafel test is one of the most commonly used electrochemical testing approaches for corrosion resistance evaluation of material for short term corrosion behavior [104-107]. It has

several advantages over traditional corrosion resistance measurement, for instances, shorter testing cycle and easier testing setup. In this study, a Gamry Reference 600 Potentiostat/Galvanostat/ZRA was used to perform the electrochemical tests and Tafel tests were performed to obtain the reference corrosion rates for coated samples using HVOF thermal sprayed Al-Bronze coating, wire arc Al-Zn coatings, and bare steel samples.

Since the corrosion by nature is one type of electrochemical reaction, the corrosion rate could be described by its reaction rate, or the electron transferring rate, i.e. the current between anode side and cathode side. In a typical Tafel test, the testing instrument generates a range of potential between the anode and cathode, by attached counter electrode and working electrode, to excite the oxidation reaction on anode aside and the reduction reaction on cathode side. At the same time, the instrument also records the current for each potential generated during this process. As a result, two current vs. potential curves, one for the anode side and the other for cathode side, was plotted in one graph, named as Tafel plot. Figure 10 showed a typical Tafel plot[108].

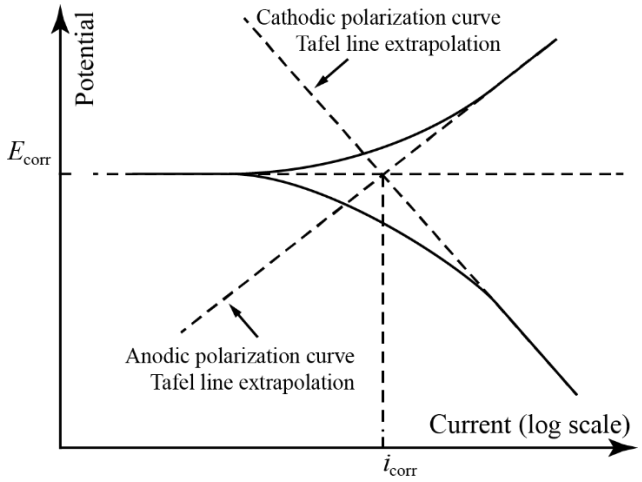

Figure 10. A typical Tafel plot graph.

After the Tafel plot was generated, to get the corrosion rate, the linear parts of anode and cathode side current vs. potential curves are used to find the balance point of anode and cathode

side chemical reaction, shown in Figure 10 as dashed line. At the balance point, the chemical reaction could continue without external interference, which means the current at the balance point is the corrosion rate of the testing metal. In Figure 10, the corrosion potential is E_{corr}, and the corrosion current is I_{corr}. The larger value of corrosion current indicates a less corrosion resistance or a larger corrosion rate, vice versa. Thus, the corrosion current can be calculated as follow:

$$I_{corr} = \frac{\beta_A \cdot \beta_C}{2.3R_P(\beta_A + \beta_C)} \tag{14}$$

where the β_A and β_C are known as Tafel constants, which are the absolute value of slope of linear part of anode and cathode side polarization curve when current axis is in log scale. R_p is the polarization resistance, which would be determined once the testing environment is settled down.

By fitting the linear part of Tafel plot graph, the Tafel constants, β_A and β_C, can be determined. With the value of polarization resistance (R_P) of the material, which determined by the material itself, and the two Tafel constants, corrosion rate can be calculated as follow:

$$CR = I_{corr} \cdot \frac{K \cdot EW}{d \cdot A} \tag{15}$$

where CR is corrosion rate, K is unit conversion factor, EW is the equivalent weight of tested material, d is density of tested material, and A is the testing area.

Figure 11 shows the Tafel test setup and Figure 11 shows the electrochemical test setup used in this study to measure the corrosion rate. In order to conduct electrochemical corrosion test on sample, a PVC pipe was attached to the sample and then filled with 3.5wt% NaCl solution to create free electron. After using epoxy to glue PVC pipe to the surface of the coated sample, a conductive wire connected to the bottom of the sample for connecting testing

instrument. A scan rate was set to be 0.1 mV/sec and the scan range was set to be ±250 mV vs. corrosion potential.

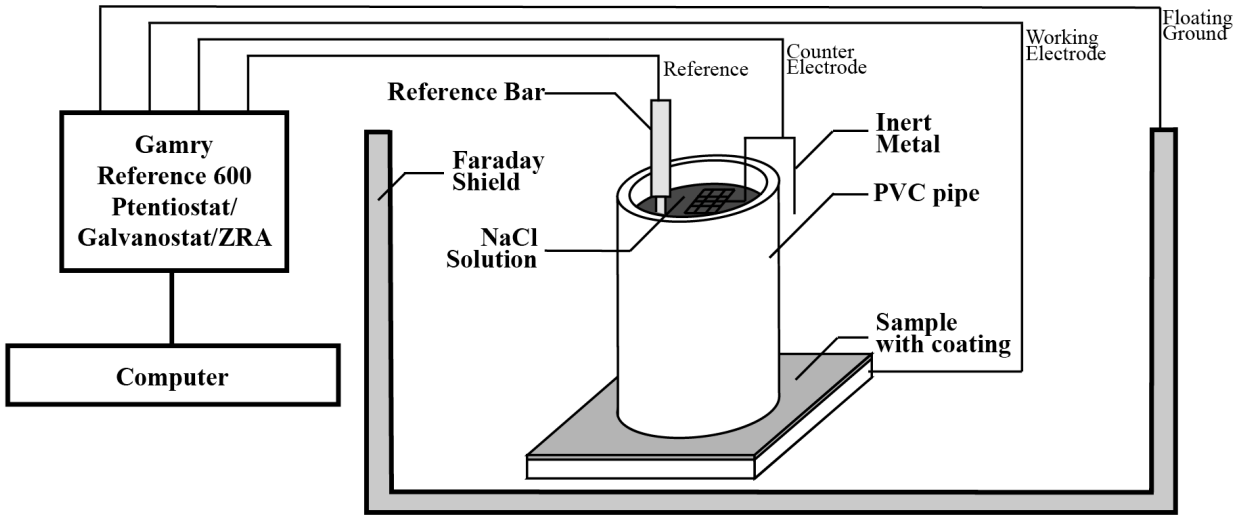

Figure 11. Sketched electrochemical corrosion test set-up.

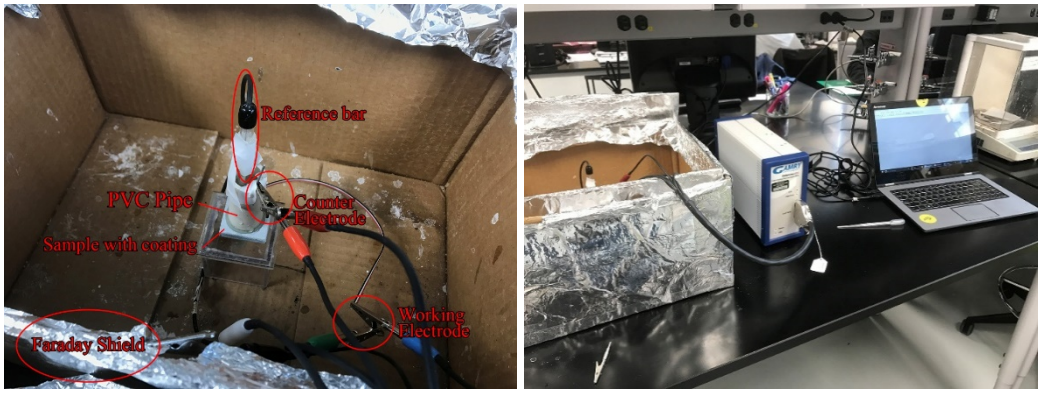

Figure 12. Experimental setup for electrochemical tests.

3.1.1. Tafel Test Results of HVOF Thermal Sprayed Al-Bronze Coated Sample

The Tafel plot of HVOF thermal sprayed Al-Bronze coated sample was shown in Figure 13. By using the linear fitting on the anode side polarization curve and cathode side polarization curve, parameters needed for corrosion rate calculation were obtained. The corrosion rate of the tested sample was calculated using Equation (15), and the results were listed in Table 3. The corrosion rate of the HVOF thermal sprayed Al-Bronze is measured to be 0.5054 mil/year.

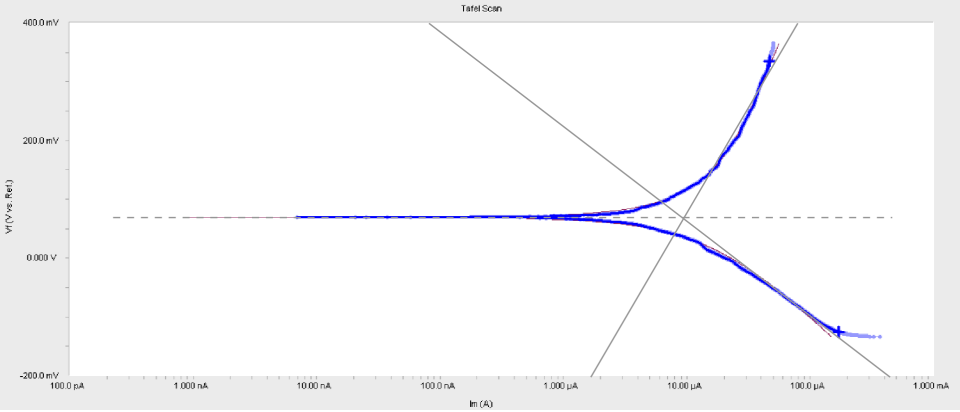

Figure 13. Tafel plot measurement result of HVOF thermal sprayed Al-Bronze coated sample.

Table 3. Parameters used for corrosion rate calculation in HVOF thermal sprayed Al-Bronze coated sample.

Notation	Value
I_{corr} / Corrosion Current in A	9.5 µA = 0.0000095 A
K / Unit Convert Constant	128800
W_{E} / Equivalent Weight in grams/equivalent	30
D / Density in g/cm^3	4.1
A / Sample area in cm^2	17.715
Corrosion Rate in mil/year	0.5054

3.1.2. Tafel Test Result of Wire Arc Sprayed Al-Zn Coated Sample

The Tafel plot of wire arc sprayed Al-Zn coated sample was shown in Figure 14. By using the linear fitting on the anode side polarization curve and cathode side polarization curve, parameters needed for corrosion rate calculation were obtained. The corrosion rate of the tested sample was calculated using Equation (15), and the result was listed in Table 4. Parameters used for corrosion rate calculation in wire arc sprayed Al-Zn coated sample. The corrosion rate of the wire arc sprayed Al-Zn coating is measured to be 0.086 mil/year.

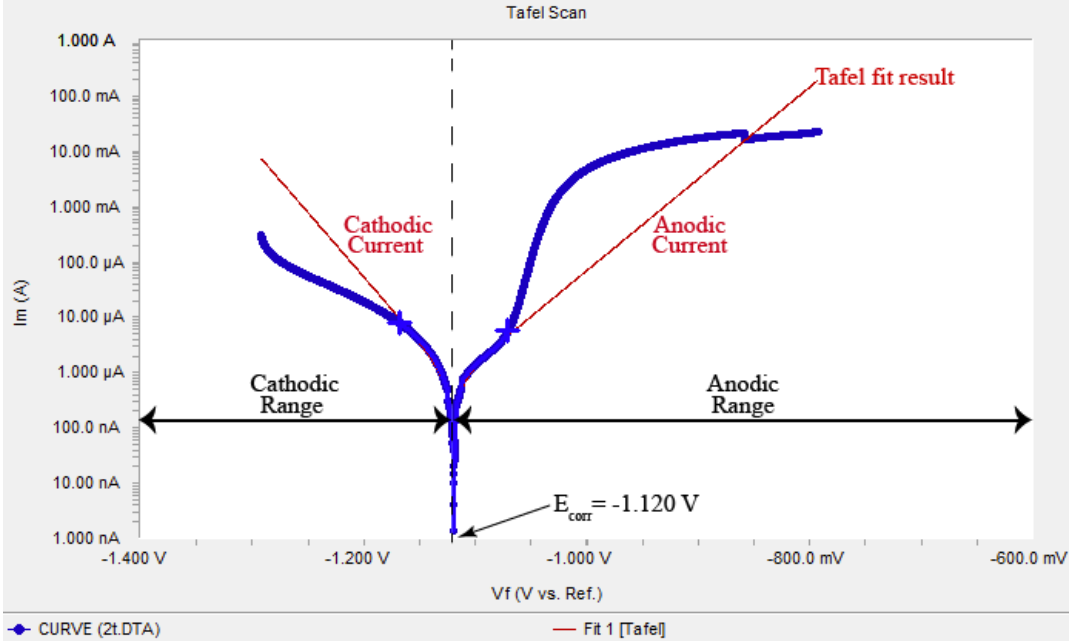

Figure 14. Tafel plot measurement result of wire arc sprayed Al-Zn coated sample.

Table 4. Parameters used for corrosion rate calculation in wire arc sprayed Al-Zn coated sample.

Notation	Value
I_{corr} / Corrosion Current in A	0.79 µA = 0.00000079 A
K / Unit Convert Constant	128800
W_E / Equivalent Weight in grams/equivalent	32
D / Density in g/cm3	6.9
A / Sample area in cm2	5.491
Corrosion Rate in mil/year	0.0860

3.1.3. Tafel Test Result of Bare Steel Plate Sample

The Tafel plot of wire arc sprayed Al-Zn coated sample was shown in Figure 15. Similar to the other two samples, Tafel fit was applied to the Tafel plot to get the parameters. Corrosion rate was calculated in Table 5. The corrosion rate of the bare steel is measured to be 1.5458 mil/year.

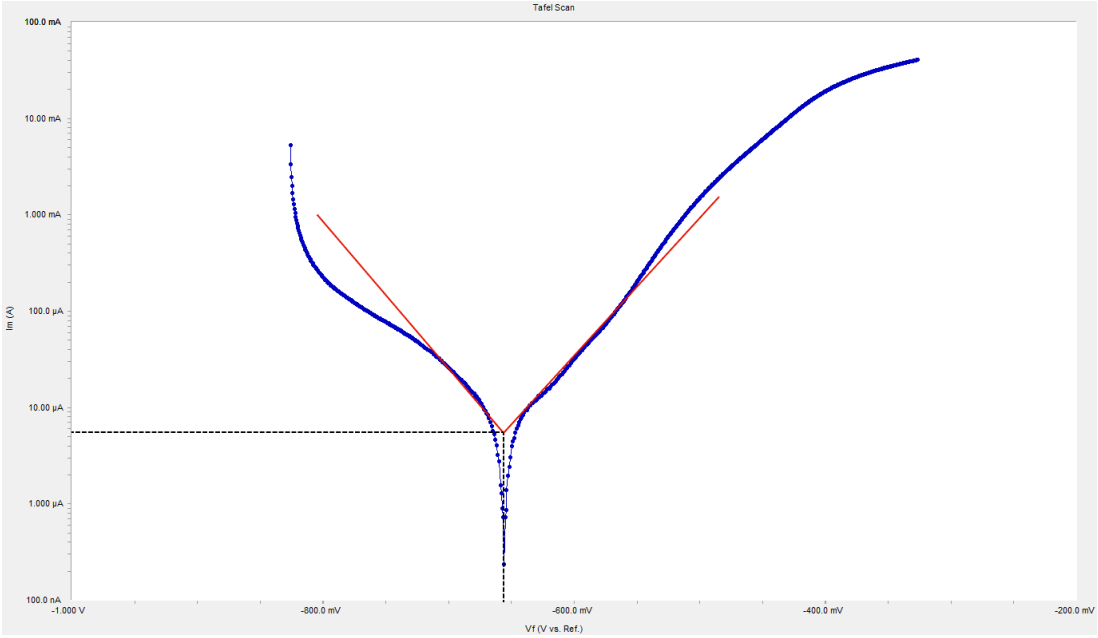

Figure 15. Tafel plot measurement result of Bare Steel Plate Sample.

Table 5. Parameters used for corrosion rate calculation in bare steel plate sample.

Notation	Value
I_{corr} / Corrosion Current in A	9.6 µA = 0.0000096 A
K / Unit Convert Constant	128800
W_{E} / Equivalent Weight in grams/equivalent	28
D / Density in g/cm3	7.9
A / Sample area in cm2	2.835
Corrosion Rate in mil/year	1.5458

3.1.4. Discussions

From the three Tafel test results, it was clearly that coatings could reduce the corrosion rate comparing to the bare steel. In addition to lowering the corrosion rate, the corrosion products of several metal, such as aluminum and zinc, would form a thin layer of firm sealing and isolate the base material from corrosive environment, stopping corrosion progress. This phenomenon is often known as passivation. Compared with the HVOF thermal sprayed Al-Bronze coating, wire arc sprayed Al-Zn coating had a lower corrosion rate, mainly because the wire arc sprayed coating had a lower porosity, and the passivation effect of aluminum and zinc. The Tafel test

results in this section also served as a calibration base for the proposed corrosion assessment system in the following sections.

3.2. Corrosion Performance Evaluation of HVOF Thermal Sprayed Al-Bronze Coating

With reference corrosion rate from the electrochemical tests, the corrosion performance of the steel plates with HVOF thermal sprayed Al-Bronze coating was also assessed using the embedded FBG sensors inside the coating through laboratory accelerated corrosion tests. Four HVOF thermal sprayed Al-Bronze coated samples with embedded FBG sensors were tested. A36 structure steel was used as substrate.

3.2.1. Experimental Setup

To create a corrosive environment for accelerate corrosion tests in laboratory, a PVC tube with a diameter of 2 inches was attached on top of each coated sample with embedded sensors using heavy duty epoxy adhesive and filled with 3.5wt% sodium chloride (NaCl) solution after the adhesive was fully cured. The experiments run for 6 days. A total of 5 samples (Sample #1 ~ #4 were coated samples and Sample #5 was uncoated sample as reference) were involved in the test. The center wavelength changes of the samples were continuously recorded during the test with a sampling rate of 10 Hz using data inquisitor (National Instrument PXIe-4844). Figure 16 shows the test setup. To identify the corrosion for each sample during the test, scheduled visual inspections for all the samples were also applied at 12:00 p.m. daily and pictures were taken.

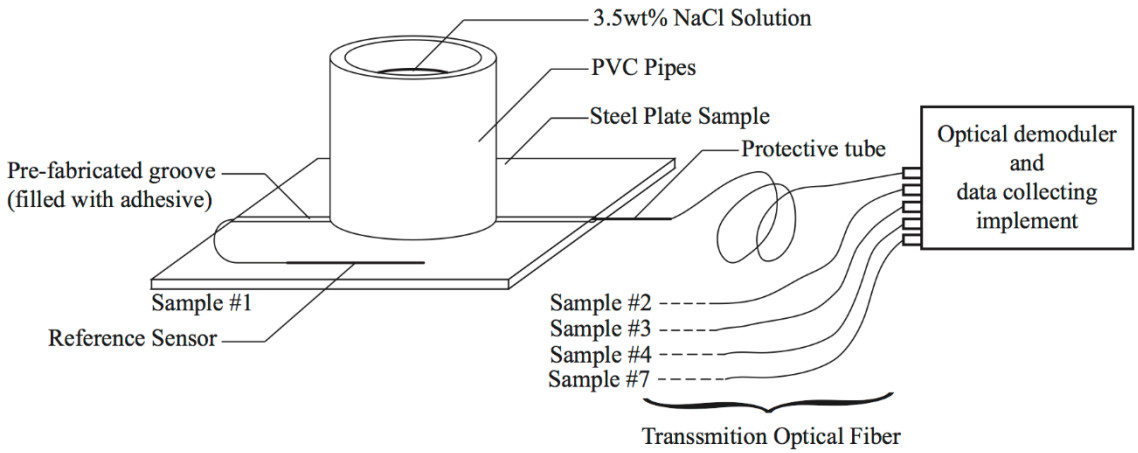

Figure 16. Corrosion test set-up for hard coated sample plates.

Figure 17 shows the Bragg wavelength changes during the test before the temperature compensation. After temperature elimination using Eq. (7), the Bragg wavelength changes was shown in Figure 18.

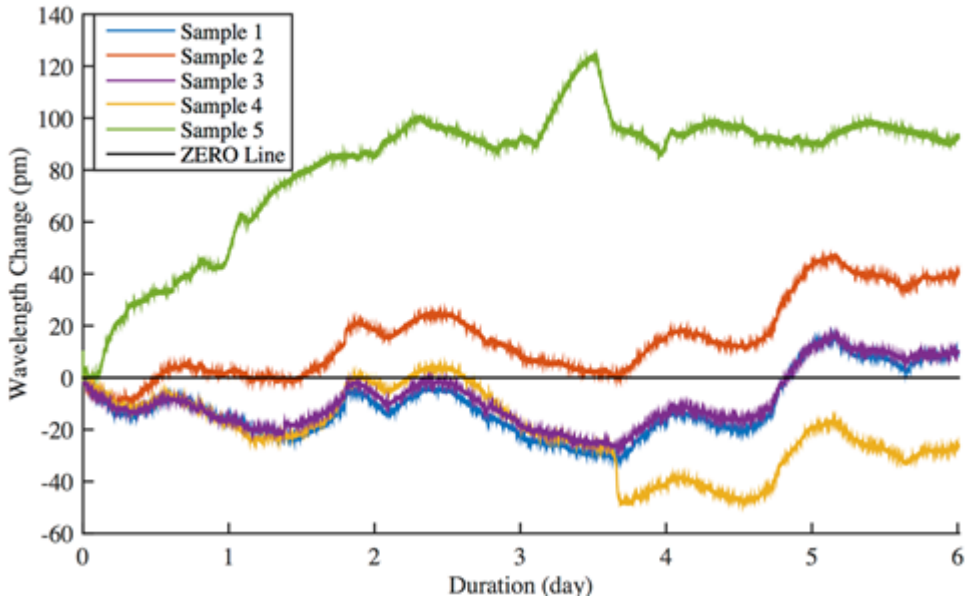

Figure 17. Bragg wavelength changes of embedded FBG sensors before temperature compensation.

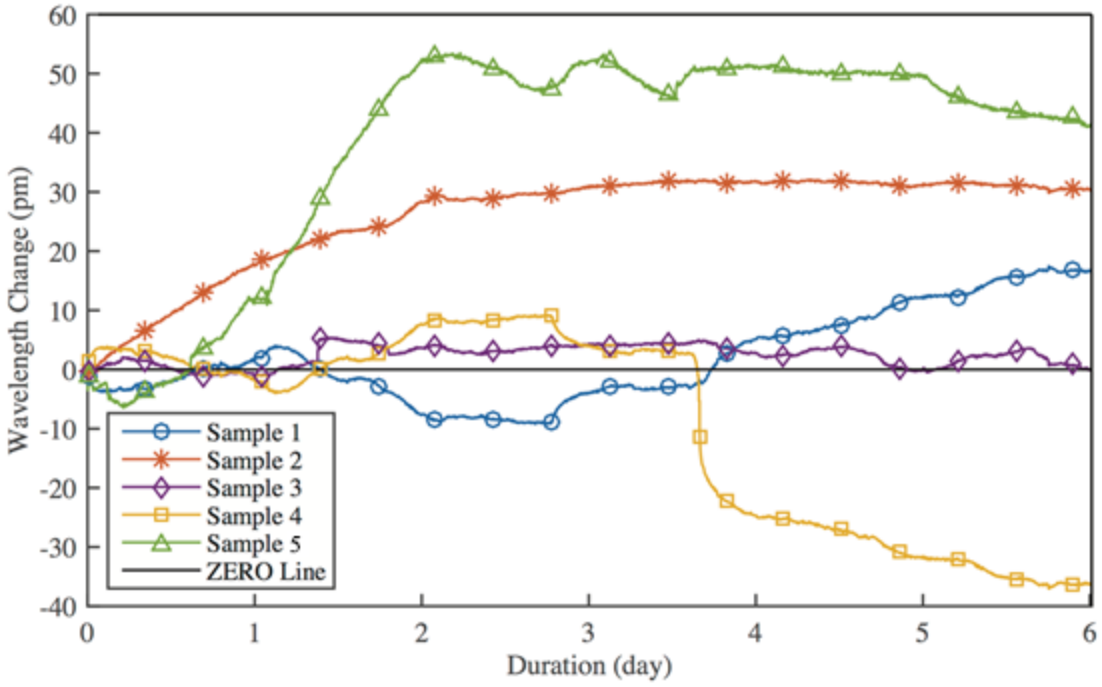

Figure 18. Bragg wavelength changes of embedded FBG sensors after temperature compensation.

Figure 19 to Figure 23 show the visual inspection result for all of samples during the test. From the visual inspection of all samples in Figure 19 ~ Figure 23, new corrosion products were found in Sample #1, #2, #4, and #5; and Sample #4 was severely corroded, in which coating cracks were observed.

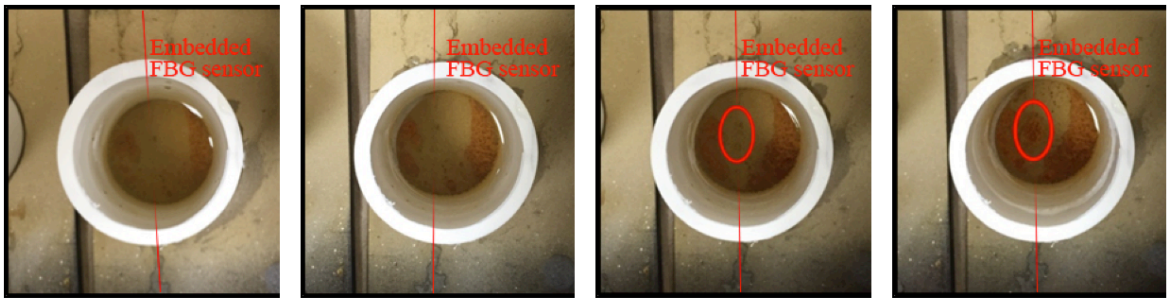

(a) Day 1 (b) Day 2 (c) Day 3 (d) Day 6

Figure 19. Visual inspection of Sample #1.

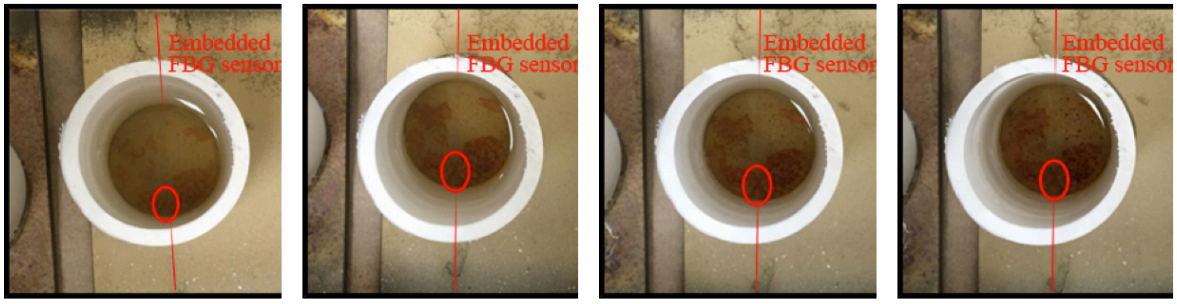

(a) Day 1 (b) Day 2 (c) Day 3 (d) Day 6

Figure 20. Visual inspection of Sample #2.

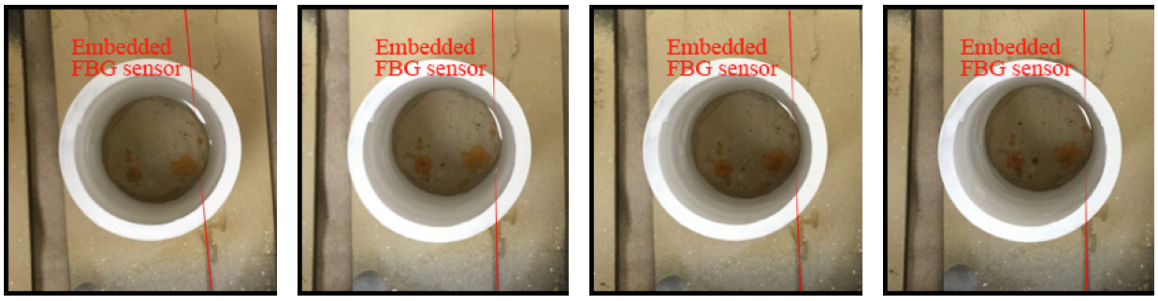

(a) Day 1 (b) Day 2 (c) Day 3 (d) Day 6

Figure 21. Visual inspection of Sample #3.

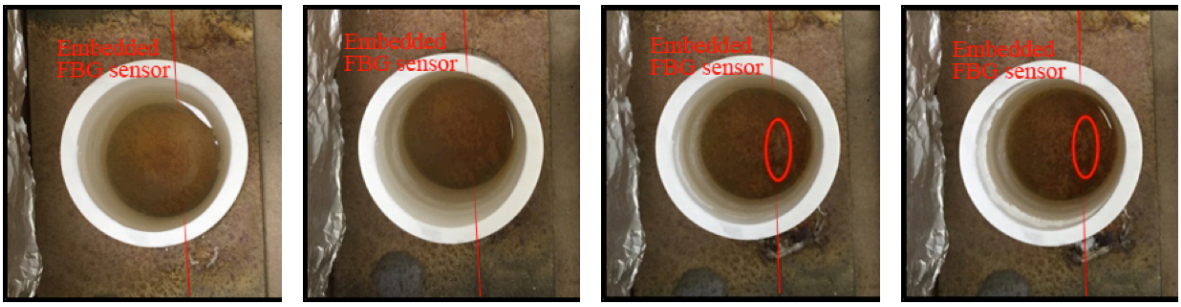

(a) Day 1 (b) Day 2 (c) Day 3 (d) Day 6

Figure 22. Visual inspection of Sample #4.

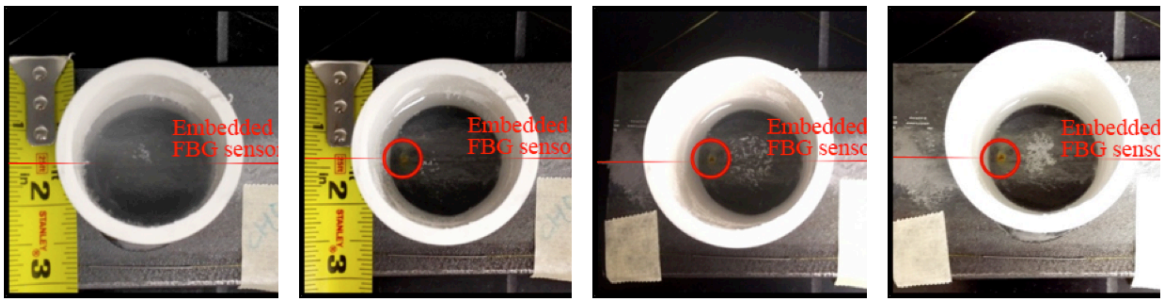

(a) Day 1 (b) Day 2 (c) Day 3 (d) Day 6

Figure 23. Visual inspection of Sample #5.

3.2.2. Discussion

From the visual inspection, it was observed that Sample #1, #2, and #5 were following a similar pattern, as those three samples have newly formed pitting corrosion. Comparing the visual inspection result with Bragg wavelength change graph, it was also observed that the Bragg wavelength changes of Sample #1, #2, and #5 were following a 3-stage corrosion phenomenon shown in Figure 24[20]. The Bragg wavelength changes of Sample #1, #2, and #5 were shown in Figure 25.

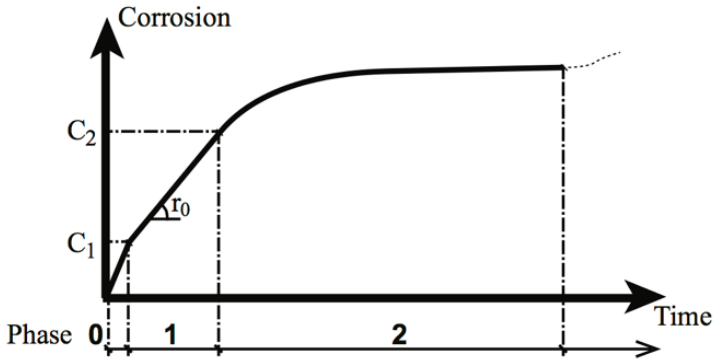

Figure 24. Multi-phase phenomenological corrosion time model.

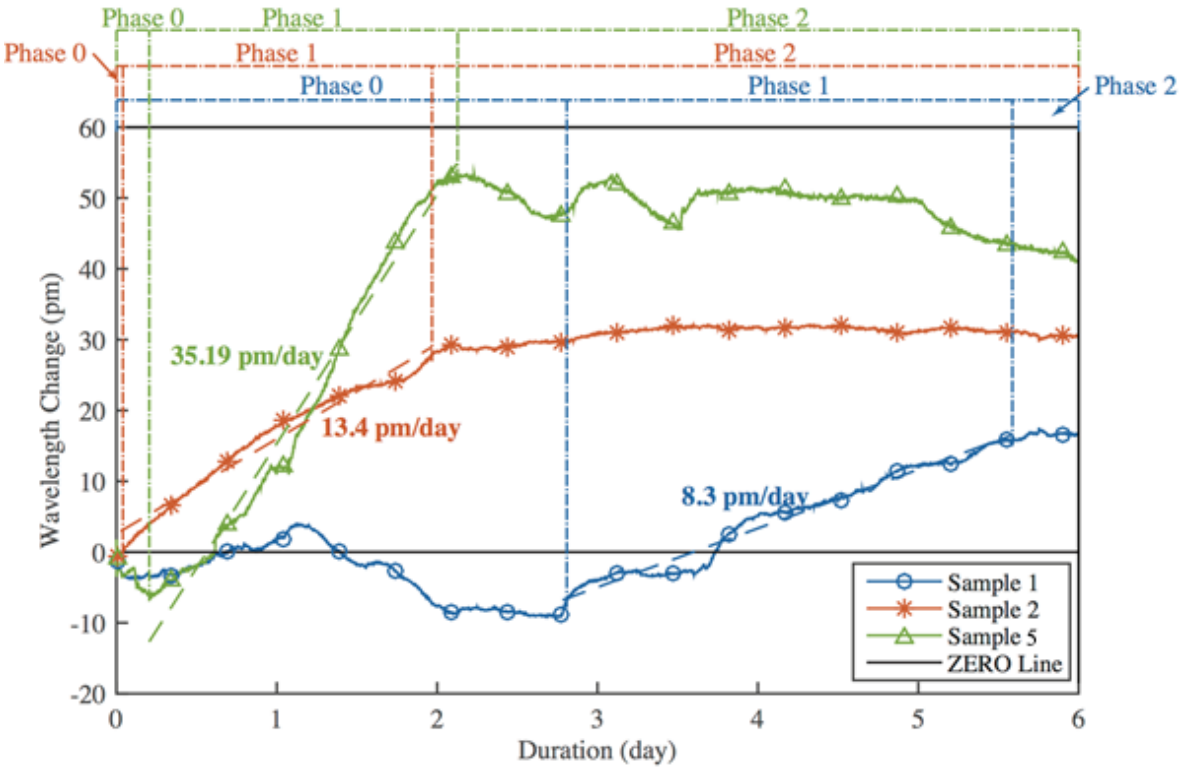

Figure 25. Bragg wavelength change vs time of Sample #1, #2, and #5.

The 3-stages identified from Figure 24 can be described as the following phases:

Phase 0, Short-term influences: at this phase, corrosion is activated, and corrosion products are filling the pores between adhesive and FBG sensor. As a result, compression is carried out to FBG sensor, causing a drop in wavelength curve.

Phase 1, High corrosion rate: Oxygen surrounded at corrosion area is consumed and more oxygen is rapidly absorbed in water. This results in high corrosion rate. Due to the limitation of space, corrosion products are tending to lift the embedded FBG sensors, causing an increase in wavelength. In this case, the slope of wavelength change curve in phase 1 reflect the production rate of corrosion products. Sample #1 and Sample #2 have lesser slope values (8.3 pm/day and 13.4 pm/day, respectively) than Sample 5 (35.19 pm/day), which indicates lower productivity of corrosion products and thus lower corrosion rates. This result matches the fact that Sample #1 and Sample #2 have higher corrosion resistance as a result of HVOF thermal spray coating. As

described in the multi-phase corrosion model, the corrosion is linear accumulated, and the curve slope is assumed to be r_0. There was a linear relationship between corrosion rate and the curve slope which could be shown as follow:

$$\mathrm{CR} = \alpha \cdot k \tag{16}$$

where CR is the corrosion rate of sample, k is the wavelength change curve of sample, and α is the gradient; as the bare steel sample tested with Tafel test in the previous section has a corrosion rate of 1.5458 mil/year, α can be determined by calculation with data from Sample 5:

$$\alpha = \frac{\mathrm{CR}_5}{k_5} = \frac{1.5458\ \mathrm{mil/year}}{35.19\ \mathrm{pm/day}} = 4.393 \times 10^{-2}\ \mathrm{mil \cdot day/(pm \cdot year)}$$

Thus, the corrosion rate of Sample 1 and Sample 2 could also be calculated as follow:

$$\mathrm{CR}_1 = \alpha \cdot k_1 = 4.393 \times 10^{-2} \times 8.3 = 0.365\ \mathrm{mil/year}$$

$$\mathrm{CR}_2 = \alpha \cdot k_2 = 4.393 \times 10^{-2} \times 13.4 = 0.589\ \mathrm{mil/year}$$

These two values were very close to the corrosion rate of the HVOF thermal sprayed Al-Bronze coated sample tested using Tafel test (0.5054 mil/year), which indicates the curve fitting of monitored data have potential to serve as a candidate in corrosion rate monitoring on site. Furthermore, Sample #1 has a lesser corrosion rate than Sample #2, indicating a better coating quality in Sample 1.

Phase 2, Stabilized corrosion progress: Oxygen starts to diffusion through the corrosion products to further corrode the steel. However, at this phase, oxygen diffuses slower than phase 1 so the corrosion rate is lowered, and the amount of corrosion product is in metastable. As the corrosion products further develop and alternate and adhesive been broken through, strain caused by corrosion products slowly evanesce, and the remaining sensor reading on wavelength change curve is primarily remnant stress.

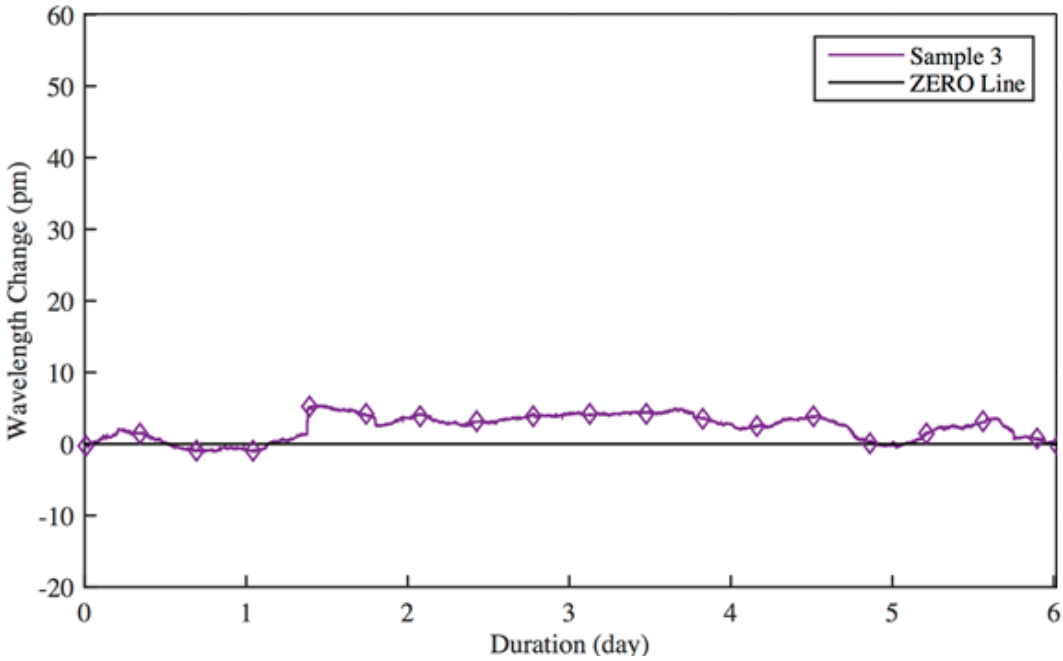

Figure 26. Bragg wavelength change of Sample #3 with no corrosion happened on top of sensor during the six-day corrosion test.

Figure 21 showed the visual inspection Sample #3 and Figure 26 showed the Bragg wavelength change of FBG sensor embedded in Sample #3. It can be seen that even though the two pitting corrosion existed from the beginning of the test, no additional corrosion happened during the 6-day test on top of the sensor of Sample #3. The coating condition and corrosion were not further developed from the day 1. And the wavelength change curve of Sample #3 was also stabilized with no dramatic change during the 6-day accelerated corrosion test.

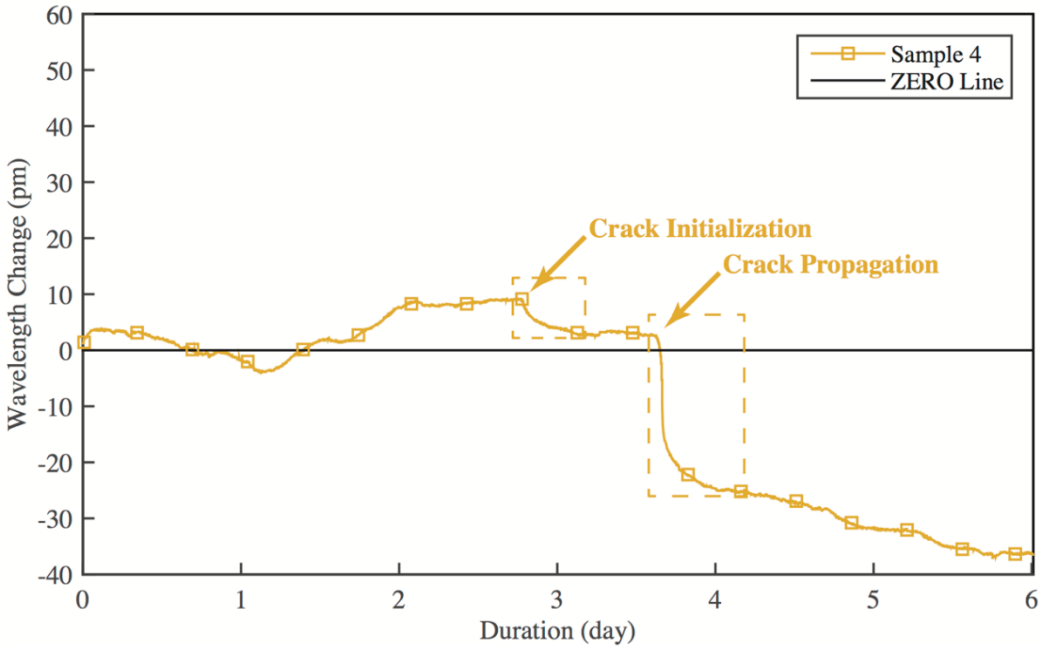

Figure 27. Bragg wavelength change of Sample #4 during the six-day corrosion test.

Figure 22 showed the visual inspection Sample #4 and Figure 27 showed the Bragg wavelength change of FBG sensor embedded in Sample #4. As stated before, a Tafel test for obtaining the corrosion rate of the coatings was performed in Sample #4 prior to the start of accelerated corrosion test. As a result, Sample #4 was contaminated by the Tafel test and severely corroded during the accelerated corrosion test. From day 3, a crack on coating caused by the corrosion can be observed, and it was continuing to grow in the next several days. A concentrated severe corrosion in the center can be seen in day 6.

With the result of visual inspection, it can be clearly pointed out that the Sample #4 had already passed Phase 0 and Phase 1 when the accelerated corrosion test started. The two considerable drops in the wavelength change curve of Sample #4 indicate the occurrence of two coating breaks (as shown in Figure 27).

The results of calculation and analysis supported the potential that the proposed corrosion monitoring system could serve as an effective way of real-time corrosion rate monitoring on-site.

Bragg wavelength change analysis could also be used as a strong tool in real-time coating condition monitoring.

3.3. Corrosion Performance Evaluation in Wire Arc Sprayed Al-Zn Coating

With successful corrosion performance evaluation of the steel plates with HVOF thermal sprayed Al-Bronze coating, wire arc sprayed Al-Zn coating was also assessed using the embedded FBG sensors inside the coating through laboratory accelerated corrosion tests. Three samples with wire arc sprayed Al-Zn coating were tested using the same experiment setup as for HVOF thermal sprayed Al-Bronze coating to further evaluate the coating quality and capability of corrosion assessment system. A36 structure steel was also used as substrate.

3.3.1. Experimental Setup

For the three wire arc sprayed Al-Zn coated samples, the coating thickness varied between samples. As shown in Figure 28, three samples were noted as Sample #A1, #A2, and #A3. The coatings on Sample #A1 and #A2 had thickness of 2mm, and the coating on Sample #A3 had a thickness of 1.5mm. Before the accelerated corrosion test was conducted, PVC pipes were also attached on top of each coated sample using heavy duty epoxy adhesive by the same method as previous tests to keep consistency with the HVOF thermal sprayed Al-Bronze coated samples, as shown in Figure 29. Figure 30 showed the overall setup for the accelerated corrosion test. The accelerated corrosion test had run for two weeks, and the NaCl solution used in the test had a concentration of 3.5wt%.

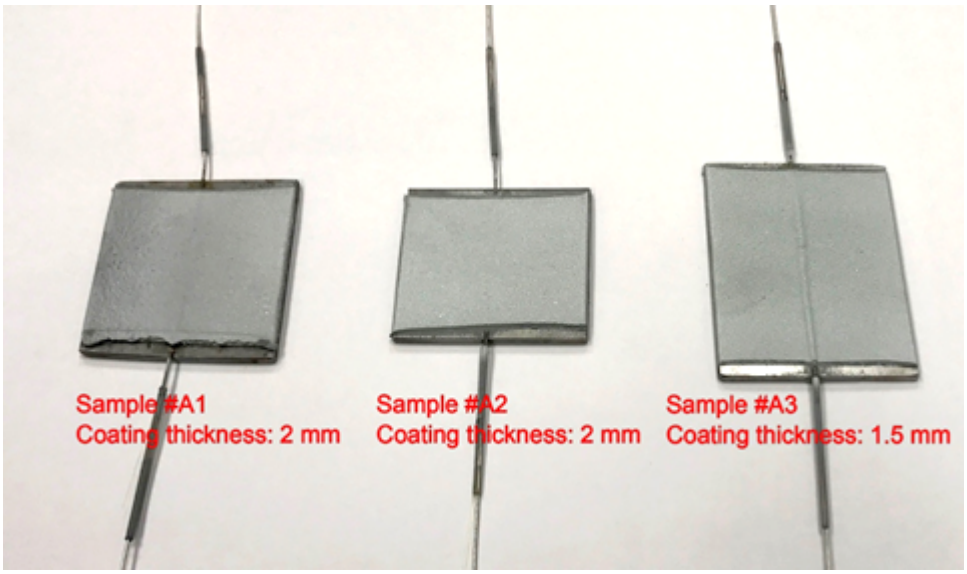

Figure 28. Three coated samples with FBG sensor embedded before accelerated corrosion test.

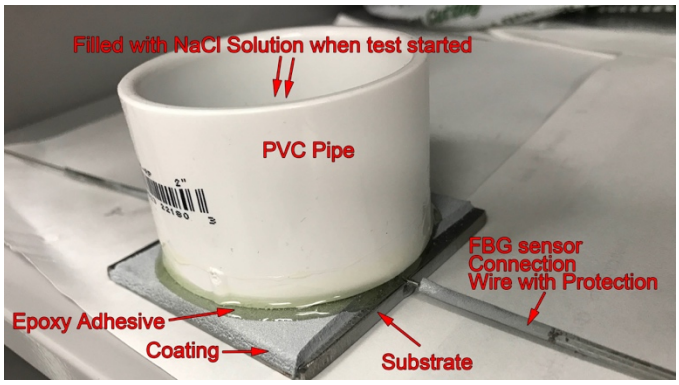

Figure 29. Sample attached with PVC pipe.

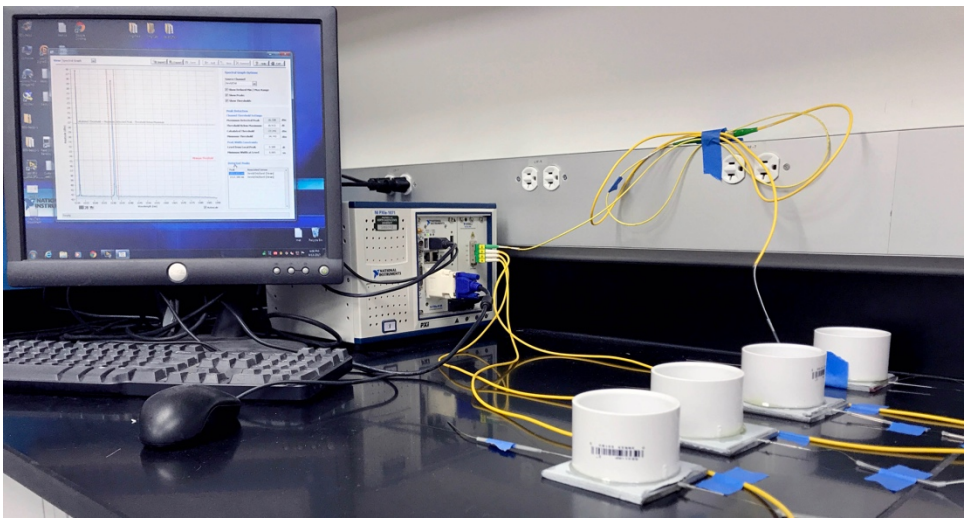

Figure 30. Corrosion testing setup for wire arc sprayed Al-Zn coating.

Visual inspections were scheduled daily at 12:00pm each day to spot the corrosion and record corrosion progress. In Figure 31, data collected from embedded corrosion monitoring system together with the data collected from the temperature compensation sensor during the two-week period was illustrated, and the data after temperature compensation was shown in Figure 32. Visual inspection result had been shown in Figure 33.

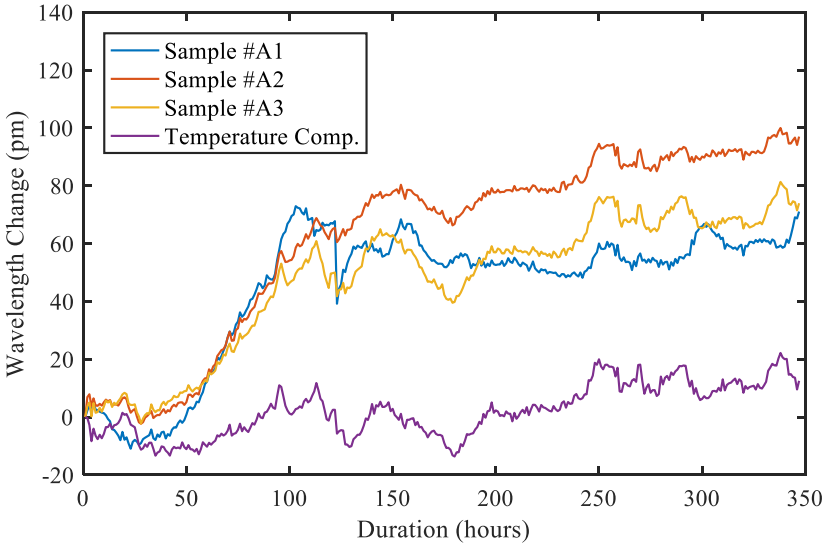

Figure 31. Bragg wavelength of embedded FBG sensors with wire arc sprayed Al-Zn coating before eliminating temperature effect.

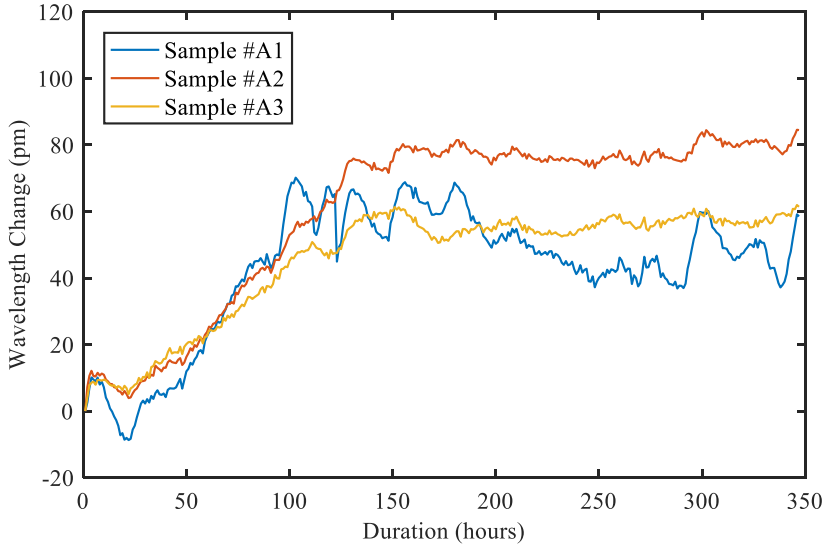

Figure 32. Bragg wavelength of embedded FBG sensors with wire arc sprayed Al-Zn coating after eliminating temperature effect.

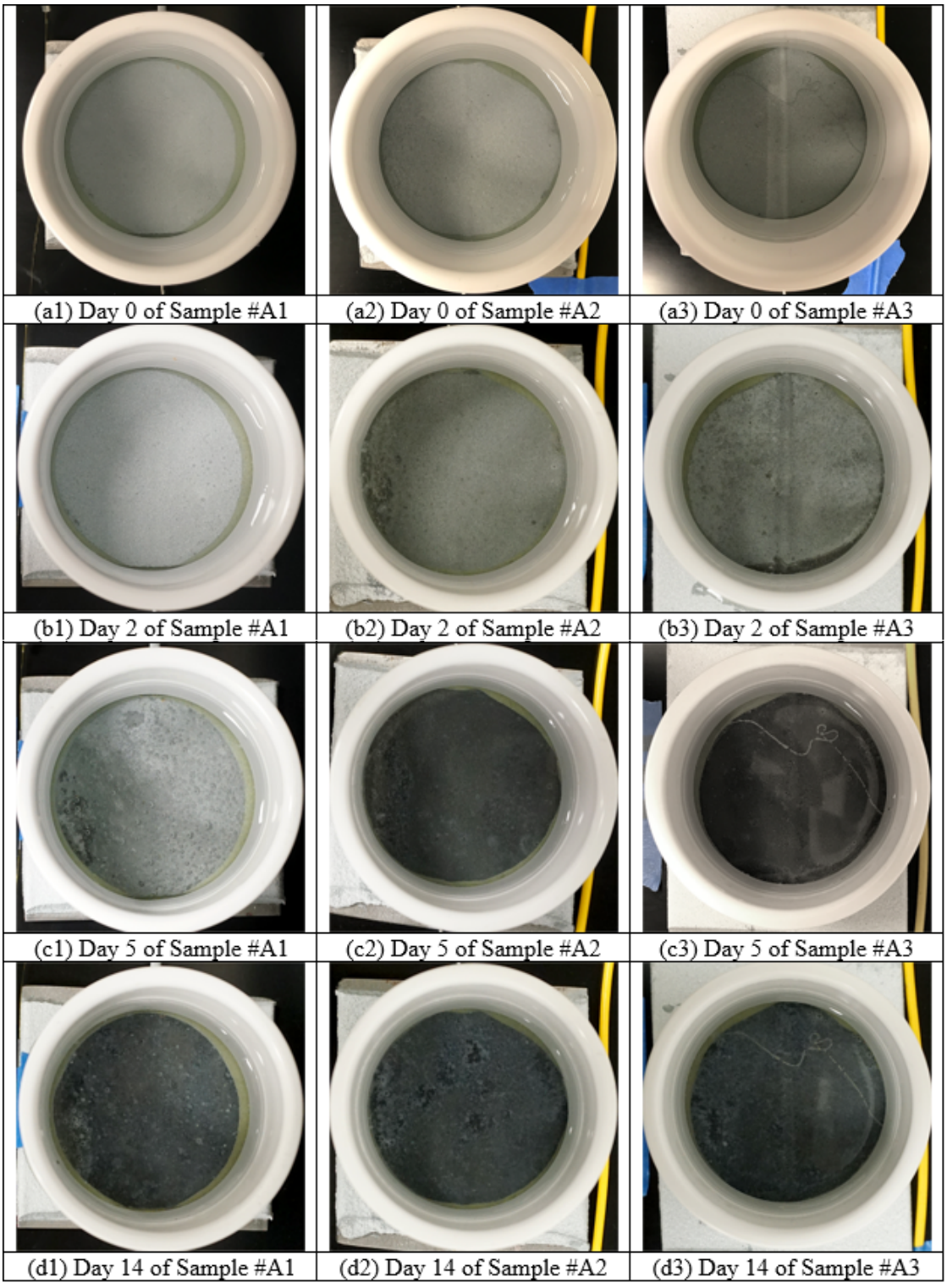

Figure 33. Visual inspection result for Sample #A1, #A2, and #A3.

3.3.2. Discussion

By using the same corrosion multi-phase model in Section 3.2, the corrosion rate of Sample #A1, #A2, and #A3 could be calculated using the linear increase part of the Bragg wavelength change graph, as shown in Figure 34. Since the coating property had changed from the previously performed testing, the linear proportional parameter α has to be re-calibrated.

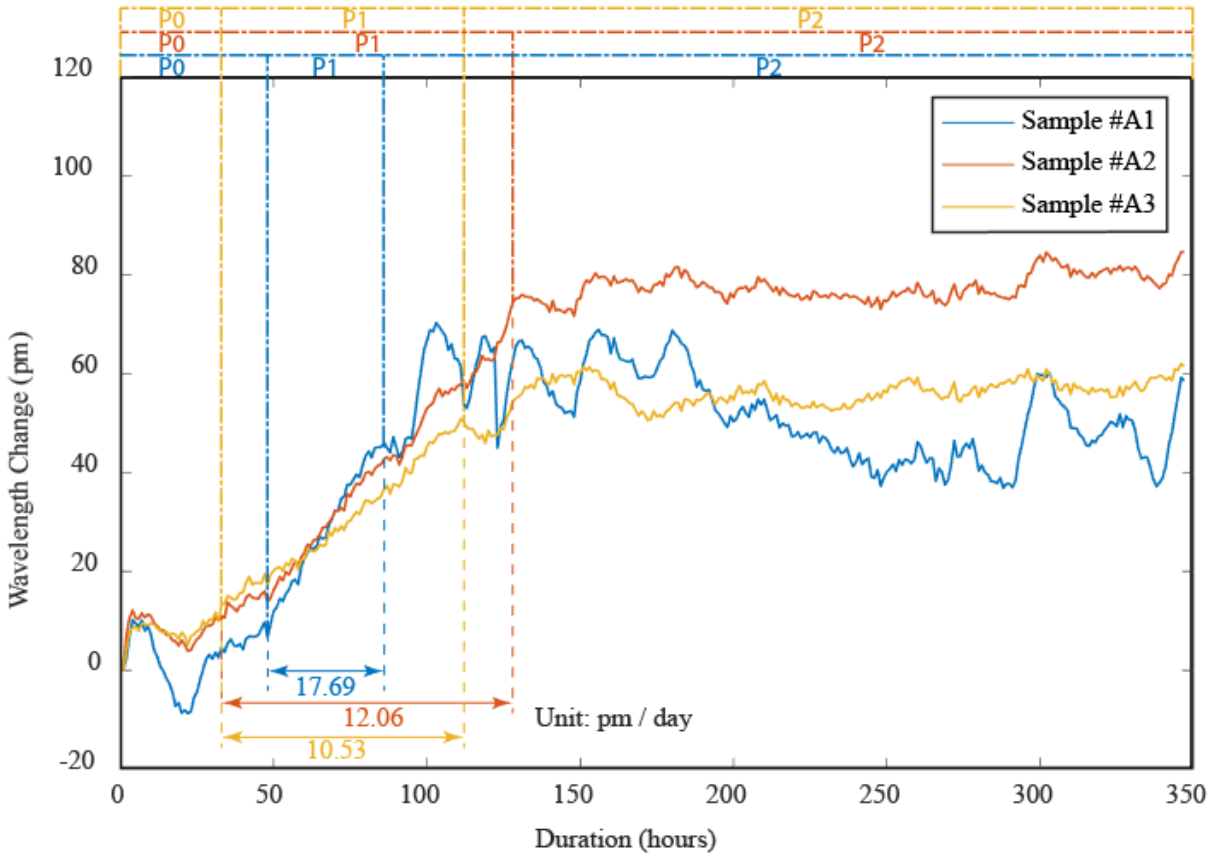

Figure 34. Bragg wavelength of embedded FBG sensors with wire arc sprayed Al-Zn coating with linear increase part marked.

In Figure 34, it was observed that there were multiple spikes on curve of Sample #A1 at range from 95 hours to 200 hours, indicating the coating structure had been severely corroded. From the visual inspection pictures shown in Figure 33, it was also confirmed that at bottom left corner of the sample, severe corrosion had attacked the coating, and started from day 5, the coating delaminated from the substrate. This also caused a higher corrosion rate for Sample #A1,

comparing with Sample #A2 and #A3. Possible reason of higher corrosion rate of Sample #A1 might be a higher porosity of coating, or unevenly applied coating. The final corrosion rate of the tested three samples are listed in the Table 6. The average corrosion rate of the wire arc Al-Zn coating is 0.0859 mil/year measured from the embedded FBG sensors. The calculation results suggested that proposed corrosion assessment system could serve as an effective way of real-time corrosion rate monitoring on-site.

Table 6. Corrosion rate of tested wire arc sprayed Al-Zn coated samples.

Sample Number	Sample #A1	Sample #A2	Sample #A3	All Sample Average
Corrosion Rate (mil/year)	0.1132	0.0772	0.0674	0.0859

3.4. Corrosion Performance Evaluation in Soft Coating

With successful corrosion performance evaluation of the steel plates with HVOF thermal sprayed Al-Bronze coating and wire arc sprayed Al-Zn coating, the performance of soft coating was also assessed using the embedded FBG sensors inside the coating through laboratory accelerated corrosion tests. Three samples with soft coatings applied were tested. A36 structure steel was also used as substrate.

3.4.1. Experimental Setup

Three steel plate samples with soft coating were noted as Sample #S1, #S2, and #S3. The soft coating used in the test was epoxy (Duralco 4461). One layer of epoxy was applied on surface of the base material as soft coating. FBG using the same packaging method was embedded before the soft coatings were applied. After the soft coating layer was fully cured, an PVC pipe with a diameter of 2 inch was fixed on top of the location of sensor by Loctite heavy duty epoxy adhesive then filled with 3.5wt% NaCl solution to create corrosive environment for

sensing area. The preparation procedure of the tested three samples were all the same. An additional temperature compensation sample was made beside Sample #S3, and it was not filled NaCl solution. Experiment setup has been shown in Figure 35.

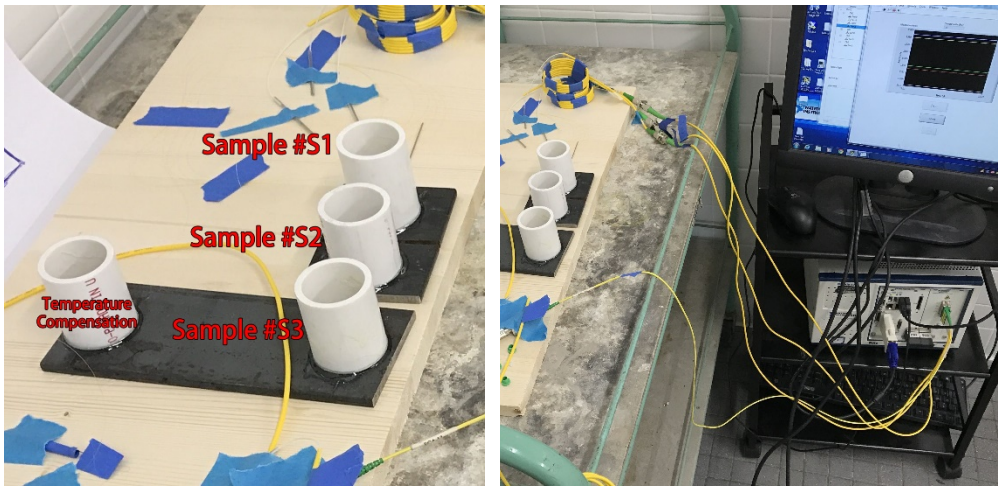

Figure 35. Corrosion monitoring system performance experiment for samples with soft coatings.

Due to strong corrosion resistance of the soft coating, the accelerated corrosion experiment run for 6142 hours (256 days) in total. The center wavelength change collected from FBG sensors were shown in Figure 36 and Figure 37.

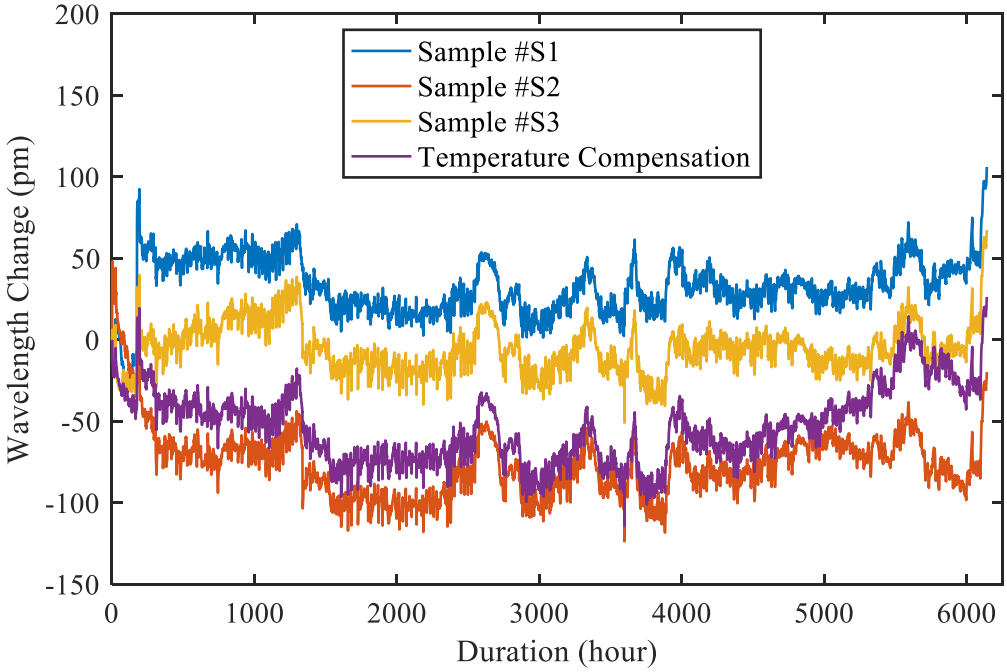

Figure 36. Bragg wavelength of embedded FBG sensors with soft coating before eliminating temperature effect.

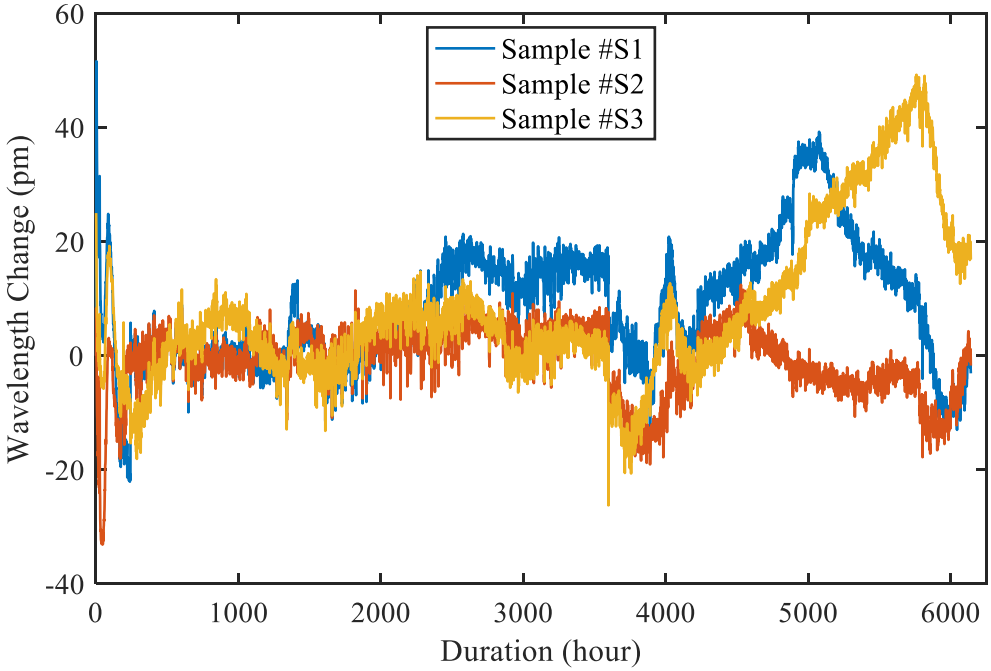

Figure 37. Bragg wavelength of embedded FBG sensors with soft coating after eliminating temperature effect.

Because of the nature of soft coating, if it was not damaged, it can isolate the substrate from corrosive environment outside. Thus, corrosion cannot get initiated without the damage of soft coating. It was observed that after the first 144 hours short-term effects for coatings and sensors to be settled down, started from the 144 to 3598 hours, the center wavelength of embedded FBG sensors of samples fluctuated near zero, except for Sample #S1, which increased about 20 picometers. However, in practical, soft coating was vulnerable to external physical interferences such as impact force, abrasion, and metal cutting. To simulate the corrosion progress after 3598 hours, a cutting damage was intentionally made to the soft coating near sensor location. The visual inspection results were shown in Figure 38.

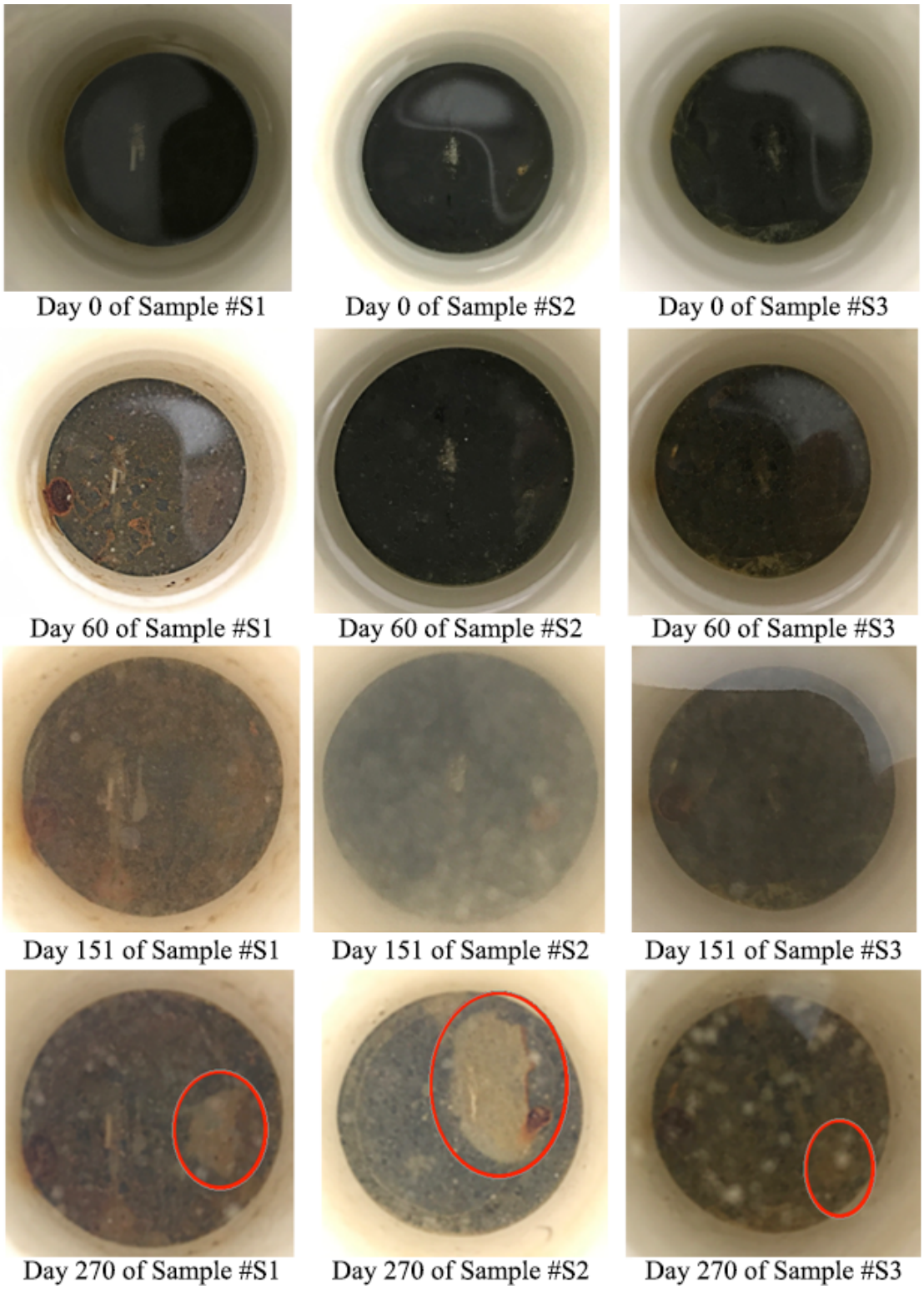

Figure 38. Visual Inspection of Sample #S1, #S2, and #S3.

3.4.2. Discussion

It was observed from visual inspection that Sample #S1 had corrosion initiation before the cutting damage was made. This contributed to the 20 picometer increase in FBG sensor's Bragg wavelength change of Sample #S1 started from about 1270 hours (53 days), as shown in Figure 39. This may due to PVC pipe was attached using a different type of epoxy before the soft coating was fully cured, causing the soft coating delaminated from the substrate. The corrosion assessment system had successfully caught the corrosion initiation and progress.

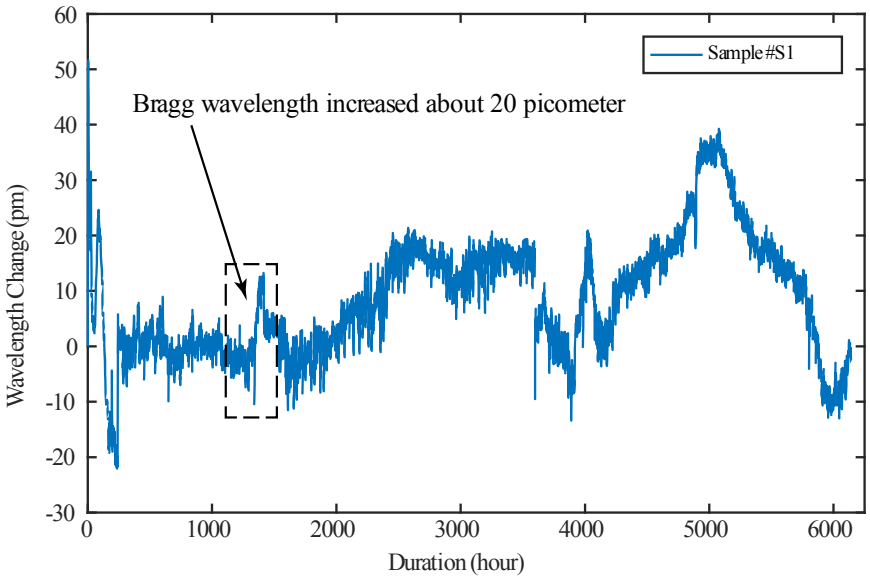

Figure 39. Bragg wavelength change of Sample #S1.

By taking a closer look at the Bragg wavelength change curve of the three sensors together as seen in Figure 40, it was found that when cutting damages were intentionally made to the soft coatings, the Bragg wavelength drop dramatically, showing a similar phenomenon to HVOF thermal sprayed Al-Bronze coating's crack initiation and crack propagation discussed in Section 3.2.2. After the initial Bragg wavelength drop, it was followed by a rapid increase similar to corrosion initiation pattern. This rapid increase suggested that once the soft coating had been damaged, the bare steel had exposed to the corrosive 3.5wt% NaCl solution, and corrosion started to attack the substrate.

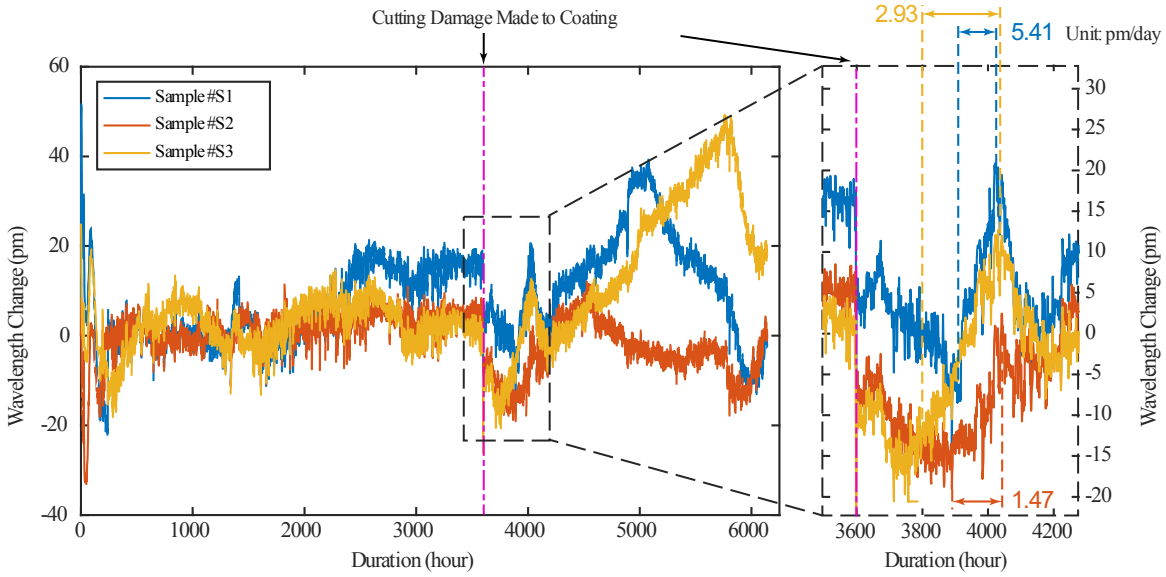

Figure 40. Bragg wavelength of embedded FBG sensors with soft coating with partial enlargement.

In Figure 37 and Figure 40, it was observed that the Bragg wavelength increases were followed by drops, and each of these drops suggested an internal crack or delamination of the soft coating. From the visual inspection result of day 270, it can be clearly identified that large portion of soft coating had delaminated from the substrate, and the samples were severely corroded. Also, the corrosion rate after the crack was made were listed in the Table 7.

Table 7. Corrosion rate after the crack was manually made to soft coating samples.

Sample Number	Sample #S1	Sample #S2	Sample #S3	Average Corrosion Rate
Corrosion Rate (mil/year)	0.2377	0.1287	0.0645	0.1437

The testing results confirmed that proposed corrosion assessment system could be used as an effective way of real-time monitoring corrosion rate on-site. That it successfully detected the coating crack or delamination suggested that the proposed system can be used as a real-time coating condition monitoring tool.

3.5. Corrosion Performance Evaluation of HVOF Thermal Sprayed Al-Bronze Coating on Pipe Samples

To see if the shape of the test samples would contribute the corrosion status monitoring, the corrosion performance with HVOF thermal sprayed Al-Bronze coating was also assessed for pipe samples using the embedded FBG sensors inside the coating through laboratory accelerated corrosion tests. Two A36 structural steel pipe samples were tested in order to evaluate the performance of proposed corrosion monitoring system on pipe shape samples.

3.5.1. Experimental Setup

The pipes had a length of 4 inches, outer diameter of 2.5 inches, and thickness of 0.2 inch. After the FBG sensors were successfully embedded in pipes using the same packaging technique as before, the Al-Bronze coating was applied using HVOF thermal spraying technique on a rotating machine. The coating process and final product were shown in Figure 41. Two samples were noted as Sample #P1 and #P2, respectively.

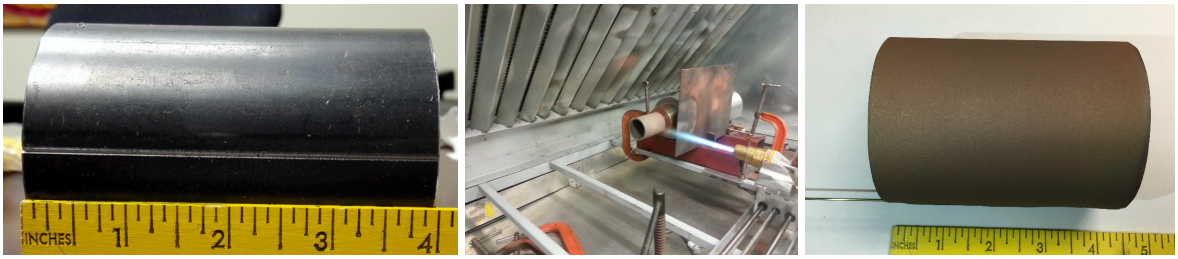

Figure 41. Pipe sample preparation and coating process.

To create the corrosive environment for pipe samples, PVC pipes with larger diameters than coated steel pipes were first attached to a plastic plate foundation using epoxy, and then the coated steel pipes were placed inside it, also fixing with epoxy. 3.5wt% NaCl solution was filled in between, as shown in Figure 42. The experiment had run for 15 days.

Figure 42. Corrosion testing setup for HVOF thermal sprayed Al-Bronze coated pipe samples.

The Bragg wavelength change collected from embedded FBG sensors after temperature compensation were shown in Figure 43. Data collecting rate is 10Hz.

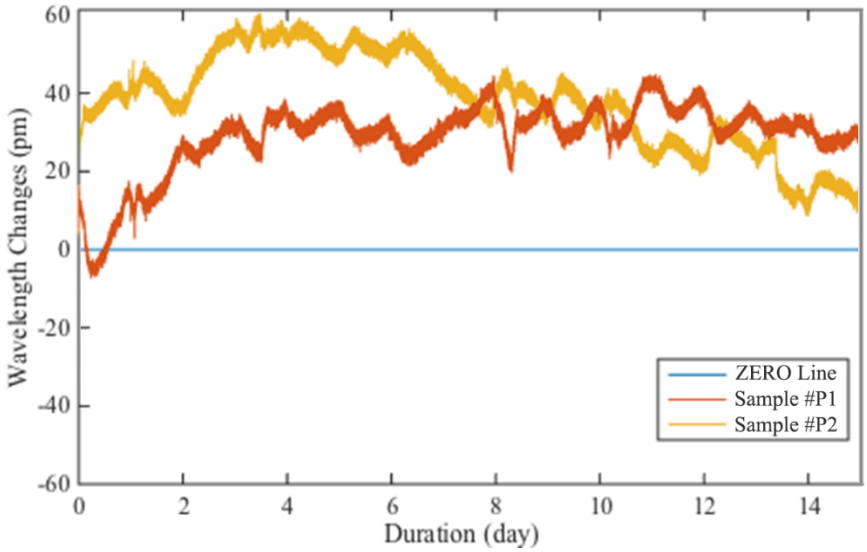

Figure 43. Bragg wavelength change vs time of Sample #P1 and #P2.

3.5.2. Discussion

By measuring the slop of the linear part of the Al-Bronze coated pipe samples, the corrosion rate of the two tested samples can be calculated with Equation (16). The corrosion rate of two samples were shown in Table 8.

The average corrosion rate of the two tested pipe samples was 0.5961 mil/year, which was very close to the Tafel test result. The test results indicated that the pipe samples showed

same results as plates and the developed system can be successfully applied to pipelines in future. The calculation results suggested that the proposed system could be used as an effective way of real-time corrosion rate assessment tool on-site.

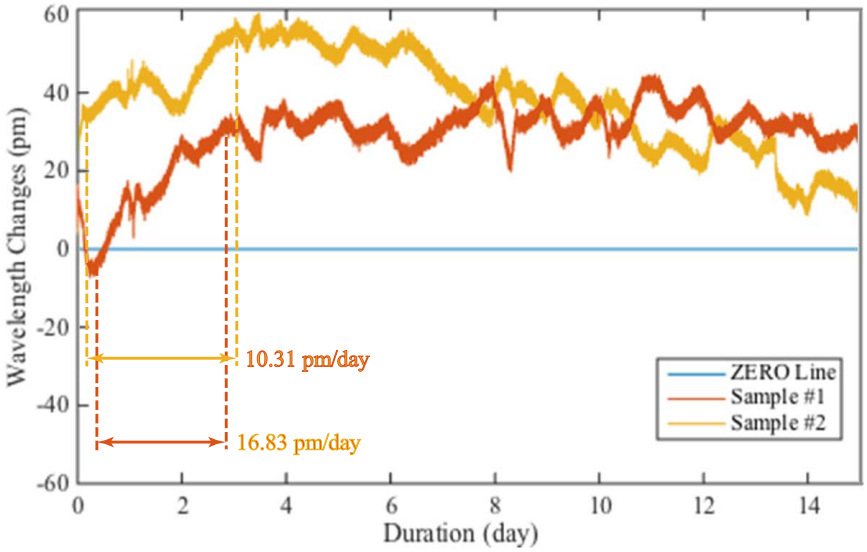

Figure 44. Bragg wavelength change curve of Sample #P1 and #P2 with linear part measured.

Table 8. Corrosion rate of tested HVOF thermal sprayed Al-Bronze coated pipe samples.

Sample Number	Sample #P1	Sample #P2	Samples Average
Corrosion Rate (mil/year)	0.4529	0.7393	0.5961

3.6. Comparison Between Electrochemical Methods and the FBG Sensors

Table 9 compares the corrosion rate testing results of various coatings using the traditional electrochemical method and the embedded FBG sensors. For HVOF thermal sprayed Al-Bronze coatings, the measured corrosion rate from electrochemical method is 0.5054 mil/year and the average corrosion rate detected from the embedded FBG sensors is 0.5366 mil/year, with a difference of 6.2% in between. For wire arc Al-Zn coating, the measured corrosion rate from electrochemical method is 0.0860 mil/year and the average corrosion rate measured from the

embedded FBG sensors is 0.0859 mil/year, with a difference less than 1.0%. The comparison validated that the embedded FBG sensors can detect the corrosion rate accurately.

When comparing the shapes of the samples by using the HVOF thermal sprayed Al-Bronze coating, it can be seen that for steel plate substrate, the average corrosion rate detected from the embedded FBG sensors is 0.5366 mil/year and that for steel pipes is 0.5961 mil/year, with a difference of around 10%. Thus, the non-flat surface of the pipeline may introduce about 10% measurement variance in estimating the corrosion rate, which is still within the allowable range of detecting corrosion. In addition, Table 2 also indicated that the FBG sensors can not only detect the corrosion rate of the coatings, but also monitor the coating corrosion progressing and detect corrosion induced cracks in coatings and substrates if any.

It also can be noted from Table 2 that for metallic coatings, HVOF thermal sprayed Al-Bronze coatings improved the corrosion resistance for more than 3 times when compared to bare steel. The wire arc Al-Zn coatings has an improved corrosion resistance of more than 10 times when compared to HVOF thermal sprayed Al-Bronze coatings and more than 20 times when compared to bare steel. The wire arc Al-Zn coatings can be a very promising corrosion mitigation metallic coating for practical application on steel pipelines.

Table 9. Comparison of corrosion rate testing result between electrochemical approach and FBG sensor approach.

Substrate	Coatings	Electrochemical Method	FBG Sensors
Steel Plate Samples	Bare steel (Sample B)	Corrosion rate tested: 1.5458 mil/year	*
	HVOF thermal sprayed Al-Bronze coating (Sample #1 ~ #4)	Corrosion rate tested: 0.5054 mil/year	Corrosion rate tested: 0.5366 mil/year ** Corrosion progress monitored; Crack initiation detected.
	Wire arc Al-Zn coating (Sample A#1 ~ A#3)	Corrosion rate tested: 0.0860 mil/year	Corrosion rate tested: 0.0859 mil/year ** Corrosion progress monitored; Crack initiation detected.
	Soft coating (Sample S#1 ~ S#3)	*	Crack initiation detected. Corrosion rate after the crack tested: 0.1437 mil/year **.
Steel Pipe Samples	HVOF thermal sprayed Al-Bronze coating (Sample P#1 ~ P#2)	*	0.5961 mil/year**; Corrosion progress monitored Crack initiation detected.

Note: * - not tested; ** - all sample average.

3.7. Summary

In this chapter, the developed corrosion assessment system based on FBG sensors were validated through laboratory experiments for various coatings including hard and soft coatings by comparing with the traditional electrochemical approach. From the laboratory experimental results, it can be seen that 1) the slope of the Bragg wavelength changes monitored from FBG sensors can be directly related to the corrosion rate, 2) the coating failure/ cracks can be detected by a sudden drop in the monitored Bragg wavelength changes, 3) the turning points of the measured Bragg wavelength curve from the embedded FBG sensors indicates different phases of

corrosion progress and the gradual Bragg wavelength changes of the FBG sensor can qualitatively measure the growth of corrosion, 4) the comparison of the corrosion rate of HVOF thermal sprayed Al-Bronze and wire arc Al-Zn coatings between the electrochemical method and the developed corrosion assessment system indicated a difference less than 6%, which validated the effectiveness of the developed system for corrosion detection, and 5) the shape of the substrate does introduce some measurement variance within 10% when compared the steel plate substrate with the pipe substrate. To sum up, the laboratory test results showed that the proposed corrosion assessment system based on FBG sensors is very promising for assessing the coating condition and corrosion state for coated pipes.

4. TWO DIMENSIONAL CORROSION LOCATION IDENTIFICATION

In Chapters 2 and 3, the corrosion status of the steel coatings is successfully related to the center wavelength changes of the embedded FBGs inside the coating followed by experimental validations on various coatings. However, since the FBG sensors are point sensors, the corrosion status of the steel coatings can only be assessed if the sensors were installed exactly at the corrosion locations, which is an unknown location in practical applications. Thus, if the corrosion does not occur exactly at the locations of the embedded sensors, or near the sensors, the effectiveness of the corrosion assessment system is questionable. To solve this challenge, this chapter develops a two dimensional (2D) sensor network with a limited number of sensors along the way of the pipeline that would possibly identify the locations of the corrosion on the coated pipelines. The theoretic algorithm followed by the parametric study through numerical analysis on the developed 2D corrosion location identification system has been investigated systematically in this chapter.

4.1. Plate Theory for 2D Corrosion Localization

When corrosion does not directly occur beneath the embedded point FBG sensor, multiple sensors can be embedded and form a sensor network to locate the corrosion and conduct the following risk management. However, with a sensor network which will be different from the one dimensional problem as discussed in Chapters 2 and 3, the relationship between the sensed strains on the point FBG sensors and corrosion would be a two dimensional (2D) problem. Assume that the two assumptions in Section 2.4 still apply here, the corrosion induced strains on the FBG sensors can be analyzed using a simply supported plate for a 2D problem as shown in Figure 44.

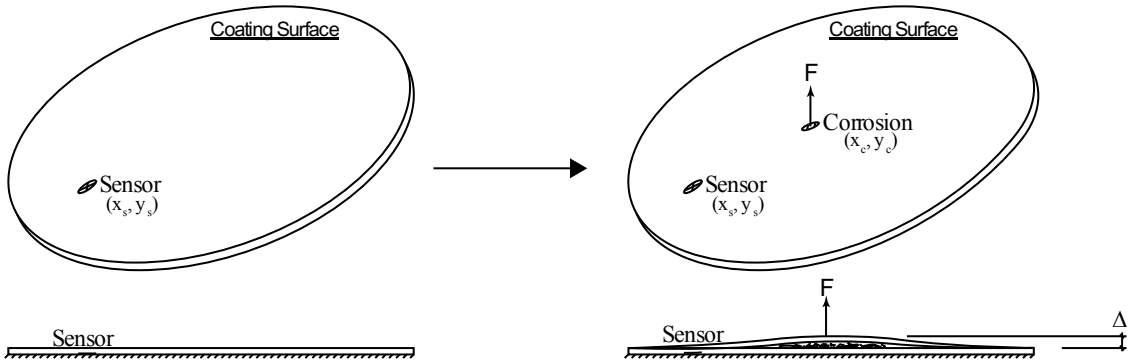

Figure 45. Corrosion plate theory demonstration.

Similar to the simply supported beam theory, the simply supported plate theory also treats the corrosion as a concentrated force applied at a single point on the plate as shown in Figure 44 (right). The corrosion induced displacement Δ has its maximum value at the point of corrosion, and gradually decrease along the way to the lifting edge of coating surface to zero.

Assuming a square plate, and let the radius of the plate to be *r*, in order to get the strain value at sensor location (x_c, y_c), a differential equation should be solved as below [109, 110]:

$$D\left(\frac{\partial^4 w}{\partial x^4} + 2\frac{\partial^4 w}{\partial x^2 y^2} + \frac{\partial^4 w}{\partial y^4}\right) = F(x, y), \qquad \text{where } D = \frac{Eh^3}{12(1-\rho^2)} \tag{17}$$

With the given boundary condition and the known material property (Young's modulus *E*, Poisson's ratio ρ, and coating thickness *h*) of the coating, the strains of any given locations on coating surface under the applied force *F* could be solved. As the actual boundary condition and the external force *F* are not explicitly known, and the strain has only one exact solution, the strain value could be implicitly as in Equation (18):

$$\varepsilon_s = f(x_c, y_c, r, F, E, \rho, h, x_s, y_s) \tag{18}$$

The function *f* took inputs of physical properties of the entire system, the corrosion location and severity, and output the strains of an embedded sensor, so the function *f* represents the transfer function. In Equation (18), the material property, the boundary condition, and the

sensor embedment location stay unaltered when the system is designed. The coating's Young's modulus E, Poisson's ratio ρ, and thickness h, are constants as well as the sensor embedment location (x_s, y_s). Thus, in Equation (18), only x_c, y_c, and F are unknown, which are the corrosion's location and severity. Thus, Equation (18) can be rewritten as:

$$\varepsilon_s = f(x_c, y_c, F) \tag{19}$$

From Equation (19), it could be seen that the strains on embedded sensors were only related to the corrosion location and corrosion severity. Therefore, for this 2D problem, if only one sensor embedded providing one strain measurement, there would be three unknowns in one equation. Since the number of unknown parameters had exceeded the number of equations, the equation could not be solved for both the corrosion location and the corrosion severity. As a result, if only one sensor embedded in the system, it could detect the corrosion initiation, but not the corrosion location and corrosion severity simultaneously.

It could also be seen from Equation (19) that in order to get both the corrosion location and severity information, a sensor network composed of multiple sensors was required. With multiple sensor covering the same sensing area, for a single corrosion initiated within this area, different sensors would have a different strain reading. Thus, the number of equations had increased but the number of unknown parameters remain not changed. For instance, if there were n sensors embedded in the area to assess the potential one single corrosion, the total number of strain reading would be n, and so was the total number of equations, as shown below:

$$\begin{aligned} \varepsilon_{s1} &= f_1(x_s, y_s, F) \\ \varepsilon_{s2} &= f_2(x_s, y_s, F) \\ &\vdots \\ \varepsilon_{sn} &= f_n(x_s, y_s, F) \end{aligned} \tag{20}$$

There was a total of three unknowns to be solved in Equation (20), therefore, in case of $n \geq 3$, there were enough equations to solve corrosion location and severity information for a single corrosion. Thus, a minimum of three sensors were needed to locate and characterize the corrosion in coatings. Figure 46 shows a potential sensor network consisting of three sensors and a single corrosion.

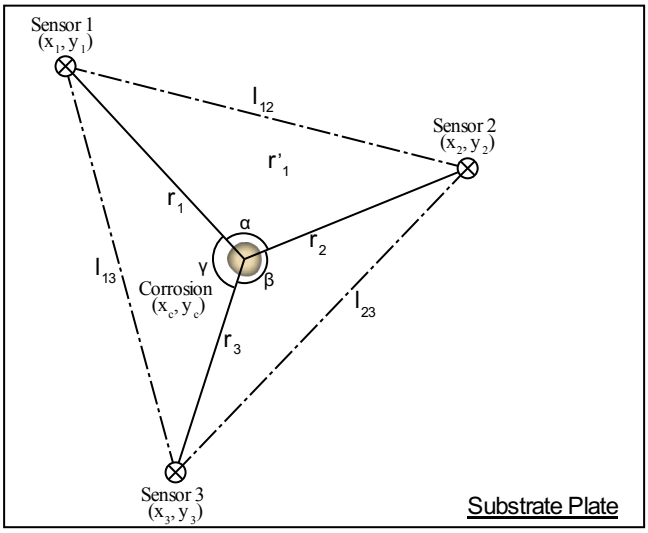

Figure 46. A three-sensor network demonstration.

However, without knowing the actual transfer function *f*, the equations would remain unsolved. In next section, the transfer function *f* on the corrosion localization algorithm would be derived through numerical analysis.

4.2. Transfer Function from Numerical Analysis

To derive the transfer function, *f*, between corrosion location/severity and the measured strains from the embedded sensors, numerical analysis using the finite element model (FEM) analysis was conducted since an analytical solution for the above mentioned differential equations would be very complicated and time-consuming [111-113].

The numerical analysis can be performed using fixed the sensor location at the center of the simply supported plate and altering the corrosion locations and severity. As seen in Figure

47, if the sensor location was fixed at the center (0,0), with multiple corrosion cases at (0,1), (1,0), (1,1), etc., the transfer function from corrosion location/severity to the measured strains from the embedded sensors could be obtained. However, this approach would result in a large number of cases, depending on the precision requirement. For instance, in Figure 47, if the precision is required to be 1, and the corrosion severity between two discrete corrosion locations had to be interpolated linearly or using curve fitting techniques. Thus, if an accurate location detection was desired, it may require thousands of cases to meet the precision.

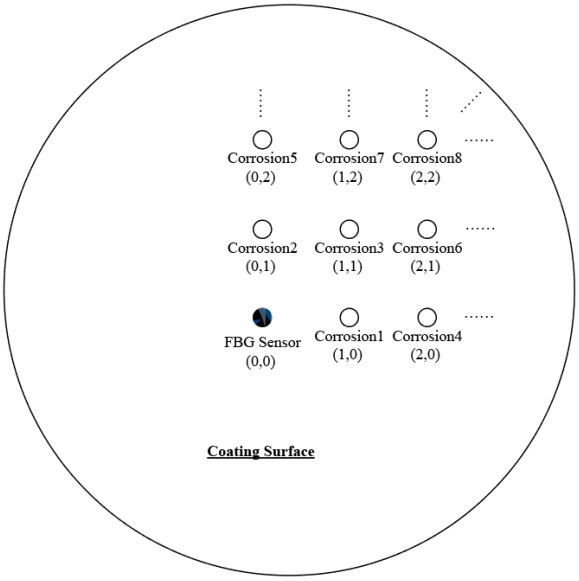

Figure 47. Simulation model with sensor at fixed location.

Instead of creating multiple models that has the sensor in the middle and varies the corrosion location to getting the strains to corrosion location/severity relation, another approach is to fix the corrosion location as shown in Figure 48 and create a strain distribution, which can be inversely used to get the corrosion location/intensity. Compared with the altering corrosion location, this approach is much time efficient, which was applied in this study.

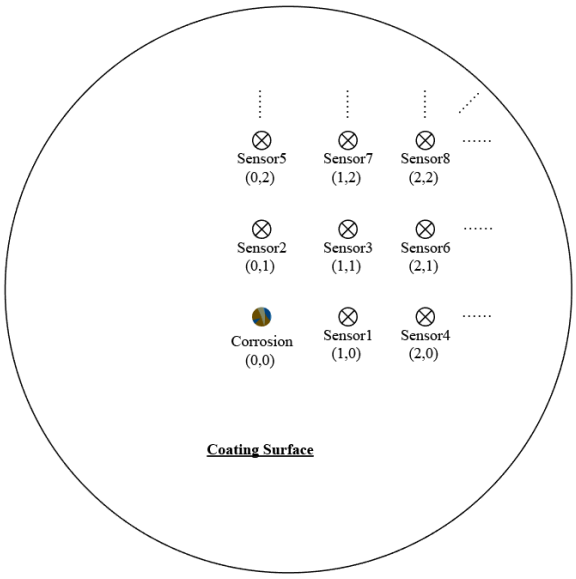

Figure 48. Simulation model with corrosion at fixed location.

Based on Figure 48, a FEM model was set up in ANSYS as seen in Figure 49. Since it was assumed that the coating was not de-attached from the steel substrate, the out ring of the simply supported plate was fixed all degree of freedom (DOF) as boundary condition. The corrosion was simulated as a force applied at the center of the plate, with an amplitude of 1 N. The x-axis and y-axis were within the plate plane, and the z-axis was perpendicular to the plate plane with the positive value represent a direction point up side in Figure 49. Detailed configuration about the FEM model was shown in Table 10.

Table 10. Configuration of the circle plate FEM model.

Unit of length	mm
Unit of force	N
Radius of the plate	10 mm (0.394 in.)
Thickness of the plate	2 mm (0.079 in.)
Young's modulus of the plate	5.157 MPa (748 psi)
Poisson's ratio of the plate	0.29
Element Type	Shell 181

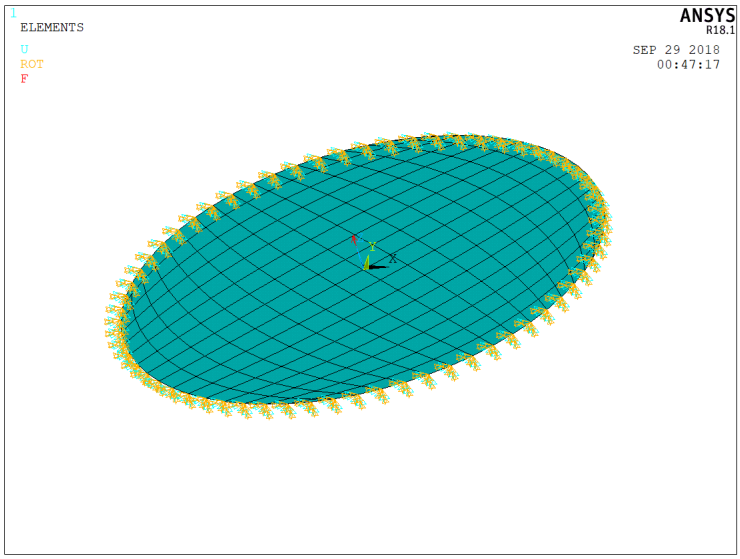

Figure 49. FEM model of the proposed plate theory using ANSYS.

4.2.1. Numerical Analysis Results

Figure 50 (a ~ d) show the simulation results. Since the corrosion initiated at the center of the circle plate, the results showed the maximum strain was at the center area of the plate. In X-direction strain distribution, it was observed that the gradient of strain along the X-axis was higher than gradient in Y-axis. The distribution of the strain intensity (showing the all directional strain level) and Z-direction displacement were similar as seen in Figure 50(c, d).

Figures 50(a, b) also show that the distributions of X-direction strain and Y-direction strain had a 90 degree difference. Since the FBG sensors can only measure strains in its longitudinal direction, the difference between the strain distribution of X-direction and Y-direction suggested that the installation direction of FBG sensors should be carefully designed and recorded. These strain maps in Figures 50(a, b) were later used to derive the transfer function.

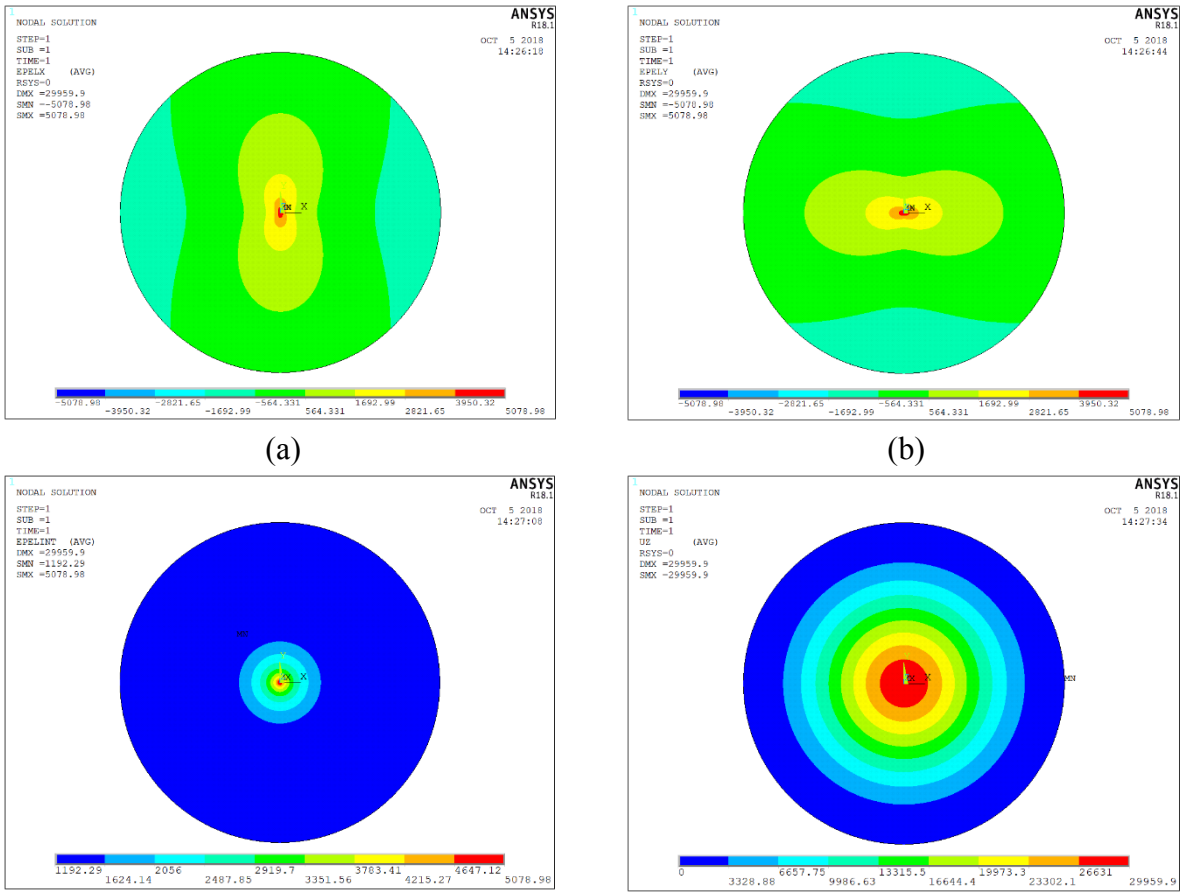

Figure 50. Simulation results of the proposed plate model (a) X-direction strain, (b) Y-direction strain, (c) strain intensity, and (d) Z-direction displacement.

In practice, the coating might not form an exact circle under corrosion attacks. To search for the possible differences in strain distribution between shapes, defects were also simulated using numerical analysis as seen in Figure 51. There were in total of 6 partial circles being substrate from the original plate model, and their radius were 0.05mm, 0.08mm, 0.06mm, 0.12mm, 0.12mm, and 0.06mm, respectively. Other modeling data of the irregular-edge plate model was the same as the original plate model shown in Table 10. In Figure 52, it can be seen that a non-uniform distributed coating bonding strength or defects may result in irregular edge for the circle plate which were simulated in this study.

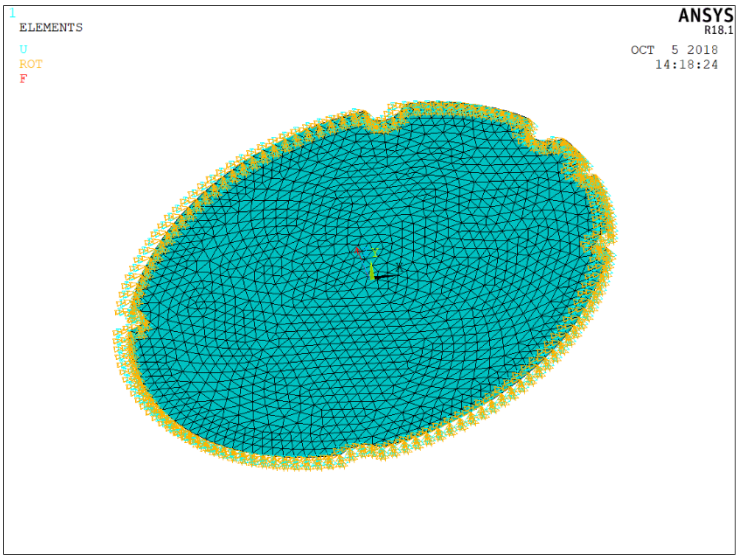

Figure 51. Simulation model of circle shape plate with irregulated edges for defects.

The simulation results were shown in Figure 52. From the X-direction strain and Y-direction strain results, it was observed that the distributions of strains in center area of irregular edge circle plate were similar to circle shape plate (in Figure 50), and the only differences were at edge. Other than that, because the boundary condition, their strain intensity had a 10% difference.

The similar strain distributions in X-direction and Y-direction suggested that although the coating bonding strength varies, by using the results from the circle shape plate, the proposed corrosion identification system may still locate corrosion successfully. The corrosion severity, however, may not be over-estimated or under-estimated for different defect types.

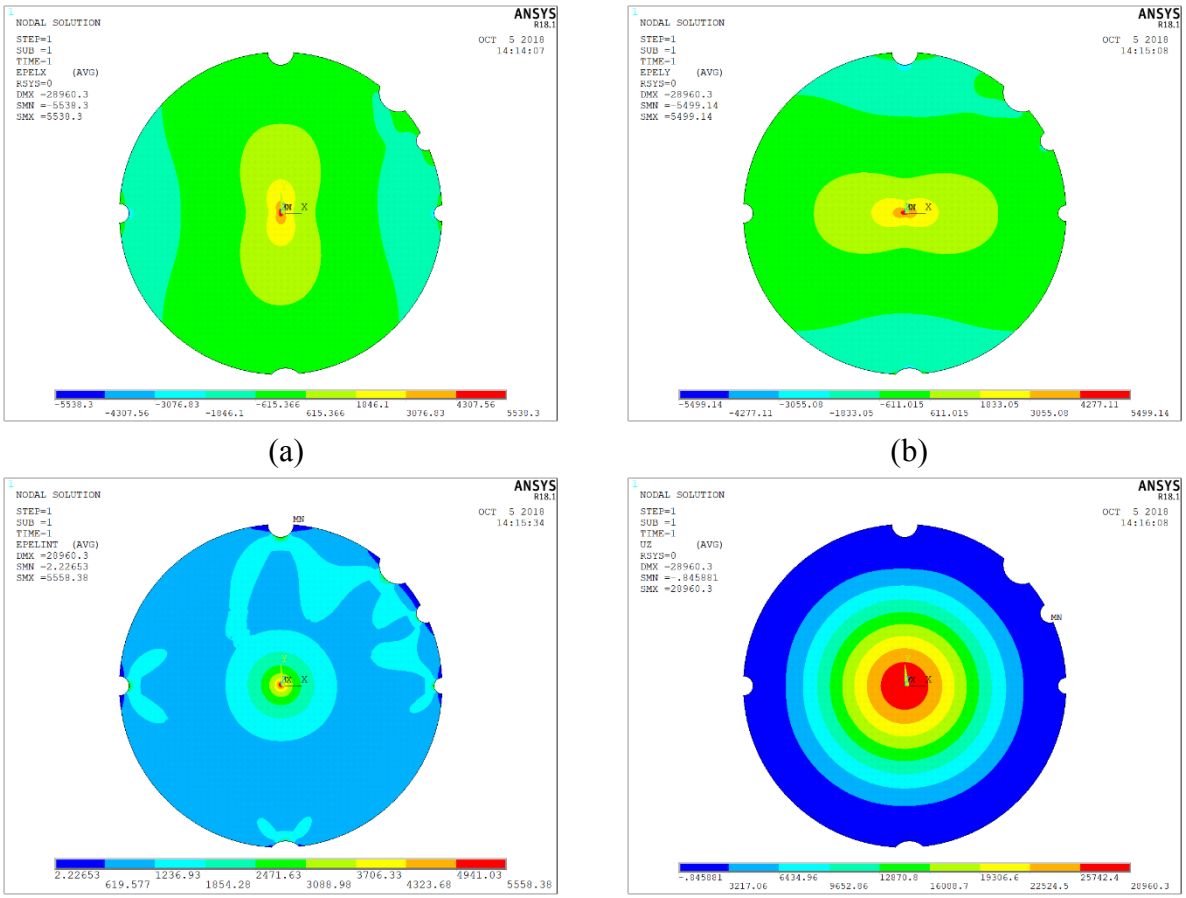

Figure 52. Simulation result of circle plate with irregular edges model (a) X-direction strain, (b) Y-direction strain, (c) strain intensity, (d) Z-direction displacement.

In addition to the circle shape, rectangular and ellipse shape coating plates were also simulated, as shown in Figure 53 and Figure 55, and their simulation results were shown in Figure 54 and Figure 56. The dimension configuration of these two models were shown in Table 11, and other configurations were kept the same as in Table 10.

Table 11. Configuration of the rectangular and ellipse plate models.

Side length of rectangular plate model	10 mm (0.394 in.)
Semi-major axis length of the ellipse plate model	10 mm (0.394 in.)
Semi-minor axis length of the ellipse plate model	8 mm (0.315 in.)

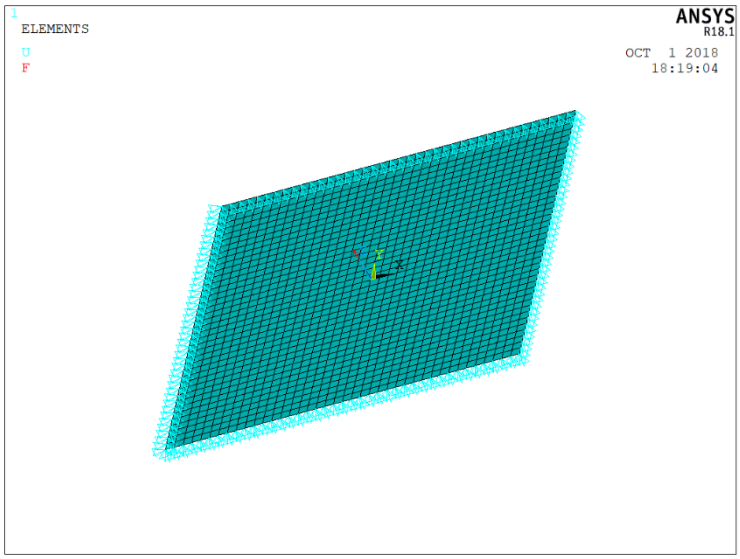

Figure 53. Simulation model of rectangular shape plate.

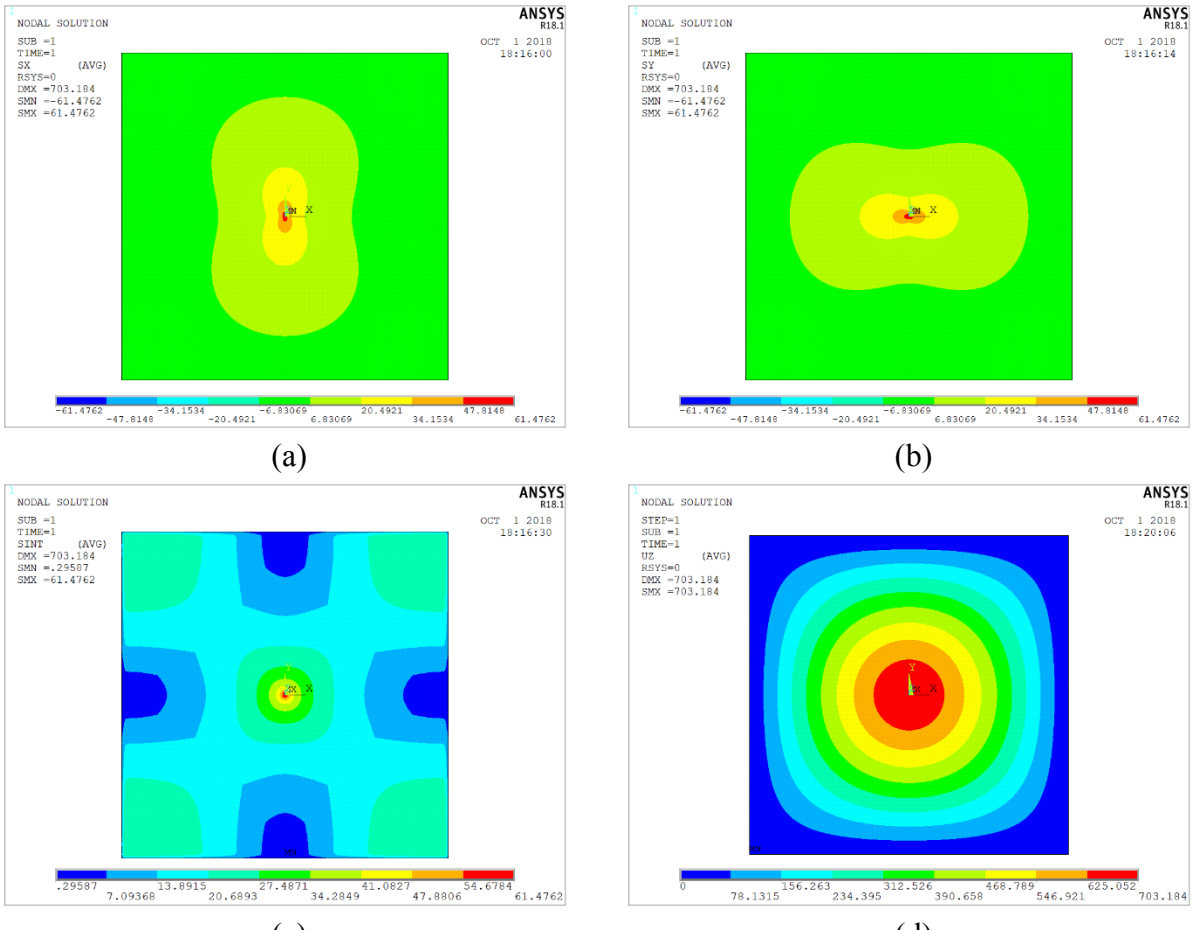

Figure 54. Simulation result of rectangular plate model (a) X-direction strain, (b) Y-direction strain, (c) strain intensity, (d) Z-direction displacement.

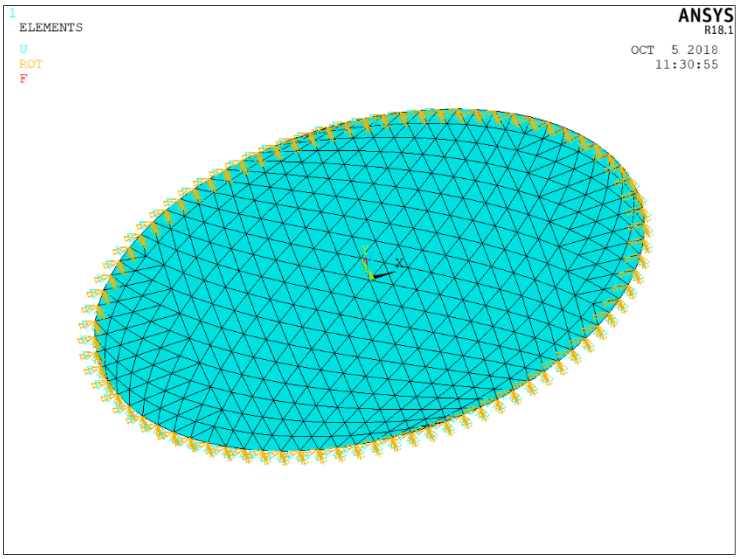

Figure 55. Simulation model of ellipse shape plate.

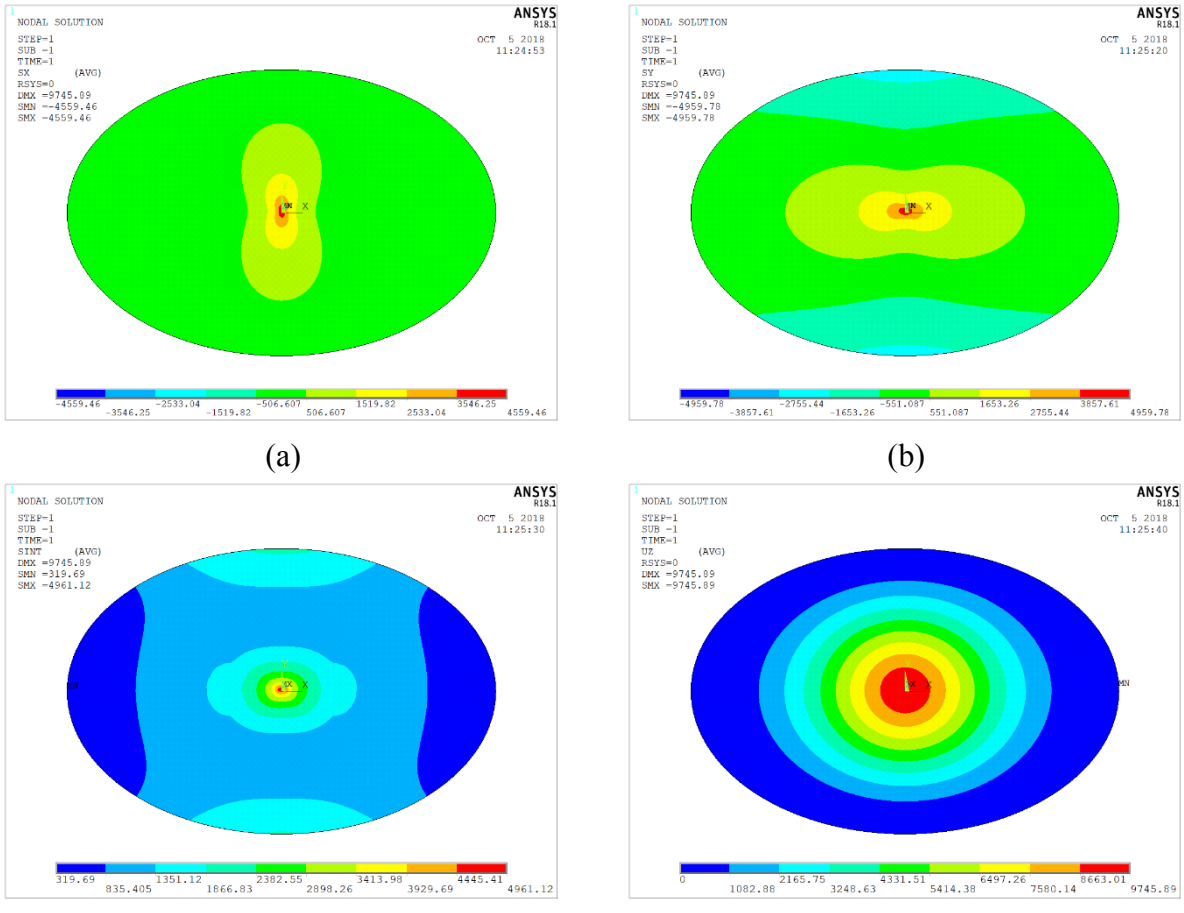

Figure 56. Simulation result of ellipse plate model (a) X-direction strain, (b) Y-direction strain, (c) strain intensity, (d) Z-direction displacement.

Similar as the circle shape plate simulation results, if the corrosion initiated in the center point of the plate, the rectangular and ellipse shape plate would have an x-direction strain and a y-direction strain with 90 degree difference. The distributions of strain were similar to the circle shape plate.

4.2.2. Corrosion Localization Algorithm

The four simulated cases above covered different boundary condition of proposed plate theory. In all cases, the maximum strain value appeared at the center of the plate, which was also the axis for both X-direction strain and Y-direction strain, and the distributions were symmetric to X-axis and Y-axis. These symmetric distributions suggested that the FBG sensor installation should avoid symmetric locations in order to achieve corrosion location detection. Even though the strain value in the four cases were different, the strain distribution could be used for corrosion location detection. Now, let's solve the transfer function equations (Equation (20)) to locate the corrosion using the method of exhaustion. As shown in Figure 57, if the sensing area was divided in several subareas, and using Euclidean space to describe these subareas, for every sensor and every possible corrosion initiated, their location could be demonstrated using the subarea that contains them. In the specific example in Figure 57, Sensor 1, Sensor 2, and Sensor 3's locations could be noted as (3,4), (4,1), and (6,2), respectively.

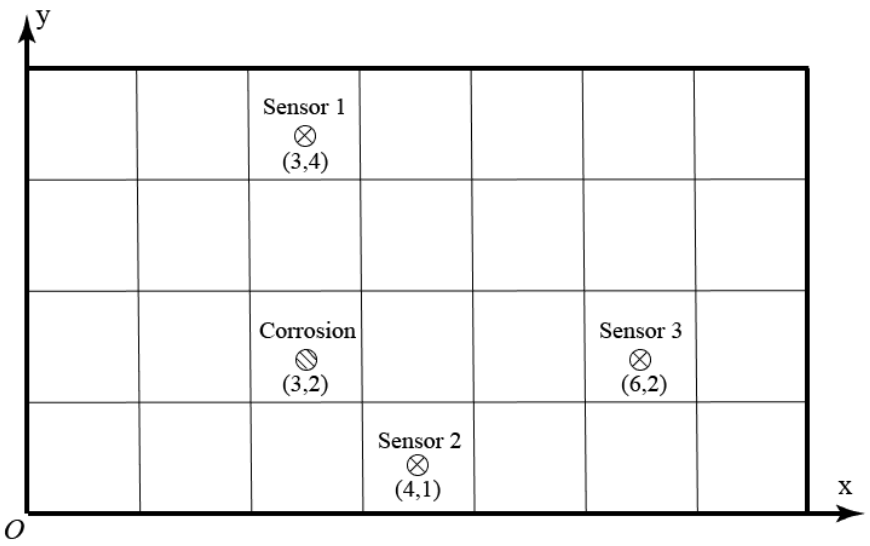

Figure 57. An example for method of exhaustion in corrosion location detection.

Before the corrosion initiated, sensors would have similar readings close to zero. Once the corrosion had initiated, these three sensors would have three different readings because the strains induced by the corrosion at different location varied as mentioned in previous section. Thus, in Figure 57, the strains measured from Sensor 1, 2, and 3 were noted as ε_1, ε_2, and ε_3.

However, due to the fact that there is only one corrosion, ε_1, ε_2, and ε_3 must follow one same transfer function, using the same severity input, with different location inputs. Since the corrosion severity was linear to strain induced by corrosion, Equation (20) can be re-written as:

$$\begin{aligned} \varepsilon_1 &= S \cdot f_c(x_{sc1}, y_{sc1}) \\ \varepsilon_2 &= S \cdot f_c(x_{sc2}, y_{sc2}) \\ \varepsilon_3 &= S \cdot f_c(x_{sc3}, y_{sc3}) \end{aligned} \tag{21}$$

where f_c is the transfer function for corrosion c; x_{sc} and y_{sc} are the relative location for three different sensors in regarding to corrosion c; and S was the linear corrosion severity factor.

Since the sensors' locations were fixed after installation, for any possible corrosion initiated at location (x_c, y_c) with severity factor of 1.0, the strains at all the three sensor locations could be calculated as:

$$\begin{aligned}\widehat{\varepsilon_1} &= 1.0 \cdot f_{(x_c,y_c)}(x_{sc1}', y_{sc1}') \\ \widehat{\varepsilon_2} &= 1.0 \cdot f_{(x_c,y_c)}(x_{sc2}', y_{sc2}') \\ \widehat{\varepsilon_3} &= 1.0 \cdot f_{(x_c,y_c)}(x_{sc3}', y_{sc3}')\end{aligned} \tag{22}$$

As a result, if we could calculate the strains for every possible corrosion location in the area, and then find a match that:

$$\begin{aligned}\widehat{\varepsilon_1}/\widehat{\varepsilon_3} &= \frac{f_{(x_c,y_c)}(x_{sc1}', y_{sc1}')}{f_{(x_c,y_c)}(x_{sc3}', y_{sc3}')} = \frac{S \cdot f_c(x_{sc1}, y_{sc1})}{S \cdot f_c(x_{sc3}, y_{sc3})} = \varepsilon_1/\varepsilon_3 \\ \widehat{\varepsilon_2}/\widehat{\varepsilon_3} &= \frac{f_{(x_c,y_c)}(x_{sc2}', y_{sc2}')}{f_{(x_c,y_c)}(x_{sc3}', y_{sc3}')} = \frac{S \cdot f_c(x_{sc2}, y_{sc2})}{S \cdot f_c(x_{sc3}, y_{sc3})} = \varepsilon_2/\varepsilon_3\end{aligned} \tag{23}$$

then the corrosion location c could be estimated at (x_c, y_c). And the linear corrosion severity factor could be calculated as:

$$S = \varepsilon_1/\widehat{\varepsilon_1} \tag{24}$$

In the example of Figure 57, the corrosion was initiated at (3,2), then the measured strains that sensors were:

$$\varepsilon_1 = S \cdot f_c(0,2)$$

$$\varepsilon_2 = S \cdot f_c(1,-1)$$

$$\varepsilon_3 = S \cdot f_c(3,0)$$

As the computer program try to exhaust all possible corrosion location, it would start at possible corrosion location (1,1), and the calculation would be:

$$\widehat{\varepsilon_1} = 1.0 \cdot f_c(2,3)$$

$$\widehat{\varepsilon_2} = 1.0 \cdot f_c(3,0)$$

$$\widehat{\varepsilon_3} = 1.0 \cdot f_c(5,1)$$

which definitely would not match $\widehat{\varepsilon_1}/\widehat{\varepsilon_2} = \varepsilon_1/\varepsilon_2$ and $\widehat{\varepsilon_2}/\widehat{\varepsilon_3} = \varepsilon_2/\varepsilon_3$. So, the method of exhaustion corrosion location detection algorithm would move on to the next possible corrosion (2,1), and calculated again, as shown in Figure 58.

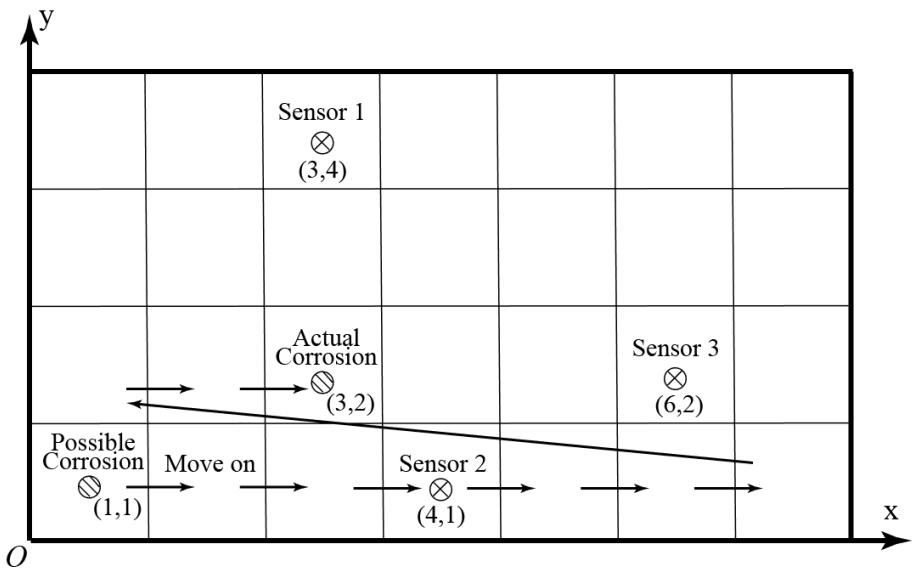

Figure 58. Method of exhaustion in corrosion location detection iteration.

Until it reached the possible corrosion location (3,2), the calculated result would be:

$$\widehat{\varepsilon_1} = 1.0 \cdot f_c(0,2)$$

$$\widehat{\varepsilon_2} = 1.0 \cdot f_c(1,-1)$$

$$\widehat{\varepsilon_3} = 1.0 \cdot f_c(3,0)$$

This result finally matched the actual sensors' reading, because we had:

$$\widehat{\varepsilon_1}/\widehat{\varepsilon_3} = \frac{1.0 \cdot f_c(0,2)}{1.0 \cdot f_c(3,0)} = \frac{f_c(0,2)}{f_c(3,0)} = \frac{S \cdot f_c(0,2)}{S \cdot f_c(3,0)} = \varepsilon_1/\varepsilon_3$$

$$\widehat{\varepsilon_2}/\widehat{\varepsilon_3} = \frac{1.0 \cdot f_c(1,-1)}{1.0 \cdot f_c(3,0)} = \frac{f_c(1,-1)}{f_c(3,0)} = \frac{S \cdot f_c(1,-1)}{S \cdot f_c(3,0)} = \varepsilon_2/\varepsilon_3$$

Thus, the corrosion location had been detected successfully at the current location (3,2).

For higher corrosion location detection precision requirement, the total area could be divided into a greater number of and smaller subareas. In this case, the computing power

requirement might increase dramatically as the number of subareas increases. To solve this possible limitation in computing power, the theoretical strains at sensors' locations for every possible corrosion location could be calculated once and stored. Thus, when the corrosion detection system was running, instead of exhausting the whole area for every single sensor strain reading, to achieve corrosion location detection only requires the comparison between the monitored strain value ratio and stored strain value ratios, which could save huge amount of time.

4.3. Proof-of-concept Experiments and Data Analysis

To validate the corrosion locating algorithm mentioned in last section, laboratory experiments were conducted, and corrosion localization was performed using the developed algorithm.

4.3.1. Experimental Setup and Results

One steel pipe with a layer of epoxy soft coating was served as test sample for the proof-of-concept experiment. The material of sample was A36 structural steel, which was same as previous samples. The pipe was NPS size 6 schedule 40, which had a diameter of 6.625 inches, a thickness of 0.28 inch and a length of 10 inches. Soft coating used in this experiment was epoxy (Duralco 4461), which was same as soft coating used in Section 3.4. Three sensors were embedded before soft coating applied. Sensor location and the pipe sample set up were shown in Figure 59.

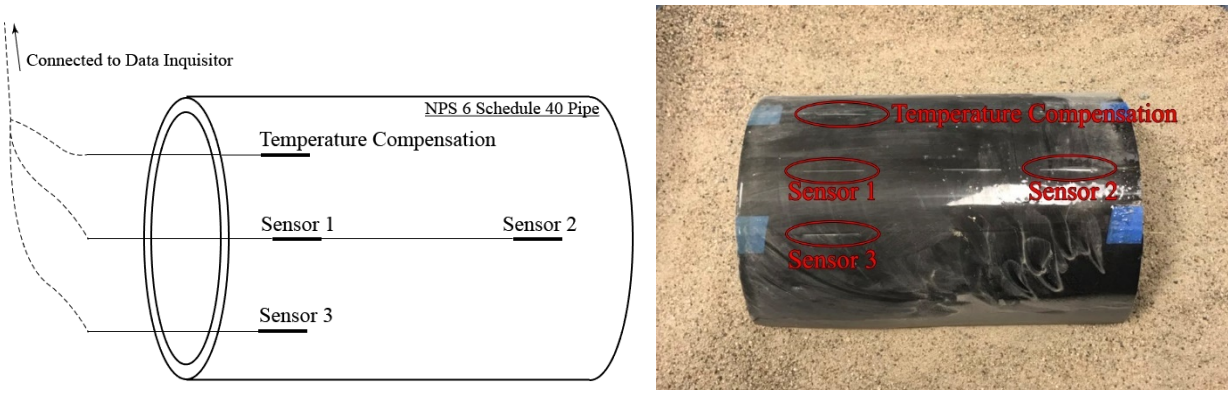

Figure 59. Steel pipe sample preparation for corrosion location detection.

The steel pipe sample was buried in sand after soft coating was fully cured, and 3.5wt% NaCl solution was sprayed on to the sand every other day to maintain a corrosive environment around the steel pipe. The experiment setup was shown in Figure 60.

Figure 60. Experiment set-up for corrosion location detection.

The experiment run for a total of 60 days. In the 31st day, a small crack was made intentionally near Sensor 1 on coating to accelerate the corrosion initiation, since the deterioration rate of soft coating was slow, and the corrosion may not initiate before the damage of soft coating. Crack location was near Sensor 1 as shown in Figure 61.

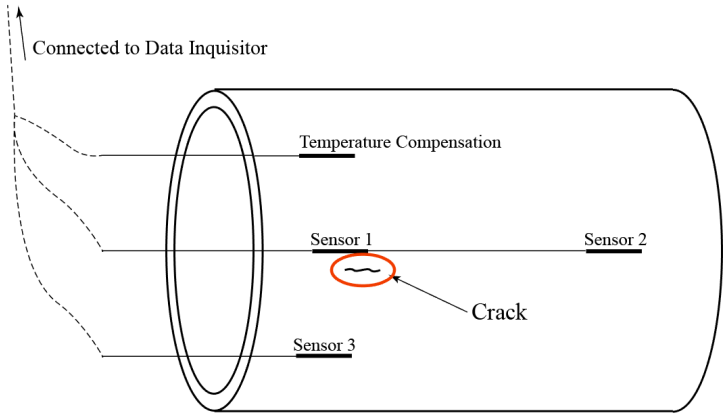

Figure 61. Coating crack location on steel pipe.

4.3.2. Experimental Results

Figure 62 shows the measured Bragg wavelength changed of tested steel pipe sample with soft coating. In Figure 62, the crack making time is marked in graph. It can be seen that the Bragg wavelength increased for a short time before it dramatically dropped for Sensor 1 and Sensor 3 after the crack was made. The Bragg wavelength of Sensor 2 was nearly not changed much (within 5pm) during the entire experiment, which indicate the corrosion was initiate far away from Sensor 2.

Similar to the phenomenon shown in Section 3.4, corrosion at first would increase the Bragg wavelength and dramatically decrease due to coating delamination, which was caused by aggressively expanded corrosion progress.

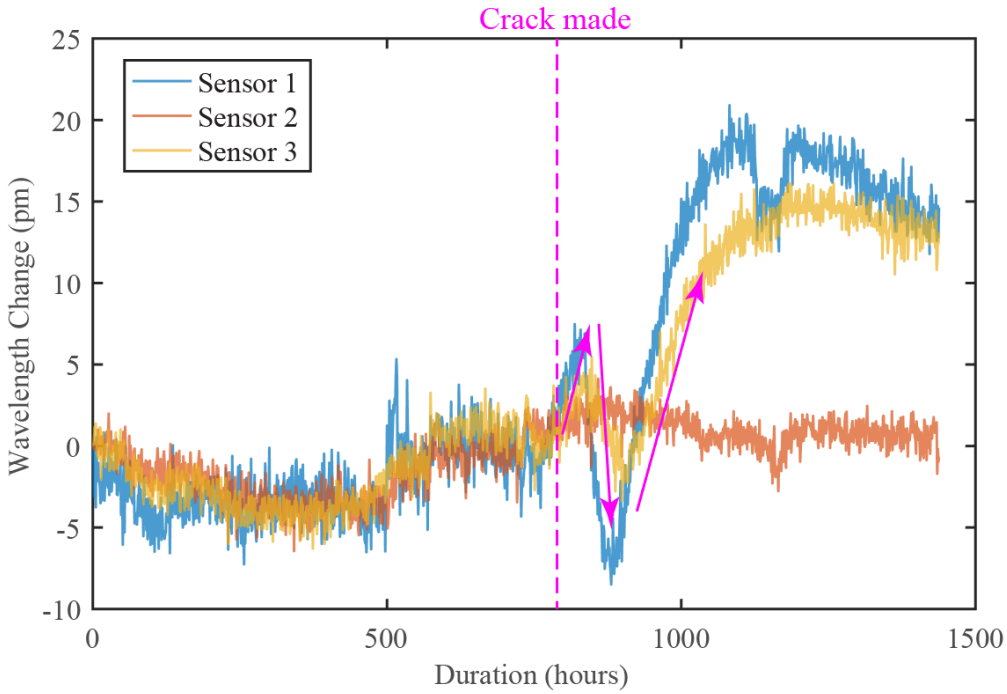

Figure 62. Bragg wavelength change curve of steel pipe sample with crack making time marked

4.3.3. Corrosion Location Identification

The transfer function used in this experiment was simulated using FEM analysis and is shown in Figure 63. The entire sensing area was set as half of the pipe surface, and the area was divided into 10,000 subareas with 100 rows and 100 columns as seen in Figure 64. Every 1 unit stands for 0.1 inch. Sensor 1 location was (15,50), Sensor 2 location was (85,50), and Sensor 3 location was (15,18). The crack made intentionally was at (15,45). All sensors' locations were using the mid-point of the Bragg grating.

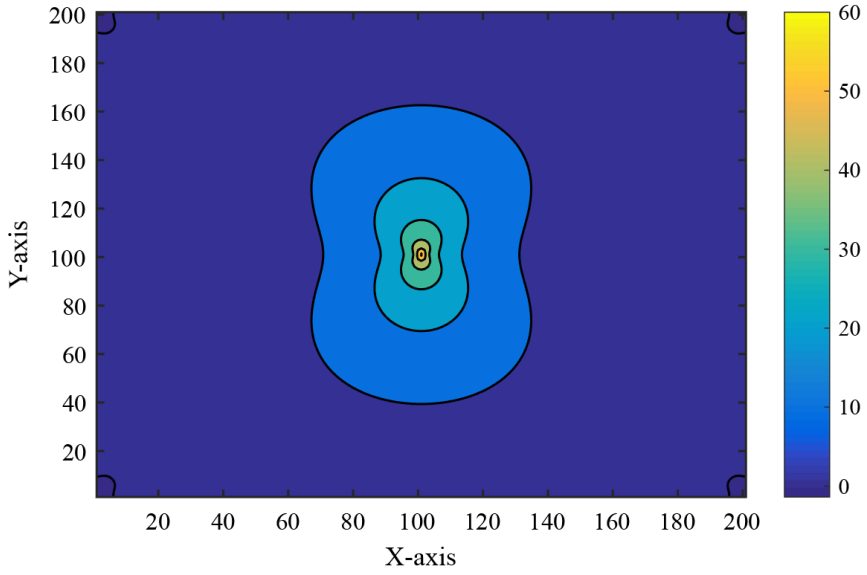

Figure 63. Corrosion induced strain map.

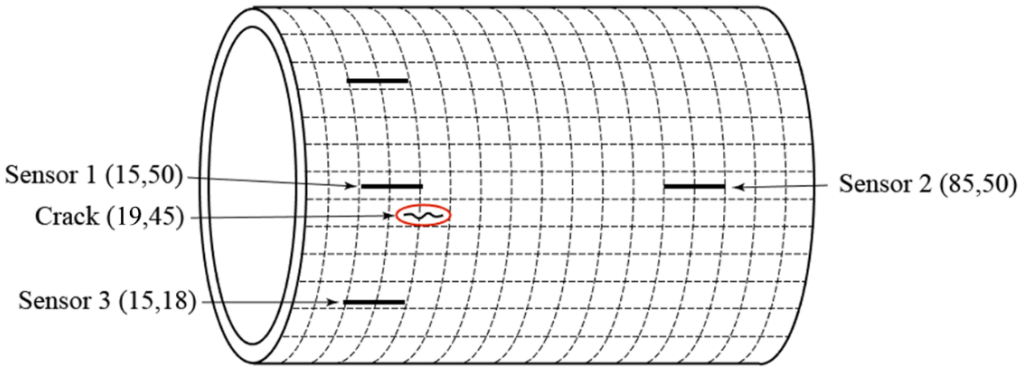

Figure 64. Steel pipe with definition of subareas.

Before the crack was made to the soft coating, since these was no corrosion, the Bragg wavelength changes of all three sensors were close to zero, and the strain ratios ($\varepsilon_1/\varepsilon_3$ and $\varepsilon_2/\varepsilon_3$) were unstable. As a result, the corrosion location detection algorithm cannot match any corrosion location during this period.

After the crack was intentionally made to soft coating, the corrosion started to initiate. However, the corrosion caused a coating crack in a short time before the Bragg wavelength change curve having a stable increase, so the corrosion location detection algorithm was not able

to match any location in the first increase of Bragg wavelength change curve. The main reason is the strain value of Sensor 1 and Sensor 3 were close to zero.

After the Bragg wavelength change curve dropped due to the coating delamination, the corrosion location was successfully detected during the second increase of Bragg wavelength change curve (shown as the highlighted part in Figure 65).

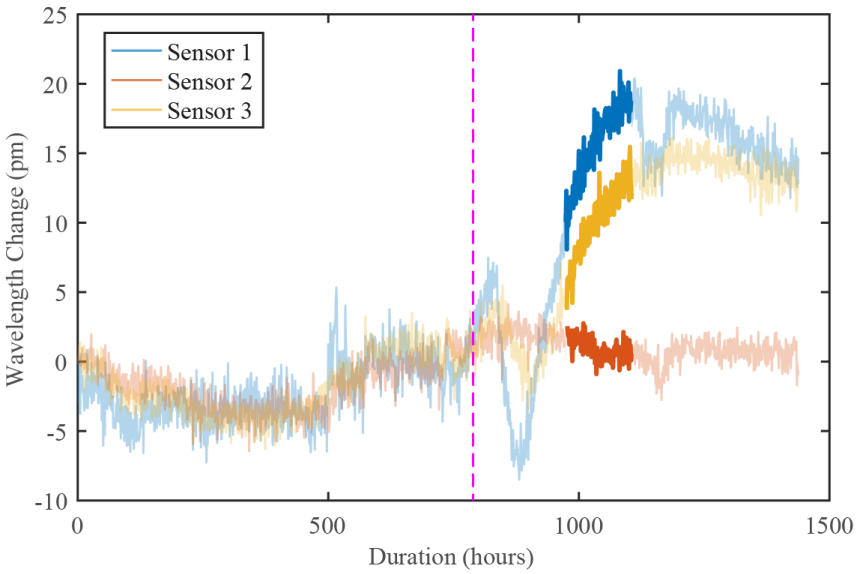

Figure 65. Bragg wavelength change curve of steel pipe sample with successful corrosion location detection

The zoomed in detail of highlighted part of the Bragg wavelength change curve was shown in Figure 66. It was observed that the Sensor 1 and Sensor 3 clearly had larger Bragg wavelength change comparing to the Sensor 2, and the ratio of Sensor 1 to Sensor 3 was stable. The Bragg wavelength change curves were denoised using wavelet package before the corrosion location detection algorithm applied, as shown in Figure 67.

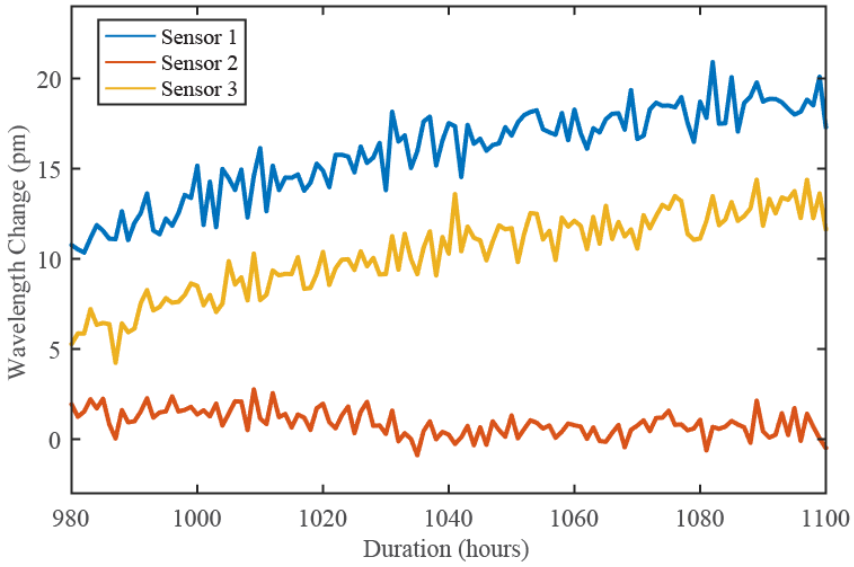

Figure 66. Corrosion location detection inputs.

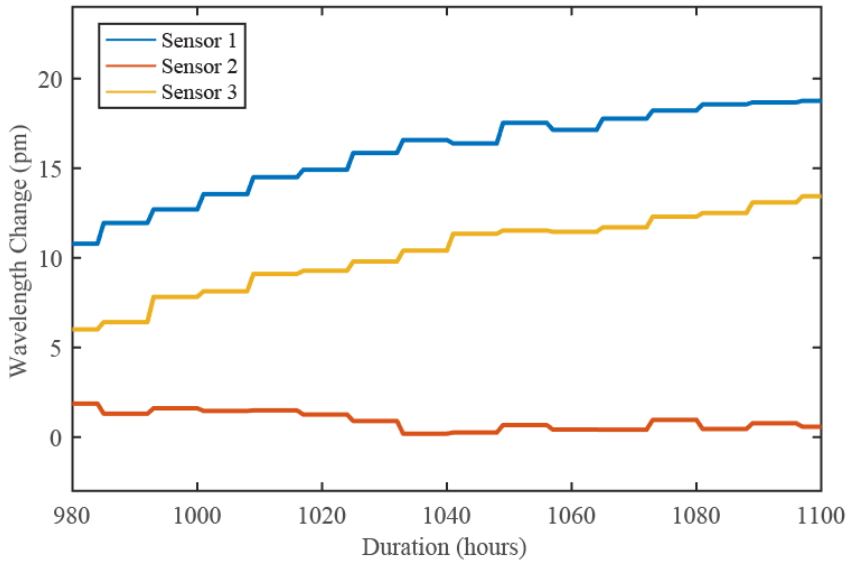

Figure 67. Denoised Bragg wavelength change curve inputs.

The strain inputs were divided into three segments and the average strain ratio value for each segment were served as input in the corrosion detection algorithm, as shown in Figure 68. For the first segment (Segment 1), the algorithm located corrosion at (25,32). For the second and the third segment (Segment 2 and Segment 3), the algorithm located corrosion at (17,42) and (23,47). From the crack location and visual inspection result shown in Figure 69, the actual

corrosion location was at (19,45), which was 1.3 inches away from estimation of Segment 1, 0.4 inch away from estimation of Segment 2, and 0.4 inch away from estimation of Segment 3.

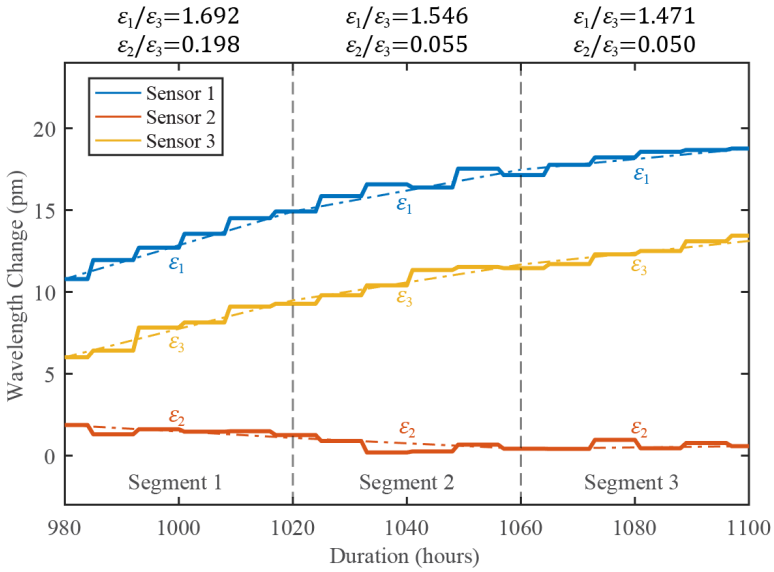

Figure 68. Bragg wavelength change curve segments and the strain ratios.

Figure 69. Visual inspection result for the steel pipe sample at 60th day.

From the corrosion location detection algorithm estimation results, it could be found that the corrosion location detected from Segment 2 and Segment 3 were more accurate comparing to Segment 1. It could be predicted that this algorithm is more accurate when the corrosion was at a stable increase stage.

4.4. Summary

In this chapter, the corrosion location identification using the developed corrosion assessment system was developed. The 2D plate theory can be applied to identify the corrosion location using a sensor network with minimum of three embedded FBG sensors in the coating. The transfer function between the corrosion locations and the severity can be set up using FEM analysis. By using the method of exhaustion, a corrosion locating algorithm was successfully programed. With the transfer function's numerical solution from finite element model, method of exhaustion can be used as algorithm to estimate corrosion locations and severity when Bragg wavelength change curve of sensors were interrogated from embedded FBG sensors. The proof-of-concept experimental results indicated the proposed corrosion assessment system could successfully locate the corrosion positions.

5. SYSTEM PLACEMENT OPTIMIZATION - EXAMPLE CASE STUDY

With the developed real-time corrosion risk assessment system in previous chapters, the corrosion initiation and expansion could be monitored and assessed in a timely manner. However, due to fact that the pipeline is very long (millions of miles in United States [10]), the locations to place the sensing units is very challenging. For an effective corrosion risk assessment system, the sensor placement needs to cover the key locations to avoid large possible oil/gas discharges. Thus, the sensor placement locations can be optimized and guided through the worst case oil/gas discharge analysis. In this chapter, an example case study was used to demonstrate how to use the worst case oil/gas discharge to determine the placement locations of the real-time corrosion assessment system, and how much oil spill could be prevented if the system is in place.

5.1. Worst Case Oil/Gas Discharge Method

To determine the most critical locations for system placement along the pipeline, preliminary analysis can be performed using worst case oil/gas discharge calculation. The locations need to install the real-time corrosion assessment system can be ranked using the worst case oil/gas discharge analysis. Then the placement of the system can be installed in respect to the available budget from top ranking down.

5.1.1. Worst Case Oil/Gas Discharge Volume Calculation

The “worst case discharge”, according to United States Code of Federal Regulation, is defined as “the largest foreseeable discharge of oil, including a discharge from fire or explosion, in adverse weather conditions” as stated in 49 CFR 194.105(b). To determine a worst case discharge, if a flow rate of the transport fluid/gas in pipeline is known, the discharge can be

calculated based on the responding time which include both the detection time from the leakage detection system and the response time of the pipeline operators.

Since the main focus here is the corrosion and the corrosion threat mostly would induce pin-hole damages in pipeline, the worst case discharge in this study will focus on the worst discharge induced by pin-holes. Since the United States doesn't have requirement for pipeline operators to report the pin-hole size when a failure occurred, the hole size related statistics was not available in United States. In European countries, in a pipeline failure report drafted on 2009 [114], 46% of the failure was caused by small holes with diameters less than 20mm (0.79 inch), 20% of the failure was caused by middle size holes with diameters between 20mm (0.79 inch) and 80mm (3.15 inches), 20% of the failure was caused by large size holes with diameter larger than 80mm (3.15 inches), and the rest 14% of the failure was caused by rupture. Thus, if a pin-hole has a size larger than 3 inches, it could be treated as rupture. And generally, if a rupture happened, the leak detection system could immediately confirm the failure.

Thus, in this study, the leak discharge of pin-hole with sizes typically between 0.79 inches to 3 inches were identified as target for analysis. When a corrosion induced pin-hole is in place, there are two stages of oil/gas discharge including oil discharged before and after isolation valves closure. The oil/gas discharge volume before the isolation valves closure (V_T) can be calculated as:

$$V_T = Q_L \cdot t_D + Q_L \cdot t_R \tag{25}$$

where Q_L is the fluid/gas flow rate, t_D is the detection time from the leakage detection system, and t_R is the response time for the pipeline operators.

After the isolation valves are closed, if the pipeline is above water table, all the oil within the two isolation valves eventually will discharge just a matter of time. If the pipeline is beneath

water table, since oil (usually had a specific gravity of 0.7 ~ 0.9) and gas is lighter than water, the water started to replace the space originally occupied by oil in the pipeline. However, water cannot replace all oil transported in the pipeline due to water pressure to stop oil/gas existing in the pipeline coming out. When the two forces reach a balance, the oil discharge stops. Thus, in this case, the oil between the leak location and the lowest elevation of a pipeline would be discharged.

Due to the fact that the corrosion risk assessment will only influence the oil/gas discharge volume before the valves closure, in this study, only the worst case oil/gas discharge before valves closure was analyzed to determine the optimized sensor placement location ranking.

5.1.2. Detection Time

In Equation (25), t_D represents the detection time from the leakage detection system. It describes a time between the initialization of a leak and someone confirmed, or some assessment system detected this leak but not yet took any mitigation action. The detection time usually are determined by the factors such as resolution of the detecting system and the training of employees, etc.

The traditional leakage detection system on site in industrial mainly consisted of pressure gauges, flow rate gauges, temperature gauges, and fluid level gauges [1, 115-118]. When a leak occurs, the flow rate gauge would give different readings before and after the leak location. Oil and gas transmission pipelines are mostly running at high pressure [10], so leak will cause pressure loss which could be detected by the pressure gauges. If the leak occurred at position under water, and the fluid running in the pipeline had temperature difference compared to the outside water, then the temperature gauge will also contribute to the leak detection.

The maximum detection time which can be achieved by the current available leak detection system are shown in the Table 12, for a leakage of 5%, 3%, and 2% of total flow rate. It could be seen that for smaller leak, the detection system requires more time to conform a leak. A 2% of leak required more than 35 minutes to detect it using the current available corrosion detection systems in market. Based on Table 7, an exponential curve fitting was made to estimate the leakage detection system's performance under different sizes of holes failures as shown in Figure 70. It can be seen that if a below 2% leak detection is required, much more time is demanded by using the current available pressure detection system.

Table 12. Normal detection time for on-site leak detection system.

Leak Intensity (of total flow rate)	5%	3%	2%
Detection Time	5 minutes	17.5 minutes	35 minutes

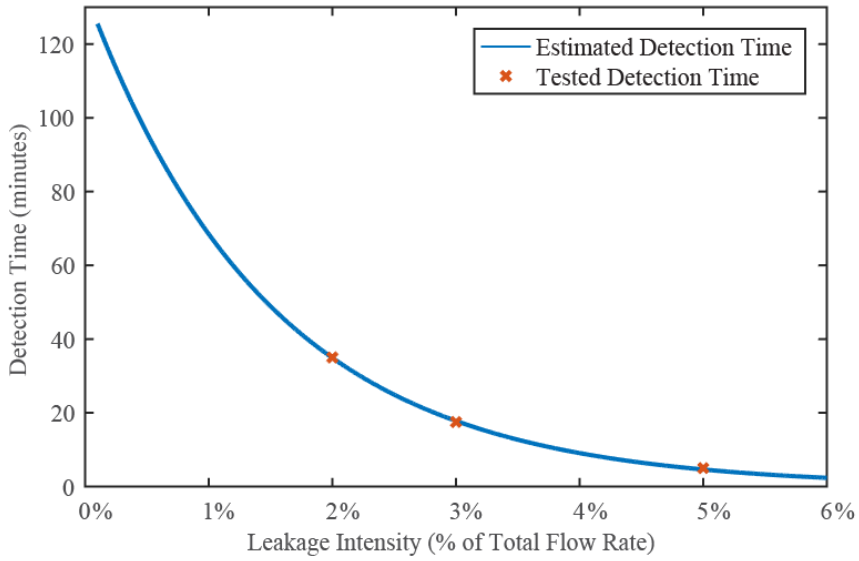

Figure 70. Estimated detection time for different leak level.

5.1.3. Response Time

The response time describes the time between immediately after the leak detected and liable parties started to take action to shut down the pipeline or any other operation to stop the

discharge continuing. The response time usually is determined by the valve closing speed and the training of employees[3, 119]. According to the operation schedule from the pipeline operator, if a leakage indication signal initiated by the system, the direct liable party or responsible employees have normally 15 minutes to determine the severity of situation and give a conclusive response. The pumps and valves on site could be shut down remotely within 1 minute. As a result, the most common response time for a leak is around 16 minutes, which may be longer depending on the actual situations. However, when a rupture occurred, the indicating signal would be extremely strong, and usually the decision to close the isolation valves is immediate so the response time of a rupture could be down to 1 minute.

5.2. Example Case Study

The example case study was assumed to be a pipeline system crossing a lake with the vertical profile as shown in Figure 71. Total length of the pipeline was assumed to be 4 miles with NPS 20 Schedule 60 (outer diameter 20 inches, wall thickness 0.812 inch). Maximum flow rate of the pipeline system was assumed to be 25,200 barrels per hour. There were two cases assumed for the on-site leak detection system including: 1) all available commercial flow gauges and 2) the proposed real-time corrosion assessment system to identify leakage.

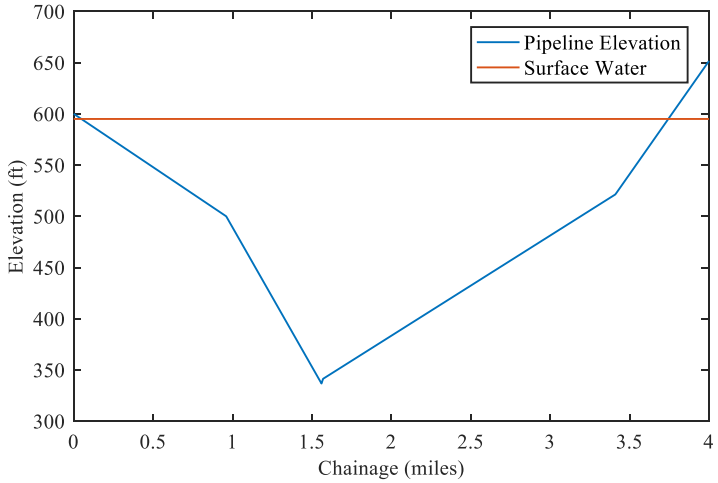

Figure 71. Pipeline elevation profile.

5.2.1. Commercial Detection System

To calculate the worst case discharge based on Equation (25) for using commercial detection system, the leaking flow rate Q_L is required. A larger leaking flow rate requires a smaller detection time. The estimated detection time (t_D) when leaking flow rate (Q_L) was known could be calculated as:

$$t_D = 134.3 \cdot e^{-0.002673 \cdot Q_L} \tag{26}$$

Taken into account that a regular response time is 16 minutes and combined with Equation (26), we have:

$$V_T = Q_L \cdot 134.3 \cdot e^{-0.002673 \cdot Q_L} + 16 \cdot Q_L \tag{27}$$

Let $f(Q_L) = Q_L \cdot 134.3 \cdot e^{-0.002673 \cdot Q_L}$, Equation (27) can be rewritten as:

$$V_T(Q_L) = f(Q_L) + 16 \cdot Q_L \tag{28}$$

In order to get the maximum discharge volume, the first order derivative of function $V_T(Q_L)$ needs to be zero as below:

$$V_T{}'(Q_L) = f'(Q_L) + 16 = 0 \tag{29}$$

where

$$f'(Q_L) = 134.3 \cdot e^{-0.002673 \cdot Q_L} - 0.6737 \cdot Q_L \cdot 134.3 \cdot e^{-0.002673 \cdot Q_L}$$

By plotting $V_T{}'(Q_L)$ as shown in Figure 72, it can be found that there are two solutions for $V_T{}'(Q_L) = 0$, which means the function $V_T(Q_L)$ does not have a maximum value. $V_T(Q_L)$ could increase to infinity as the value of Q_L increased after the second solution (when $Q_L >$ 1000 barrels per hour). Thus, the maximum discharge volume before isolation valves' closure cannot be directly calculated based on mathematics.

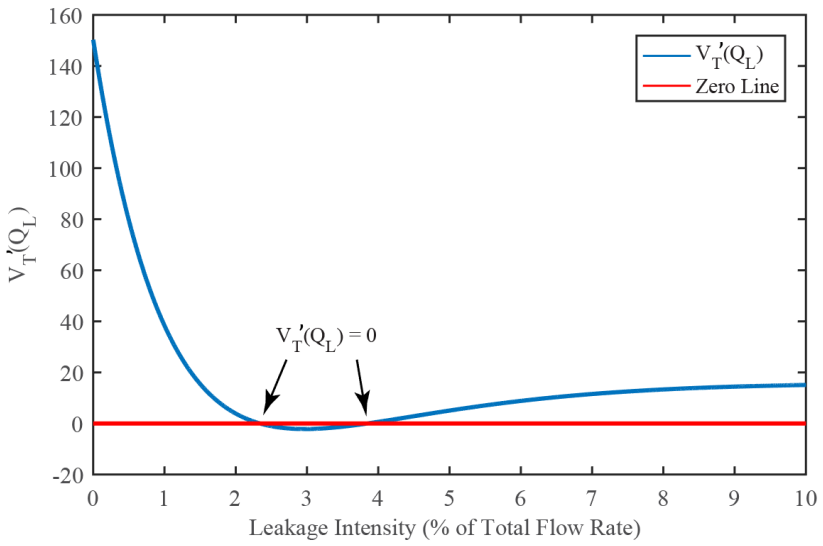

Figure 72. Leaking flow rate vs. first derivative of discharge volume

To find the maximum flow rate, water energy equations below were used. With the limitation of physical properties in the operating pipeline system, the maximum discharge volume could be found. The flow rate by its definition was calculated as:

$$Q = VA \tag{30}$$

where Q is the flow rate, V is the flow speed, and A is the flow cross-section area.

To perform the water energy analysis, station was assumed to be located at two ends of the pipeline as shown in Figure 73. At station, the oil flow was assumed to have a flow rate of $Q_S = 25200$ barrels per hour, flow speed of $V_S = 5.966\ m/s$, cross-section area of pipe of $A = 0.1864\ m^2$, operating pressure $p_s = 180$ psi, and elevation of 178.87 m (586.84 ft). For any other location (in this example, location 1), the oil flow had a flow rate Q_1, flow speed V_1, and elevation of H_1. The cross-section area of pipe would not change along the lake-crossing pipeline system. Thus, assuming the operating pressure in the pipeline system does not change and the oil flow at station was a full pipe flow, then we have:

$$H + \frac{p_s}{\rho g} + \frac{{V_s}^2}{2g} = H_1 + \frac{p_1}{\rho g} + \frac{{V_1}^2}{2g} \tag{31}$$

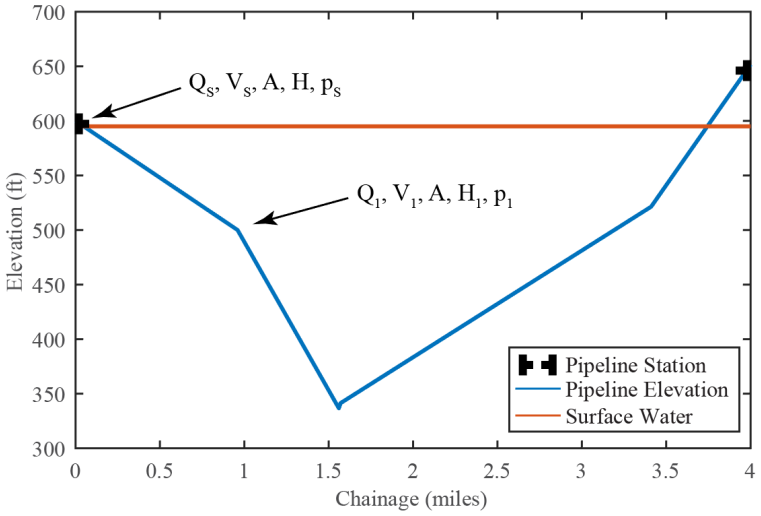

Figure 73. Lake-crossing pipeline system water energy equation demonstration at station and a random location.

If the leakage occurred at location 1, as shown in Figure 74, we have

$$V_1 A_1 = V_2 A_1 + V_3 A_L \tag{32}$$

where A_L is the cross-section area of the leakage hole.

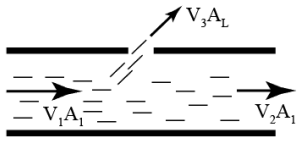

Figure 74. Pin-hole size leak on a pipe.

With elevation profile and Equations (26) to (32) available, the maximum possible leak before valve closure of isolation in this lake-crossing could be plotted as shown in Figure 75. For getting a more realistic result, an additional condition was set that if the leaking flow rate was larger than 20% of the total flow rate (20% of 25200 barrels per hour), the leakage detection system and employees would immediately treat this incident as rupture [114].

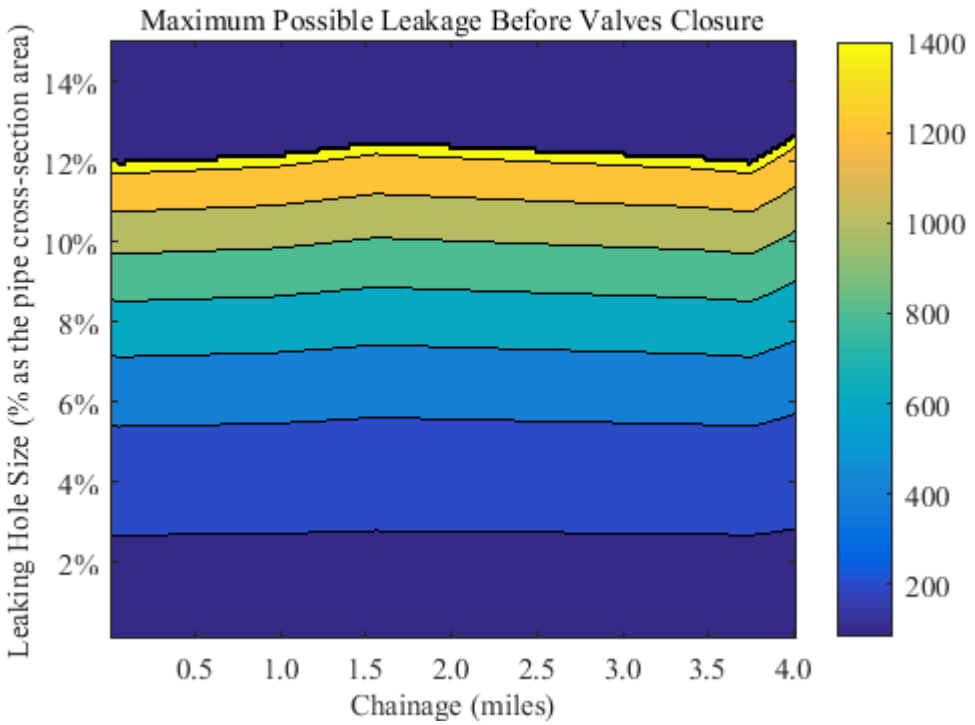

Figure 75. Maximum possible leakage before the valves' closure at different leaking hole size and location.

It was observed from Figure 75 that, most of the locations could reach the maximum leak of 1461 barrels before valve closure. However, at different locations, the minimum required leaking hole size to reach this maximum leakage would be different. At the two points where the pipeline met the water surface (one was at 0.05 miles and the other one was at 3.74 miles), the maximum leakage of 1461 could be reached at a local minimum leak hole size (about 12% of the cross-section area of pipe), which was 2.4 inches. The sudden drops near 1461 barrels of leakage indicated that the leaking hole size was too large so that it triggered the 20% of the total flow rate condition and was treated as rupture. A total oil discharge before closure of isolation valves of 1461 barrels for a regular detection system.

In addition, these two locations, one at 0.05 miles and the other one at 3.74 miles, where maximum leakage could be reached by minimum leak pin-hole sizes would also be the best locations to install sensors of proposed corrosion risk assessment system, as shown in Figure 76.

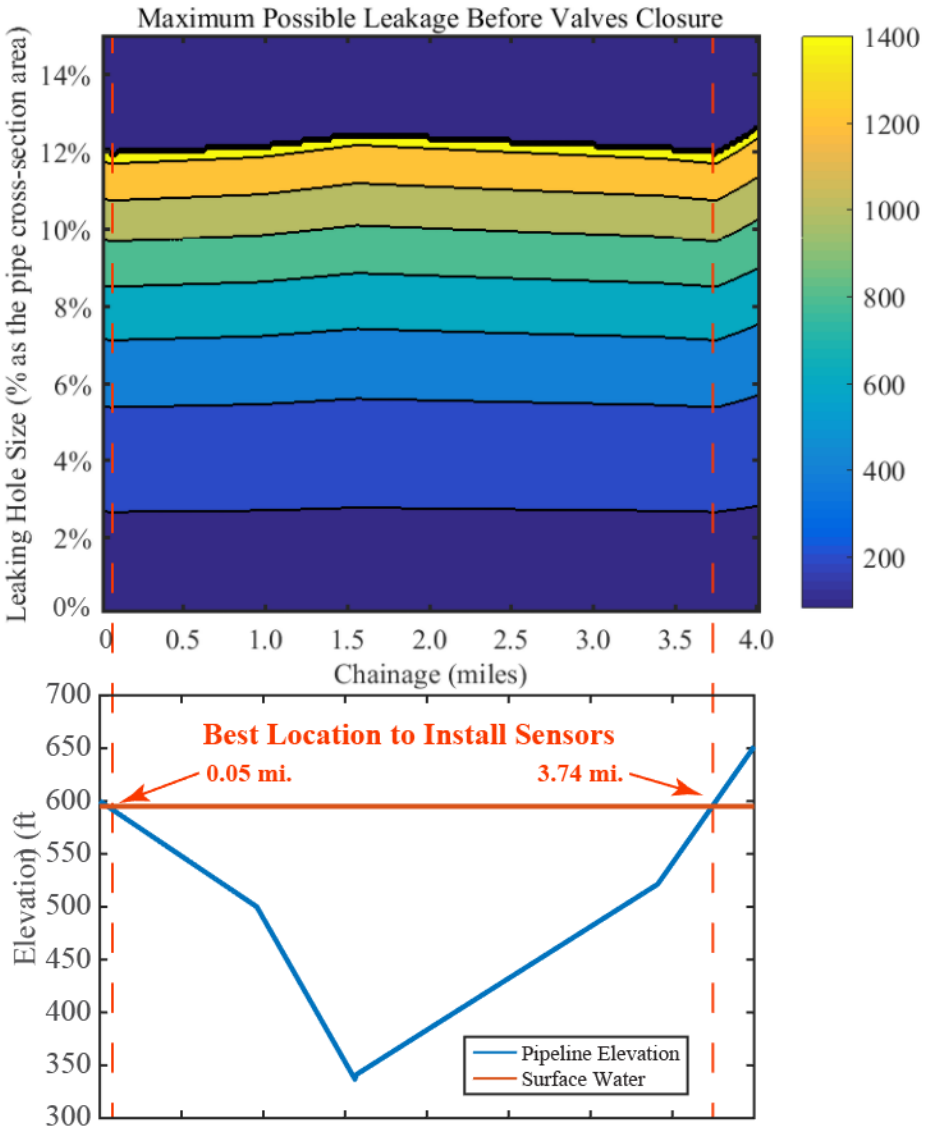

Figure 76. Best locations to for sensor placement.

5.2.2. The Developed Corrosion Assessment System

By applying the proposed corrosion risk assessment system, the corrosion could be detected before it caused severe damage to the pipes. As the pipeline operators was aware of the initialization of corrosion, there would be enough time for them to conduct the corrosion

mitigation plan. Either replacing or continuing to use the existing pipes with extra caution could prevent the pin-hole leakage caused by corrosion on the pipeline system [9]. Thus, with the developed system, the detection time, t_D, in Equation (25) equals to zero and only rupture may cause severe damage and the worst case discharge volume before the valve's closure, therefore, Equation (25) can be rewritten as:

$$V_T = Q \cdot t_R \tag{33}$$

where Q is the maximum operational flow rate, and tR is the responding time.

As mentioned in Section 5.1.3, since the indicating signal of commercial detection system in a rupture case was extremely strong, the liable party might immediately determine the situation and close the valves. As a result, in rupture cases, the response time, t_R, is shortened to one minute.

Hence, based on Equation (33), we have a discharge volume before the isolation valves' closure of:

$$V_T = 25200 \times \frac{1}{60} = 420 \text{ barrels}$$

Comparing this result, 420 barrels to the situation where only commercial detection system was utilized, which could be 1461 barrels as shown in Section 5.2.1, the implementation of the developed system can reduce the worst case oil discharge before the isolation valves' closure by over 70%.

5.3. Summary

In this chapter, the system placement optimization was analyzed using worst case discharge method. An example case study was run to show how the system placement optimization can be achieved for a lake-crossing oil transmission pipeline. Due to the fact that corrosion often caused small pin-hole size leakage, the worst case leak introduced by pin-hole

leak was analyzed and the locations for the worst leak based on the pin-hole leak was analyzed by comparing the current commercial leak detection system and the developed corrosion assessment system. The developed corrosion assessment system can detect the corrosion and its induced damages in real time which reduce the response time to be one minute, which will significantly reduce the oil/gas leak if in place.

6. CONCLUSIONS AND FUTURE WORK

In this dissertation, a novel real-time corrosion risk assessment system based on embedded FBG sensors was developed for coated steel pipelines. Two theoretical models for corrosion monitoring system with substrates, sensors, and coatings were developed to quantitatively analysis the corrosion rate and corrosion severity. Simply supported beam model was used for assessing one-dimensional corrosion and the simply supported plate model was used to locate two-dimensional corrosion. Multiple laboratory experiments were conducted to validating the theoretical study. To optimize the locations to place the corrosion risk assessment system, the worst case oil/gas discharge analysis was proposed to determine the sensor placement locations which was demonstrated using an example case study. Based on the abovementioned comprehensive investigations numerically and experimentally, specific conclusions could be drawn from this study as follow:

1) Corrosion products occupied far more space compared to the original steel metal. This excessive volume increase would lift existing coating and induce strain that could be detected by the FBG sensors on top of it. The Bragg wavelength change rate could serve as an indicator for corrosion rate because it has a positive relationship to the production rate of corrosion. By calibrating the factor in their positive relationship, the corrosion rate could be calculated with the slope of Bragg wavelength change curve.
2) From the experiment results of different types of coatings, the proposed corrosion risk assessment system can effectively measure the corrosion with less than 6% of difference when compared to the electrochemical measurements. Experimental results also showed that when the corrosion continued to grow without control, it can

penetrate or delaminate the coating from the substrate which releases the compressive strains on FBG sensors. As a result, a sudden drop in the Bragg wavelength can indicate a coating failure or crack. In addition, the turning points in Bragg wavelength change curve could serve as indicators for different phases of corrosion progress. Using the multi-phase corrosion growth model, the corrosion progress could be clearly observed from the Bragg wavelength change curve, as Bragg wavelengths of the FBG sensor change with the growth of corrosion qualitatively.

3) The finite element model analysis using ANSYS indicated that the developed 2D simply supported plate model can analyze the transfer function of corrosion localization using multiple sensors. To locate a corrosion in 2D, a minimum of three embedded FBG sensors are required. After transfer function was successfully got from the numerical analysis, the 2D corrosion locations can be estimated using the method of exhaustion. The proof-of-concept laboratory experimental results showed that the exhaustion method can identify the corrosion locations effectively within 0.5 inch.
4) To optimize the system placement for such a big pipeline network, the worst case oil/gas discharge method can be used to rank the most needed locations to place the real-time monitoring systems. An example case study showed that the developed corrosion risk assessment system if placed in the optimized locations can reduce the impact of an oil/gas discharge amount significantly.

From the conclusions, the current system can only identify one single 2D corrosion, in the future, the corrosion risk assessment system will need to further advance to detect multiple corrosion occurred at the sensing area which requires a sensor network with more than three

sensors embedded and an updated corrosion location estimation algorithm. In addition, although the proposed corrosion risk assessment system was validated by several laboratory experiments and showed potential in practical application, to date, no field application has been done using the developed system. Thus, it is of interest to apply the developed corrosion risk assessment system to an actual pipeline for a field testing, which hopefully can be done in near future.

REFERENCES

[1] W. K. Muhlbauer, *Pipeline risk management manual: ideas, techniques, and resources*. Gulf Professional Publishing, 2004.

[2] S. Diller, "Risk assessment and cost-benefit techniques as management tools for oil spill prevention," *WIT Transactions on Ecology and the Environment,* vol. 27, 1998.

[3] D. Jones, J. J. P. Dawson, and P. International, "Risk assessment approach to pipeline life management," vol. 43, no. 1, 1998.

[4] R. Pierre, *Handbook of corrosion engineering*. McGraw-Hill Professional, 1999.

[5] M. Fontana and N. Greene, *Corrosion Engineering, 3rd Edition*. McGraw-Hill book Company, 1987.

[6] A. Aljaroudi, F. Khan, A. Akinturk, M. Haddara, and P. J. J. o. L. P. i. t. P. I. Thodi, "Risk assessment of offshore crude oil pipeline failure," vol. 37, pp. 101-109, 2015.

[7] A. J. A. Jernelöv, "The threats from oil spills: now, then, and in the future," *Ambio,* vol. 39, no. 5-6, pp. 353-366, 2010.

[8] C. B. Chapman, "Large engineering project risk analysis," *IEEE Transactions on Engineering Management,* no. 3, pp. 78-86, 1979.

[9] A. W. Peabody, *Control of pipeline corrosion*. National Association of corrosion engineers Houston, Texas, 1967.

[10] U. S. E. P. Agency, *Profile of the ground transportation industry: trucking, railroad, and pipeline*. Washington D.C.: U.S. Environmental Protection Agency, 1997.

[11] S. C. Davis, S. E. Williams, and R. G. Boundy, "Transportation Energy Data Book: Edition 35," Oak Ridge National Laboratory (ORNL), Oak Ridge, TN (United States)2016.

[12] E. H. Gaylord, C. N. Gaylord, and J. E. Stallmeyer, *Design of Steel Structures, 3rd Edition*. McGraw-Hill, 1991.

[13] M. Bruneau, C.-M. Uang, and S. R. Sabelli, *Ductile design of steel structures*. McGraw Hill Professional, 2011.

[14] W. McGuire and G. Winter, *Steel structures*. Englewood Cliffs, N.J. Prentice-Hall, 1968.

[15] A. P. Eggen, B. N. Sandaker, and C. Norberg-Schulz, *Steel, structure, and architecture*. Whitney Library of Design, 1995.

[16] Y. Kim and E. Worrell, "International comparison of CO 2 emission trends in the iron and steel industry," *Energy policy,* vol. 30, no. 10, pp. 827-838, 2002.

[17] M. Ruth, "Technology change in US iron and steel production: Implications for material and energy use, and CO2 emissions," *Resources Policy,* vol. 21, no. 3, pp. 199-214, 1995.

[18] A. Carreon-Alvarez *et al.*, "Corrosion of aluminum, copper, brass and stainless steel 304 in tequila," *International Journal of Electrochemical Science,* vol. 7, pp. 7877–7887, 2012.

[19] U. Evans, "The Corrosion and Oxidation of Metals: Scientific Principles and Practical Applications, 1960," *London: Edward Arnold,* p. 324.

[20] R. E. Melchers and R. Jeffrey, "Early corrosion of mild steel in seawater," *Corrosion Science,* vol. 47, pp. 1678–1693, 2005.

[21] C. Southwell, J. Bultman, and A. Alexander, "Corrosion of metals in tropical environments. Final report of 16-year exposures," *Materials Performance (MP),* vol. 15, 1976.

[22] A. Bentur, N. Berke, and S. Diamond, *Steel corrosion in concrete: fundamentals and civil engineering practice*. CRC Press, 1997.
[23] J. Cabrera, "Deterioration of concrete due to reinforcement steel corrosion," *Cement and concrete composites,* vol. 18, no. 1, pp. 47-59, 1996.
[24] G. H. Koch, M. P. Brongers, N. G. Thompson, Y. P. Virmani, and J. H. Payer, "Corrosion cost and preventive strategies in the United States," Washington DC,2002.
[25] C. Andrade and C. Alonso, "Corrosion rate monitoring in the laboratory and on-site," *Construction and Building Materials,* vol. 10, pp. 315–328, 1996.
[26] C. Bescond, S. Kruger, D. Lévesque, R. Lima, and B. Marple, "In-situ simultaneous measurement of thickness, elastic moduli and density of thermal sprayed WC-Co coatings by laser-ultrasonics," *Journal of thermal spray technology,* vol. 16, pp. 238–244, 2007 2007.
[27] F. Lakestani, J.-F. Coste, and R. Denis, "Application of ultrasonic Rayleigh waves to thickness measurement of metallic coatings," *NDT & E International,* vol. 28, pp. 171–178, 1995.
[28] A. Legat and V. Dolecek, "Corrosion monitoring system based on measurement and analysis of electrochemical noise," *Corrosion,* vol. 51, pp. 295–300, 1995.
[29] F. Mansfeld and S. Tsai, "Laboratory studies of atmospheric corrosion—I. Weight loss and electrochemical measurements," *Corrosion Science,* vol. 20, pp. 853–872, 1980.
[30] W. Mueller, "Theory of the polarization curve technique for studying corrosion and electrochemical protection," *Canadian Journal of Chemistry,* vol. 38, pp. 576–587, 1960.
[31] J. Pei, M. Yousuf, F. Degertekin, B. Honein, and B. Khuri-Yakub, "Lamb wave tomography and its application in pipe erosion/corrosion monitoring," *Research in nondestructive evaluation,* vol. 8, pp. 189–197, 1996.
[32] B. Popov and R. White, *Electrochemical and Corrosion Experimental Techniques*. Notes USC, 1995.
[33] G. Rosa, R. Oltra, and M.-H. Nadal, "Evaluation of the coating–substrate adhesion by laser-ultrasonics: Modeling and experiments," *Journal of applied physics,* vol. 91, pp. 6744–6753, 2002.
[34] H. Tsuda, J.-R. Lee, Y. Guan, and J. Takatsubo, "Investigation of fatigue crack in stainless steel using a mobile fiber Bragg grating ultrasonic sensor," *Optical Fiber Technology,* vol. 13, pp. 209–214, 2007.
[35] A. Cusano, A. Cutolo, and J. Albert, *Fiber Bragg grating sensors: recent advancements, industrial applications and market exploitation*. Bentham Science Publishers, 2011.
[36] H. Hayes, "Service Life of Coal-Tar Enamel Protective Coatings," *Journal (American Water Works Association),* vol. 32, no. 10, pp. 1705-1722, 1940.
[37] R. S. Perry, "Composition for coating surfaces of iron and steel," United States Patent US1147971 A, 1915.
[38] J. Rowe and M. Mccarty, "Pile-protecting," United States Patent US967442 A, 1910.
[39] M. Soeel, "Method of Preserving Iron And Steel From Rust or Oxidation," United States Patent US510 A, 1837.
[40] K. Alben, "Coal tar coatings of storage tanks. A source of contamination of the potable water supply," *Environmental science & technology,* vol. 14, no. 4, pp. 468-470, 1980.
[41] R. M. Lavker, G. L. Grove, and A. M. Kligman, "The atrophogenic effect of crude coal tar on human epidermis," *British Journal of Dermatology,* vol. 105, no. 1, pp. 77-82, 1981.

[42] J. R. Baylis, "Treatment of Water to Prevent Corrosion1," *Industrial & Engineering Chemistry,* vol. 19, no. 7, pp. 777-781, 1927.
[43] G. De Santis, "Polyurethane sealant-primer system," ed: Google Patents, 1973.
[44] M. Guagliardo, "Dimer acid based polyurethane coating compositions," ed: Google Patents, 1983.
[45] M. Kendig and J. Scully, "Basic aspects of electrochemical impedance application for the life prediction of organic coatings on metals," *Corrosion,* vol. 46, no. 1, pp. 22-29, 1990.
[46] H. Maki, T. Kawamura, and H. Uchikata, "Process for inhibiting corrosion of polyurethane coating," ed: Google Patents, 1986.
[47] S. W. Guan, "The selection, application and inspection of 100% solids polyurethane coatings for corrosion protection," in *SSPC 2000 Conference, November*, 2000, pp. 12-16: Citeseer.
[48] J. A. Kehr, "Fusion-bonded epoxy internal linings and external coatings for pipeline corrosion protection," *PIPING HANDBOOK,* p. 483, 2004.
[49] C. G. Munger and L. D. Vincent, *Corrosion prevention by protective coatings*. United Kingdom: Advanced Materials Research Institute, School of Engineering, University of Northumbria, 1999.
[50] P. A. Sørensen, S. Kiil, K. Dam-Johansen, and C. E. Weinell, "Anticorrosive coatings: a review," *Journal of Coatings Technology and Research,* vol. 6, no. 2, pp. 135-176, 2009.
[51] C. Argent and D. Norman, "Fitness for purpose issues relating to FBE and three layer PE coatings," in *CORROSION 2005*, 2005: NACE International.
[52] A. N. Moosavi, S. O. Al-Mutawwa, S. Balboul, and M. R. Saady, "Hidden problems with three layer polypropylene pipeline coatings," in *CORROSION 2006*, 2006: NACE International.
[53] M. Roche, D. Melot, and G. Paugam, "Recent experience with pipeline coating failures," *Journal of Protective Coatings and Linings,* vol. 23, no. 10, p. 18, 2006.
[54] I. Dahan, U. Admon, N. Frage, J. Sariel, M. Dariel, and J. Moore, "The development of a functionally graded TiC–Ti multilayer hard coating," *Surface and Coatings Technology,* vol. 137, no. 2, pp. 111-115, 2001.
[55] J. R. Davis and others, *Handbook of thermal spray technology*. ASM international, 2004.
[56] S. Fouvry and P. Kapsa, "An energy description of hard coating wear mechanisms," *Surface and Coatings technology,* vol. 138, no. 2, pp. 141-148, 2001.
[57] R. Hauert and J. Patscheider, "From alloying to nanocomposites—Improved performance of hard coatings," *Advanced Engineering Materials,* vol. 2, pp. 247–259, 2000.
[58] S. Matthews and B. James, "Review of Thermal Spray Coating Applications in the Steel Industry: Part 1—Hardware in Steel Making to the Continuous Annealing Process," *Journal of thermal spray technology,* vol. 19, pp. 1267–1276, 2010.
[59] P. Sidky and M. Hocking, "Review of inorganic coatings and coating processes for reducing wear and corrosion," *British Corrosion Journal,* vol. 34, no. 3, pp. 171-183, 1999.
[60] M. U. Schoop, "Method of plating or coating with metallic coatings," Patent US1128059 A, Feb. 9, 1915.
[61] K. Kowalsky, D. Marantz, M. Smith, and W. L. Oberkampf, "HVOF: Particle, flame diagnostics and coating characteristics," Sandia National Labs., Albuquerque, NM (USA)1990.

[62] H. Mahbub, "High velocity oxy-fuel (HVOF) thermal spray deposition of functionally graded coatings," Dublin City University, 2005.
[63] H. S. Manpreet Kaur, Satya Prakash, "A survey of the literature on the use of high velocity oxy‐fuel spray technology for high temperature corrosion and erosion‐corrosion resistant coatings," *Anti-Corrosion Methods and Materials,* vol. 55, no. 2, pp. 86-96, 2008.
[64] K. Cooke, G. Oliver, V. Buchanan, and N. Palmer, "Optimisation of the electric wire arc-spraying process for improved wear resistance of sugar mill roller shells," *Surface and Coatings Technology,* vol. 202, no. 1, pp. 185-188, 2007/11/15/ 2007.
[65] H.-D. Steffens, Z. Babiak, and M. Wewel, "Recent developments in arc spraying," *IEEE Transactions on Plasma Science,* vol. 18, no. 6, pp. 974-979, 1990.
[66] J.-I. Chen, R. Chareonsak, V. Puengpipat, and S. Marturunkakul, "Organic/inorganic composite materials for coating applications," *Journal of applied polymer science,* vol. 74, pp. 1341–1346, 1999.
[67] H. Kozuka, M. Kajimura, T. Hirano, and K. Katayama, "Crack-free, thick ceramic coating films via non-repetitive dip-coating using polyvinylpyrrolidone as stress-relaxing agent," *Journal of Sol-Gel Science and Technology,* vol. 19, no. 1-3, pp. 205-209, 2000.
[68] T. v. Misev and R. Van der Linde, "Powder coatings technology: new developments at the turn of the century," *Progress in Organic Coatings,* vol. 34, pp. 160–168, 1998.
[69] M. Montemor, "Functional and smart coatings for corrosion protection: a review of recent advances," *Surface and Coatings Technology,* vol. 258, pp. 17-37, 2014.
[70] S. Radhakrishnan, N. Sonawane, and C. Siju, "Epoxy powder coatings containing polyaniline for enhanced corrosion protection," *Progress in Organic Coatings,* vol. 64, pp. 383–386, 2009.
[71] K. E. Spear, "Diamond—ceramic coating of the future," *Journal of the American Ceramic Society,* vol. 72, no. 2, pp. 171-191, 1989.
[72] J. Miguel, J. Guilemany, B. Mellor, and Y. Xu, "Acoustic emission study on WC–Co thermal sprayed coatings," *Materials Science and Engineering: A,* vol. 352, pp. 55–63, 2003.
[73] G. Wang *et al.*, "Testing of acoustic emission technology to detect cracks and corrosion in the marine environment," *Journal of Ship Production and Design,* vol. 26, no. 2, pp. 106-110, 2010.
[74] J. Huang, L. Hua, X. Lan, T. Wei, and H. Xiao, "Microwave assisted reconstruction of optical interferograms for distributed fiber optic sensing," *Optics express,* vol. 21, pp. 18152–18159, 2013.
[75] R. Baechler, "Corrosion of metal fastenings in zinc chloride-treated-wood after 20 years," in *Proceedings, American Wood Preservers' Association*, 1949, vol. 45, pp. 390-397.
[76] T. Wright, H. Godard, and I. Jenks, "The Performance of Alcan 65S-T6 Aluminum Alloy Embedded in Certain Woods Under Marine Conditions," *Corrosion,* vol. 13, no. 7, pp. 77-83, 1957.
[77] S. L. Zelinka and D. R. Rammer, *Review of test methods used to determine the corrosion rate of metals in contact with treated wood*. US Department of Agriculture, Forest Service, Forest Products Laboratory Madison, WI, 2005.
[78] Y. Zou, J. Wang, and Y. Zheng, "Electrochemical techniques for determining corrosion rate of rusted steel in seawater," *Corrosion Science,* vol. 53, pp. 208–216, 2011.

[79] M. Jamesh, S. Kumar, and T. S. Narayanan, "Corrosion behavior of commercially pure Mg and ZM21 Mg alloy in Ringer's solution–Long term evaluation by EIS," *Corrosion Science,* vol. 53, no. 2, pp. 645-654, 2011.
[80] J. Liang, P. B. Srinivasan, C. Blawert, M. Störmer, and W. Dietzel, "Electrochemical corrosion behaviour of plasma electrolytic oxidation coatings on AM50 magnesium alloy formed in silicate and phosphate based electrolytes," *Electrochimica Acta,* vol. 54, no. 14, pp. 3842-3850, 2009.
[81] W. Zhu, J. Rose, J. Barshinger, and V. Agarwala, "Ultrasonic guided wave NDT for hidden corrosion detection," *Journal of Research in Nondestructive Evaluation,* vol. 10, no. 4, pp. 205-225, 1998.
[82] J. Sargent, "Corrosion detection in welds and heat-affected zones using ultrasonic Lamb waves," *Insight-Non-Destructive Testing and Condition Monitoring,* vol. 48, no. 3, pp. 160-167, 2006.
[83] E. J. Friebele, "Fiber Bragg grating strain sensors: present and future applications in smart structures," *Optics and Photonics News,* vol. 9, p. 33, 1998.
[84] P. Moyo, J. Brownjohn, R. Suresh, and S. Tjin, "Development of fiber Bragg grating sensors for monitoring civil infrastructure," *Engineering structures,* vol. 27, no. 12, pp. 1828-1834, 2005.
[85] D. Betz, W. Staszewski, G. Thursby, and B. Culshaw, "Multi-functional fibre Bragg grating sensors for fatigue crack detection in metallic structures," *Proceedings of the Institution of Mechanical Engineers, Part G: Journal of Aerospace Engineering,* vol. 220, pp. 453–461, 2006.
[86] A. Maryoto and T. Shimomura, "Numerical Simulation for Corrosion Crack in Concrete Members Considering Penetration of Corrosive Product," *Simulation,* vol. 2, 2013.
[87] K. Kuang, W. Cantwell, C. Thomas, and others, "Crack detection and vertical deflection monitoring in concrete beams using plastic optical fibre sensors," *Measurement Science and Technology,* vol. 14, p. 205, 2003.
[88] Z. Zheng, X. Sun, and Y. Lei, "Monitoring corrosion of reinforcement in concrete structures via fiber Bragg grating sensors," *Frontiers of Mechanical Engineering in China,* vol. 4, pp. 316–319, 2009.
[89] P. Biswas *et al.*, "Investigation on packages of fiber Bragg grating for use as embeddable strain sensor in concrete structure," *Sensors and Actuators A: Physical,* vol. 157, pp. 77–83, 2010.
[90] J. Gao, J. Wu, J. Li, and X. Zhao, "Monitoring of corrosion in reinforced concrete structure using Bragg grating sensing," *NDT & E International,* vol. 44, pp. 202–205, 2011.
[91] Z. Chen, L. Yuan, G. Hefferman, and T. Wei, "Terahertz fiber Bragg grating for distributed sensing," *IEEE Photonics Technology Letters,* vol. 27, pp. 1084–1087, 2015.
[92] V. Dewynter-Marty *et al.*, "Embedded fiber Bragg grating sensors for industrial composite cure monitoring," *Journal of Intelligent Material Systems and Structures,* vol. 9, pp. 785–787, 1998.
[93] D. Fodan, H. Ying, A. Fardad, and W. Yechun, "Pitted Corrosion Detection of Thermal Sprayed Metallic Coatings Using Fiber Bragg Grating Sensors," *Coatings,* vol. 7, p. 35, 2017.
[94] T. K. Gangopadhyay, M. Majumder, A. K. Chakraborty, A. K. Dikshit, and D. K. Bhattacharya, "Fibre Bragg grating strain sensor and study of its packaging material for

use in critical analysis on steel structure," *Sensors and Actuators A: Physical,* vol. 150, pp. 78–86, 2009.
[95] Z.-S. Guo, "Strain and temperature monitoring of asymmetric composite laminate using FBG hybrid sensors," *Structural Health Monitoring,* vol. 6, pp. 191–197, 2007.
[96] E. Kirkby, R. de Oliveira, V. Michaud, and J. M\a anson, "Impact localisation with FBG for a self-healing carbon fibre composite structure," *Composite Structures,* vol. 94, pp. 8–14, 2011.
[97] J.-R. Lee, C.-Y. Yun, and D.-J. Yoon, "A structural corrosion-monitoring sensor based on a pair of prestrained fiber Bragg gratings," *Measurement Science and Technology,* vol. 21, p. 017002, 2009.
[98] L. Ren, Z.-g. Jia, H.-n. Li, and G. Song, "Design and experimental study on FBG hoop-strain sensor in pipeline monitoring," *Optical fiber technology,* vol. 20, pp. 15–23, 2014.
[99] B. Zhang and M. Kahrizi, "High-temperature resistance fiber Bragg grating temperature sensor fabrication," *IEEE Sensors Journal,* vol. 7, pp. 586–591, 2007.
[100] Z. Zhou and J. Ou, "Techniques of temperature compensation for FBG strain sensors used in long-term structural monitoring," 2005, pp. 167–172: International Society for Optics and Photonics.
[101] E. Udd and W. B. Spillman Jr, *Fiber optic sensors: an introduction for engineers and scientists*. John Wiley & Sons, 2011.
[102] O. S. Lee, H. J. I. J. o. P. E. lung Kim, and Manufacturing, "Effect of external corrosion in pipeline on failure prediction," *International Journal of Precision Engineering and Manufacturing,* vol. 1, no. 2, pp. 48-54, 2000.
[103] A. Sheikh, J. Boah, and D. Hansen, "Statistical modeling of pitting corrosion and pipeline reliability," *Corrosion,* vol. 46, no. 3, pp. 190-197, 1990.
[104] W.-K. Lu, R. L. Elsenbaumer, and B. Wessling, "Corrosion protection of mild steel by coatings containing polyaniline," *Synthetic Metals,* vol. 71, no. 1-3, pp. 2163-2166, 1995.
[105] E. McCafferty, "Validation of corrosion rates measured by the Tafel extrapolation method," *Corrosion Science,* vol. 47, no. 12, pp. 3202-3215, 2005.
[106] A. K. Singh and M. Quraishi, "Effect of Cefazolin on the corrosion of mild steel in HCl solution," *Corrosion Science,* vol. 52, no. 1, pp. 152-160, 2010.
[107] A. Maayta and N. Al-Rawashdeh, "Inhibition of acidic corrosion of pure aluminum by some organic compounds," *Corrosion science,* vol. 46, no. 5, pp. 1129-1140, 2004.
[108] Z. Shi, M. Liu, and A. Atrens, "Measurement of the corrosion rate of magnesium alloys using Tafel extrapolation," *Corrosion science,* vol. 52, no. 2, pp. 579-588, 2010.
[109] A. C. Ugural and A. C. Ugural, *Stresses in plates and shells*. McGraw-Hill Boston, 1999.
[110] S. P. Timoshenko and S. Woinowsky-Krieger, *Theory of plates and shells*. McGraw-hill, 1959.
[111] B. SzabÃ, B. A. Szabo, and I. BabuÂška, *Finite element analysis*. John Wiley & Sons, 1991.
[112] L. J. Segerlind, *Applied finite element analysis*. Wiley New York, 1976.
[113] T. J. Hughes, *The finite element method: linear static and dynamic finite element analysis*. Courier Corporation, 2012.
[114] C. Grusell, H. Brandt, and S. Angelsen, "Recommended Failure Rates for Pipelines," in "Energy Report," Det Norske Veritas AS,2010/11/16 2010.
[115] A. Shabtai, Y. Elovici, and L. Rokach, *A survey of data leakage detection and prevention solutions*. Springer Science & Business Media, 2012.

[116] S. Miura, K. Kurita, N. Yoshida, and K. Umayahara, "Fluid leakage detection apparatus and fluid leakage detection method," ed: Google Patents, 2005.
[117] S. L. Scott and M. A. Barrufet, *Worldwide assessment of industry leak detection capabilities for single & multiphase pipelines*. Offshore Technology Research Center College Station, 2003.
[118] T. L. Watson and S. Bachu, "Evaluation of the potential for gas and CO2 leakage along wellbores," *SPE Drilling & Completion,* vol. 24, no. 01, pp. 115-126, 2009.
[119] D. J. Hovey and E. J. Farmer, "Pipeline accident, failure probability determined from historical data," *Oil and Gas Journal (United States);,* vol. 91, no. 28, 1993.